# Spectral energy distribution of hot subdwarfs

**Masterarbeit aus der Physik**

Vorgelegt von

**Johannes Schaffenroth**
28. September 2016

Dr. Karl Remeis-Sternwarte Bamberg
Astronomisches Institut der
Friedrich-Alexander-Universität Erlangen-Nürnberg


Betreuer: Prof. Dr. Ulrich Heber

# Contents

# Abbreviations and Astronomical catalogues

| | |
|---|---|
| **SED** | Spectral energy distribution |
| **EHB** | Extended or Extreme Horizontal Branch |
| **ZAEHB** | Zero-Age EHB |
| **TAEHB** | Terminal-Age EHB |
| **SDSS** | Sloan Digital Sky Survey |
| **Galex** | Galaxy Evolution Explorer |
| **AAVSO** | American Association of Variable Star Observers |
| **APASS** | AAVSO Photometric All-Sky Survey |
| **2MASS** | Two Micron All Sky Survey |
| **UKIRT** | United Kingdom Infrared Telescope |
| **UKIDSS** | UKIRT Infrared Deep Sky Survey |
| **WISE** | Wide-Field Infrared Survey Explorer |
| **IUE** | International Ultraviolet Explorer |
| **ISIS** | Interactive Spectral Interpretation System |

## Astronomical catalogues

| | |
|---|---|
| **ASAS** | All Sky Automated Survey (variable objects) |
| **BA** | Balloon (Early-type stars) |
| **BD** | Bonner Durchmusterung |
| **CBS** | Case Blue Stars |
| **CD** | Cordoba Durchmusterung |
| **CPD** | Cape Photographic Durchmusterung |
| **CS** | Coalsack |
| **EC** | Edinburgh-Cape Survey (blue objects) |
| **EGB** | Ellis, Grayson, Bond (Planetary nebulae) |
| **EGGR** | Eggen, Greenstein (White dwarfs) |
| **FB** | Faint Blue |
| **FBS** | First Byurakan Survey (late-type stars) |
| **Feige** | (Underluminous hot stars) |

| | |
|---|---|
| **GD** | Giclas Dwarf (white dwarfs or blue stars) |
| **HD** | Henry Draper Catalogue (bright stars) |
| **HDE** | Henry Draper Extension |
| **HE** | Hamburg-ESO survey |
| **HIC** | Hipparcos Input Catalogue |
| **HIP** | Hipparcos |
| **HS** | Hamburg Schmidt Survey |
| **HZ** | Humason, Zwicky (blue stars) |
| **JL** | Jaidee, Lynga |
| **KIC** | Kepler Input Catalog |
| **KUV** | Kiso UV-excess objects |
| **KPD** | Kitt Peak, Downes (UV-Excess objects) |
| **LB** | Luyten Blue stars |
| **LBQS** | Large Bright Quasar Survey |
| **LS** | Luminous stars |
| **LSE** | Luminous Star Catalogue Extension |
| **LSS** | Luminous Stars Southern Milky Way |
| **MCT** | Montreal-Cambridge-Tololo (UV-excess objects in Southern Hemisphere) |
| **NSV** | New Catalogue of Suspected Variable Stars |
| **OGLE** | Optical Gravitational Lensing Experiment (variable stars) |
| **PB** | Palomar-Berger (stars and compact objects) |
| **PG** | Palomar-Green (UV and quasars) |
| **PHL** | Palomar-Haro-Luyten |
| **PN** | Planetary nebulae |
| **SB** | Slettabak, Brundage |
| **SBSS** | Second Byurakan Survey Stars |
| **TON** | Tonantzintla (blue stars) |
| **TONS** | Tonantzintla South Pole |
| **TYC** | The Tycho-2 catalogue of the 2.5 million brightest stars |
| **US** | Usher (faint blue objects) |
| **UVEX** | UV Excess Survey of the Northern Galactic Plane |
| **UVO** | UV objects |

# 1. Introduction

The interest of humans for the processes in the sky probably began with their existence. Many cultures observed the motion of the sun, the moon, the planets and the stars and tried to explain with various theories. The most prominent object in the night sky beside the moon and the planets are stars. The branch of stellar astronomy is one of the oldest since observations of stars can be done with the naked eye. But new technologies made the observation of many new objects possible and opened various new fields in astronomy. For example the invention of x-ray and radio telescopes enables the investigation of black-holes and neutron stars. Bigger telescopes allow the observation of extragalactic objects and very distant galaxies and the field of cosmology treats the investigation of the universe as a whole. The progress in technology and the accuracy of new instruments and detectors in the last two decades even allowed the observation of planets around stars outside our solar system, so called exoplanets and the detection of long predicted gravitational waves.

Although stars have probably been probed the longest time there are still many open questions. One topic currently addressed is the investigation of hot subdwarfs (sdB/Os). They are faint blue stars often found at high galactic latitudes. With masses around $0.5\,M_\odot$ and radii between $0.1\,R_\odot$ and $0.3\,R_\odot$ they are much smaller and of lower mass than hot main sequence stars of similar spectral types. These very compact objects are identified as helium core-burning stars with a very thin hydrogen envelope. The formation of these stars is not yet fully understood but there must be a mechanism that removes almost all of the hydrogen envelope at about the same time the helium core has attained the mass required for the helium flash. One possible explanation for the mass loss is due to the gravitational interaction with a nearby star which is likely since a large fraction of sdB stars was found in short period binary systems. Maxted et al. (2001) states that two thirds of all sdBs are in detached binary systems with periods between a few hours and days. More recent investigations indicate that half of the sdBs reside in such close binaries (Napiwotzki et al., 2004; Copperwheat et al., 2011). The assumed formation channel is that the progenitor of the subdwarf, which is most likely a red giant, fills its Roche lobe and forms a common envelope with its companion. This envelope is then ejected. This also explains the short period of the binary systems since the orbit in a common envelope shrinks due to friction. Alternatively the hot subdwarf loses its envelope through stable Roche lobe overflow.

The companion to a hot subdwarf is usually either a white dwarf or a cool main-sequence star. But also substellar objects like brown dwarfs and planets have been found. Even circumbinary planets orbiting hot subdwarfs were detected.

One tool to analyse hot subdwarfs is the construction of their spectral energy distribution using photometric data. This allows to determine atmospheric parameters like effective

temperature and surface gravity of the observed object. But also the degree of interstellar reddening can be determined and the distance can be estimated. This is possible since photometry measures the absolute flux of an object in contrast to spectroscopy where usually only relative fluxes are measured. A photometric analysis also has the capability of detecting and classifying the companion to a hot subdwarf. A potential companion can be spotted in the photometric data as a color excess in the infrared passbands or in the spectral energy distribution due to an excess in the infrared. This is because cool objects like late-type main-sequence stars emit mainly in the infrared in contrast to the subdwarfs which are brightest in the ultraviolet. However, compact objects like white dwarfs or very faint objects like very small and low-mass stars or brown dwarfs or planets can not be detected that way because they are either too faint to generate a significant signal or they are simply outshined by the hot subdwarf.

Information about the companion can be obtained when modelling both components individually and then compare the composite spectral energy distribution to the available data. This allows to determine the atmospheric parameters of both components to some degree and gives hint about the flux ratio between both components.

In the following work several samples of hot subdwarfs are analysed by constructing their spectral energy distribution. In this way, their atmospheric parameters, reddening and distance are determined. Potential main-sequence companions are identified and were investigated as well.

# 2. Stellar evolution and hot subdwarfs

The stellar evolution begins with the birth of a protostar through gravitational collapse of a gas cloud in the interstellar medium. When the gas cloud contracts the gravitational potential energy is transformed into thermal energy which heats the cloud after it has become dense enough to absorb a relevant portion of the radiation. This leads to an increase of pressure which slows the free fall of the particles. The increase in temperature and pressure then leads to ionization and to the formation of a plasma. This consumes some energy and slightly slows down the heating. At some point the temperature in the core will be high enough to ignite thermal nuclear fusion. This marks the beginning of the main-sequence phase. The star is now in a stable equilibrium and its only source of energy is the energy released by the burning of hydrogen in the core. A detailed description about star formation and the further stellar evolution can be found in most astronomical standard textbooks like for example Karttunen et al. (2007) or Carroll & Ostlie (2007).

A very clear depiction of the further stellar evolution can be given with the aid of the so called Hertzsprung-Russell (HR) diagram, where the relation between the luminosity and the effective temperature of a star is plotted (see figure 2.2).

In the Hertzsprung-Russell diagram the majority of stars is found on a roughly diagonal line, namely the main sequence. This is because the main-sequence phase takes up most of the lifetime of a star. The duration depends on the mass of the star and takes for a solar type star up to 10 billion years. The main-sequence phase ends when all the hydrogen in the core has been burned into helium. Now the thermal nuclear fusion in the core stops and a star with a helium core and hydrogen fusion in a shell around the core remains. This leads to an increase of helium in the core which in turn leads to an expansion of the star's envelope. Since the star's radius increases the released energy is distributed over a much larger surface area resulting in a lower surface temperature which makes the star appear more red even though the star's luminosity increases. Therefore this stage is called the Red Giant Phase (stars on the main-sequence in contrast are called dwarfs). In the HR-diagram the star now moves towards the top right corner. The further evolution depends on the mass of the progenitor star. For stars more massive than half the solar mass the temperature in the core will increase towards the point where helium burning in the core can begin with an explosion called the helium flash. The temperature of the star increases and in the HR-diagram it moves towards the left on the Horizontal Branch. For stars more massive than 2.3 solar masses the helium burning sets in without a helium flash since the core is not degenerate.

After the helium burning phase the thermal nuclear fusion continues with heavier elements up to iron depending on the star's mass. After the last fusion episode the star

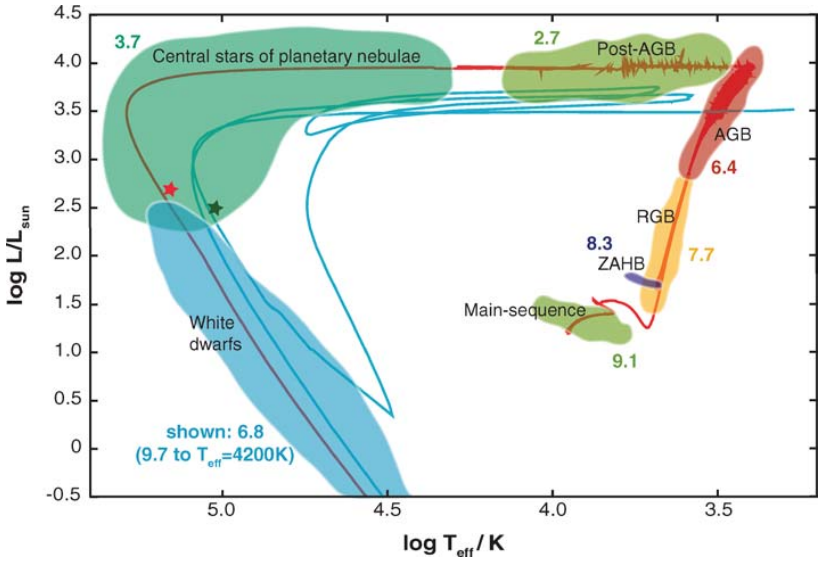


Figure 2.1.: Schematic depiction of the evolution of a 2 solar mass star. The different stages of stellar evolution are highlighted with color. From the main-sequence to the Red Giant Branch (RGB) over the Horizontal Branch (HB) to the Asymptotic Giant Branch (AGB) and finally over the Planetary Nebulae phase to the final stage of stellar evolution, the White Dwarf phase. (Herwig, 2005)

either cools off to a white dwarf or the core collapses and the star will explode in a supernova. The remnant of this explosion can then either be a neutron star or a black hole. A schematic illustration of the evolution of a 2 solar mass star can be found on figure 2.1.

## 2.1. Hot subdwarfs

Besides the classical stellar evolution there are several outliers which can be found at various places in the HR-diagram, among them a population of stars found in the lower left area of the HR-diagram (see figure 2.2). These stars are fainter and smaller than main-sequence stars (dwarfs) and are therefore called hot subdwarfs. They show spectral features similar to O- and B-stars just with stronger and broader Balmer lines. The location of the subdwarfs in the HR-diagram is a blueward extension of the Horizontal Branch (HB) and hence is called Extreme or Extended Horizontal Branch (EHB) which indicates that these stars are in the stage of helium core burning. But in contrast to usual HB-stars, they have only a very thin hydrogen envelope ($M_{\mathrm{env}} < 0.02 M_{\odot}$) which makes them basically helium burning cores. That also explains the relative high surface temperature (between 20000 and 50000 K). Beside that, these objects are also quite

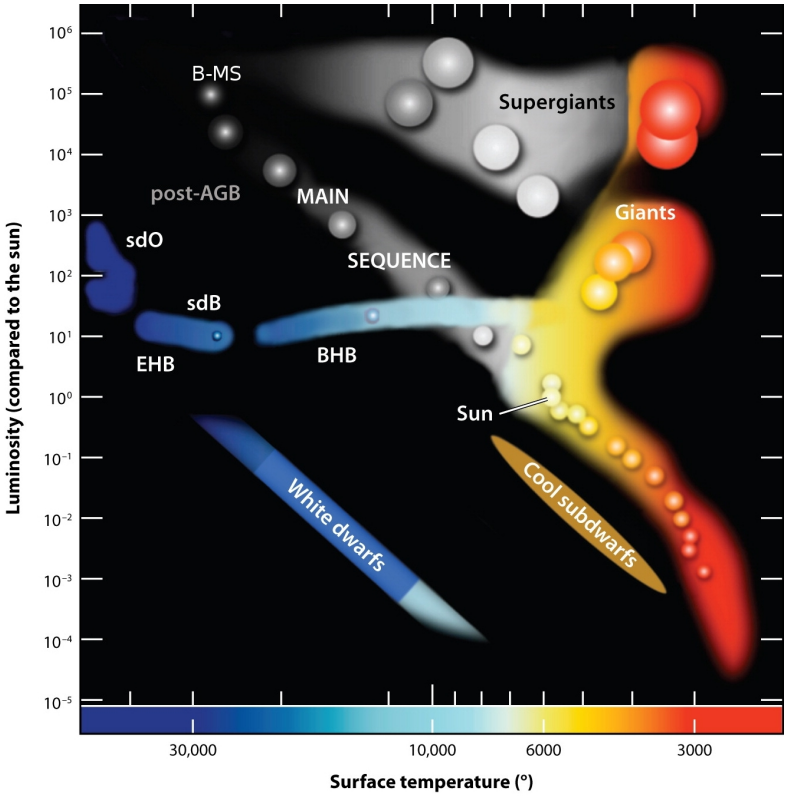


Figure 2.2.: The location of the hot subdwarfs (sdB and sdO) in the Hertzsprung-Russell diagram is below the hot end of the main sequence and above the white dwarf cooling sequence (Heber, 2009).

compact. Their logarithmic surface gravity is more than one magnitude higher than that of a main-sequence stars of the same spectral type ($\log g \sim$ 5-6 dex). In order to form such an object the star has to lose its envelope almost entirely after passing the Red Giant Branch because this means the star has not enough mass to sustain hydrogen shell burning and cannot evolve in the canonical way towards the Asymptotic Giant Branch. Instead the further stellar evolution will be helium core burning followed by a very brief period of helium shell burning. The final stage then is cooling off to a white dwarf. The reasons for the high mass loss resulting in the loss of the envelope are not fully understand yet.

## 2.2. Chemical composition anomalies and diffusion

Investigations of the chemical composition of hot subdwarfs by O'Toole & Heber (2006), Blanchette et al. (2008) and Naslim et al. (2013) showed that there are significant deviations from the solar composition. Helium and other light elements are depleted, whereas

many heavy elements are enhanced in the photosphere. The mean abundances relative to solar values for a couple of elements of sdBs and helium-sdBs are shown in Figure 2.3. The peculiarity of the elemental abundances in hot subdwarfs is assumed to be caused by

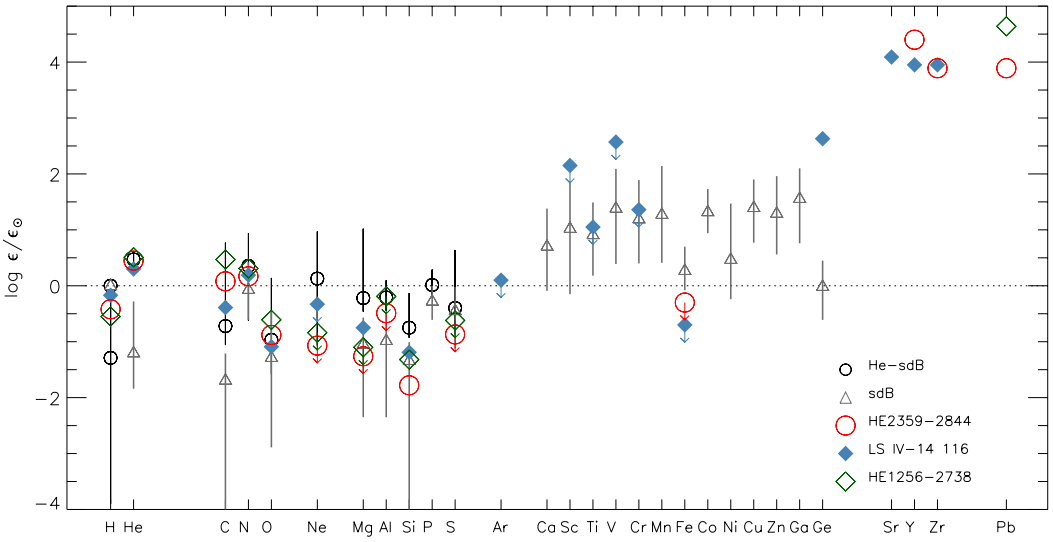


Figure 2.3.: Mean elemental abundances relative to solar values (Naslim et al., 2013).

atomic diffusion processes in the stellar atmosphere. This topic is adressed in the reviews on hot subdwarfs by Heber (2009) and Heber (2016). In a simple picture, the elemental abundance is the result of a balance between gravitational and radiative forces.
A gravitational pull causes heavier elements in the atmosphere to sink down towards the center of the star (gravitational settling). Radiative acceleration on the other hand leads to an ascension of certain elements because momentum is transferred to the atom in the absorption process. Since hot stars emit most of their flux in the ultraviolet (UV), elements with many absorption lines in that region are affected most. Saturation of the spectral lines limits the radiation pressure and an equilibrium between radiative acceleration and gravitational settling sets in. The time scales of these processes are short compared to the evolutionary time.
This causes some problems because helium should sink down since there are barely lines in the UV. The predicted abundance is 2 orders of magnitude lower than what is observed on average. At these low abundances helium should not be observable after all. On the other hand radiative acceleration should increase the abundance of atoms with many UV lines to super solar.
Therefore the diffusion process has to be slowed down somehow. Two suggested mechanisms are for example mass loss through stellar winds (Vink & Cassisi, 2002) or turbulence in subphotosheric layers (Hu et al., 2011).
More information on the chemical composition anomalies of hot subdwarfs can be found for example in Geier (2013).

# 3. Spectral energy distribution of stars

The spectral energy distribution (SED) is defined as the energy emitted from a source as a function of wavelength. In astronomy the energy is usually not measured directly. Instead an object's flux $F$ is measured which is defined as the energy per unit area per unit time. This quantity decreases with the distance to the object squared. The total flux of a star is given by its luminosity. For a spherical object radiating isotropically the radiation at a distance $r$ is distributed evenly on a spherical surface whose area is $4\pi r^2$. This yields a luminosity $L = 4\pi r^2 F$.

The spectral energy distribution of a star can be described as a blackbody to a first approximation. Therefore the properties of a blackbody will be discussed in the following section.

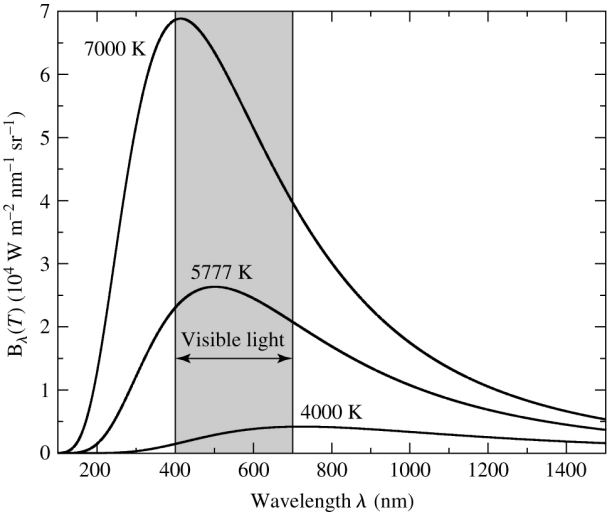


Figure 3.1.: Blackbody spectrum for three different temperatures. With increasing temperature the overall emitted energy increases and the wavelength with the maximum emitted energy decreases (Carroll & Ostlie, 2007).

## 3.1. Blackbody radiation

A blackbody is defined as an object that absorbs all incident radiation. The absorbed radiation is emitted when the object is in thermal equilibrium. The distribution of the

radiated light follows Planck's law which is a function of temperature only:

$$B_\lambda(T) = \frac{2hc^2}{\lambda^5} \frac{1}{\mathrm{e}^{hc/\lambda kT} - 1} \,. \tag{3.1}$$

This distribution is shown in figure 3.1. The intensity peak of the blackbody spectrum is shifted towards shorter wavelengths with increasing temperature. This fact is described by the Wien displacement law

$$\lambda_{\max} T = b \tag{3.2}$$

where $b$ is the Wien displacement constant

$$b = 0.0028978\,\mathrm{Km} \tag{3.3}$$

The flux of a blackbody is given by

$$F = \sigma T^4 \tag{3.4}$$

which is called the Stefan-Boltzmann law. This leads to the fact that the overall energy emitted by a blackbody increases with temperature.

$$L = 4\pi r^2 \sigma T^4 \tag{3.5}$$

This allows to assign every spectral energy distribution with the same total radiation (integrated over all frequencies) an effective temperature which is the temperature of a blackbody with the very same total flux.

As already mentioned the blackbody is only a first approximation of the spectral energy distribution of a star. Figure 3.2 shows that there are deviations from the stellar spectrum, more or less distinct depending on the spectral type of the star. These deviations originate mostly from the interaction of the continuum light with the atoms and molecules in the stellar atmosphere. Three features which affect the shape of the SED most are discussed in the following sections: the $H^-$ opacity which shapes the SED of cool stars, the Balmer discontinuity which is most pronounced in hot stars and the metalicity which alters the stellar flux in the UV.

Furthermore the light emitted by stars travels trough interstellar gas and dust which further modifies the SED (see section 3.5).

## 3.2. $H^-$ opacity

The feature at 17000 Å in the SED of the cool star (3.2a) is caused by negative hydrogen (Basu, 2003; Robinson, 2007). Negative hydrogen is a neutral hydrogen atom which captured an additional electron. This can happen when the neutral hydrogen is polarized by a nearby charge. The resulting $H^-$-ion is very fragile and can be easily ionized at temperatures of a few thousand kelvin. This means negative hydrogen can only exist in cooler stars because the higher temperature in hot stars would quickly dissociate any

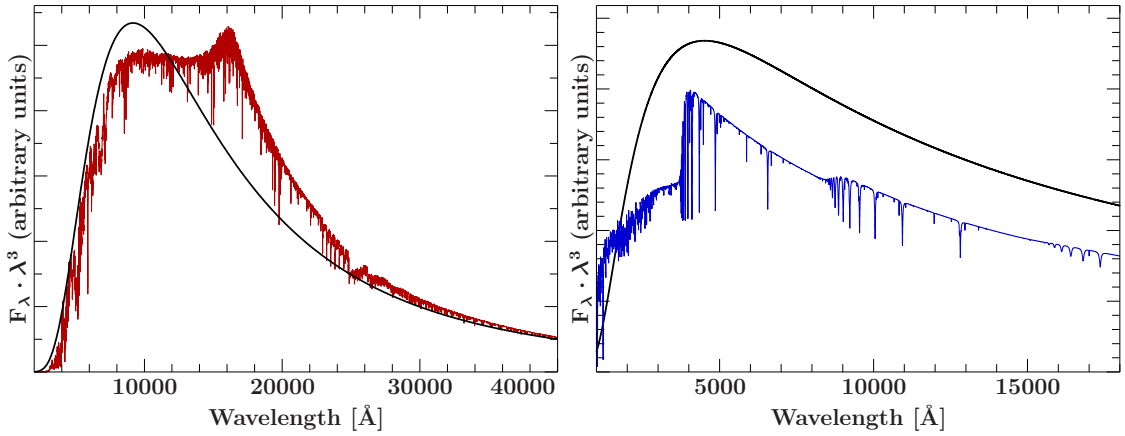


(a) cool ($T_{eff} = 4000\,K$) (b) hot ($T_{eff} = 20000\,K$)

Figure 3.2.: A comparison between the spectrum of a hot/cool star and the respective blackbody spectrum shows good agreement for the cool star apart from a flux maximum at around 17000 Å arising from a change in $H^-$ opacity. For the hot star the discrepancy is clearly bigger. Here the main difference is caused by the Balmer discontinuity.

$H^-$-ion which may form. The photoionisation energy of negative hydrogen is 0.754 eV, which means photons with a wavelength shorter than 16450 Å can dissociate the $H^-$-ion. Therefore for cool stars $H^-$ is responsible for almost the entire continuum absorption in the optical.

The formation of negative hydrogen requires neutral hydrogen and free electrons which come mainly from singly ionized metals. Therefore the $H^-$ opacity is sensitive to metallicity and temperature. At very low metal abundances or at temperatures below 3000 K the $H^-$ opacity becomes ineffective. At temperatures above 10000 K all negative ions are dissociated and Kramers opacity and electron scattering take over.

Figure 3.3 shows all the opacity contributions for a late main-sequence star with an effective temperature of 6429 K. One can see that below 17000 Å the main contribution is due to bound-free absorption of $H^-$. At around 17000 Å there is an opacity dip resulting in increased flux emission at this wavelength. At longer wavelength free-free absorption of $H^-$ takes over and the opacity increases again. The opacity dip is well sampled by the 2MASS photometric system. The H-passband is centered around the minimum opacity. For more information about the 2MASS photometric system see section 4.1.2.

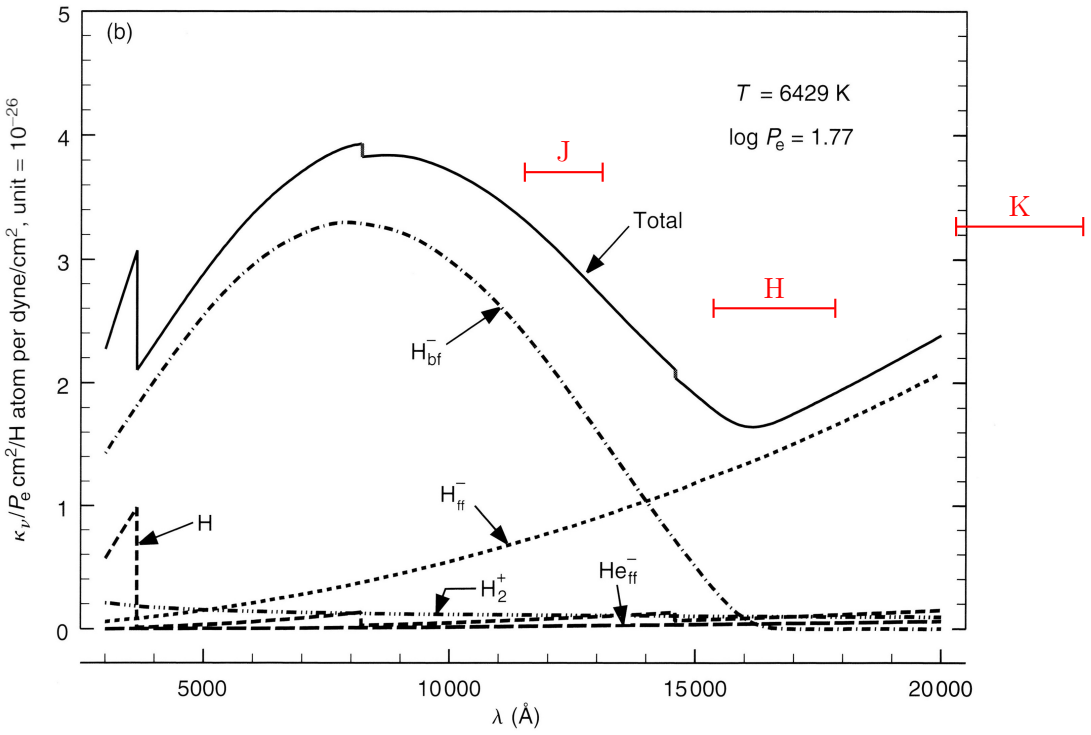


Figure 3.3.: Opacity curve for a late main-sequence star ($T_{\mathrm{eff}} = 6429\,\mathrm{K}$). The dominant source of opacity for this kind of stars is caused by negative hydrogen. Both bound-free and free-free absorption are possible. Bound-free opacity is predominant in the optical and free-free becomes important in the far infrared. In between there is a opacity dip at 17000 Å which is well sampled by the 2MASS photometric system (JHK). (Gray, 2008)

## 3.3. Balmer discontinuity

As already mentioned the $H^-$ opacity plays only a role in cool stars. For hot stars there is a distinctive feature at about 3650 Å where the intensity suddenly drops for shorter wavelengths. This is the so called Balmer discontinuity or Balmer Jump. It is caused by electrons being ionized from the second level of hydrogen. This leads to continuum opacity at wavelengths shorter than the minimum ionization energy. This effect is strongest in A type stars like Vega. The jump decreases for hotter or cooler stars. The strength of the Balmer jump is given by the number of hydrogen atoms in the second energy level and the amount of radiation below 3650 Å. Therefore it scales with both temperature and surface gravity.

For very hot stars ($T_{\text{eff}}$>40000) the Balmer discontinuity almost vanishes since there are barely neutral hydrogen atoms in the atmosphere because nearly all hydrogen is ionized. With decreasing temperature the number of neutral hydrogen increases and consequently the strength of the Balmer jump increases as well. This continues until to the spectral type A where there is only little ionized hydrogen. For even cooler temperatures the ratio between negative hydrogen and neutral hydrogen increases and $H^-$ becomes the dominant source of opacity.

For cool stars the surface gravity has a larger effect on the Balmer jump than temperature. For hotter stars like hot subdwarfs the Balmer jump is almost solely affected by temperature (see figure 3.5). The difference in intensity decreases with increasing temperature. Figure 3.4 shows that the surface gravity virtually does not affect the spectral energy distribution and therefore can't be easily determined by means of stellar photometry.

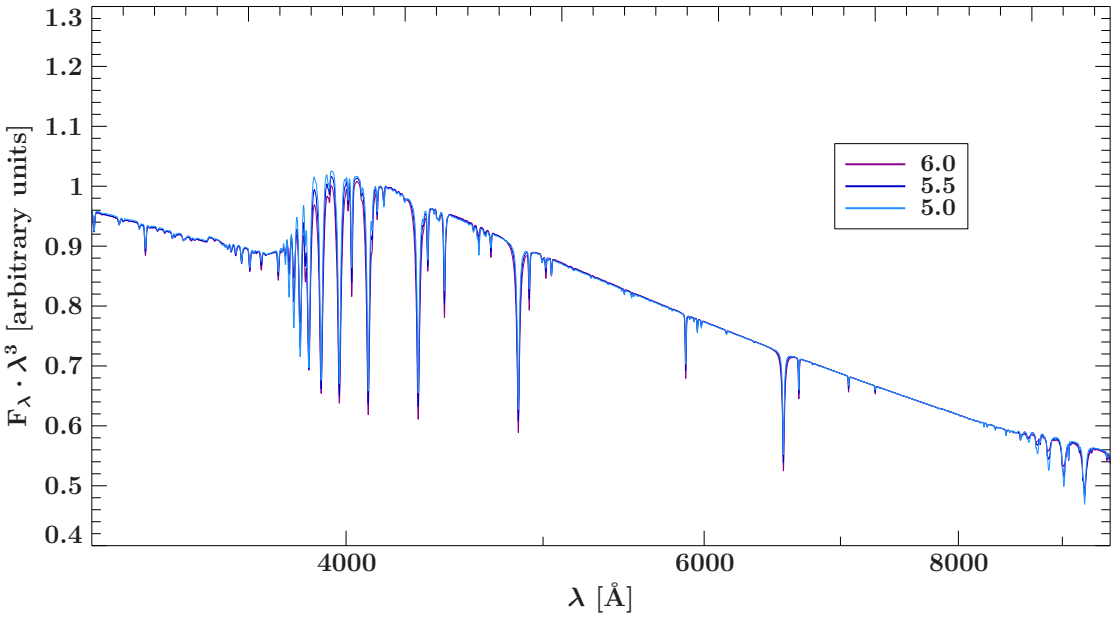


Figure 3.4.: Spectral energy distribution of a 30000 K star for three different surface gravities ($\log g = 5.0$, 5.5, 6.0). The SEDs were normalized to the maximum flux at around 4000 Å to show the effect on the balmer jump and the photometric colors.

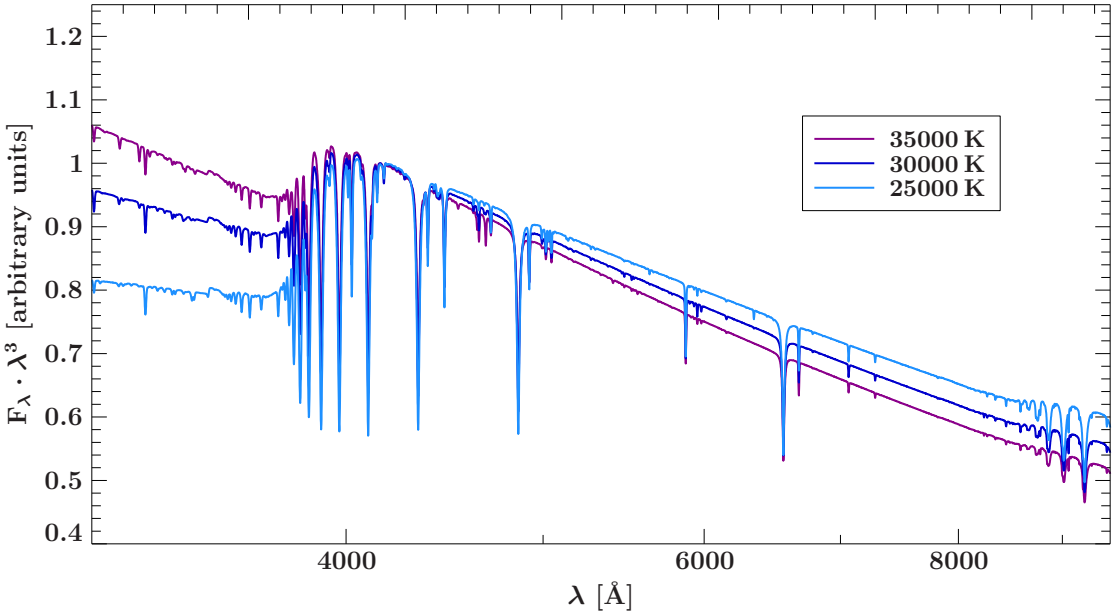


Figure 3.5.: Spectral energy distributions with $\log g = 5.5$ and effective temperature 25000 K, 30000 K and 35000 K. The SEDs were normalized to the maximum flux at around 4000 Å to show the effect on the balmer jump and the photometric colors.

## 3.4. Metalicity

The amount of metals in the atmosphere of a star can also affect the shape of the spectral energy distribution. This especially affects the ultraviolet part of the spectrum since there are many metal lines that can lead to absorption and therefore increase the opacity in that region. Figure 3.6 shows three SEDs with three different metal abundances. The SED with z=0 has a metal composite that is typical for a hot subdwarf. The chemical composition of subdwarfs is different from the solar one. For details see section 2.2. The spectra with z=1 has the same composition but ten times increased and z=-1 on the other hand only has a tenth of this composition. One can see that with increasing metalicity the flux at shorter wavelengths than 2500 Å decreases more and more. The optical part of the spectrum on the other hand is more or less unaltered. This means that one can only determine the metalicity of a star using photometry if photometric observations in the ultraviolet region are available.

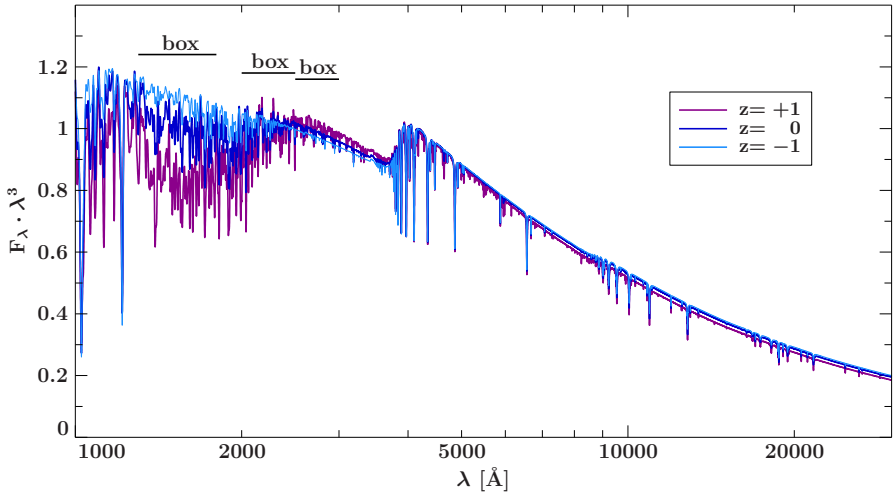


Figure 3.6.: SED of a 30000 K sdB star for three different values of z. The flux was normalized to the maximum at around 4000 Å. The three box filter in the UV are overplotted (see section 4.1.3)

## 3.5. Interstellar extinction

The space between stars is not empty. The presence of particles in the line of sight can change the emitted spectrum because absorption and scattering can occur in the interstellar medium. It turned out that this extinction is selective and has more effect on the bluer parts of the spectrum. This leaves the spectrum more red. That is why the term interstellar reddening is often considered synonymous to interstellar extinction.
A good example for interstellar extinction are dust clouds (Figure 3.7). Here the amount of grains is so high that almost all light in the optical is scattered or absorbed which

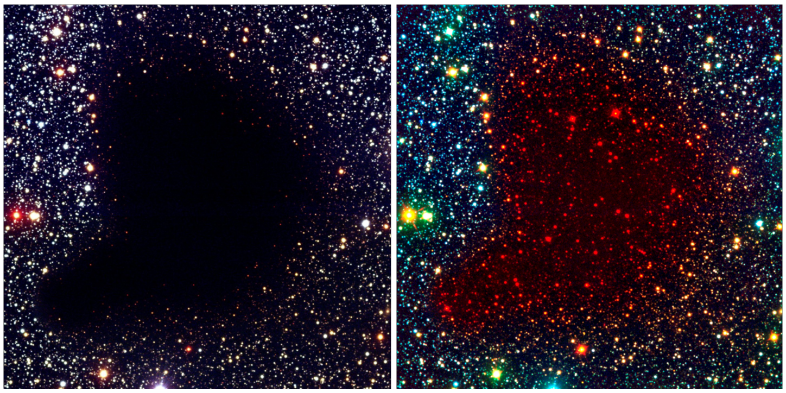

Figure 3.7.: Barnard 68, an example for extinction by interstellar dust. The cloud is opaque for light in the optical but becomes transparent if observed in the infrared. Credit: ESO

leaves the area dark. But since longer wavelengths are affected less and more light is transmitted by the dust the cloud gets transparent and stars in the background become visible.

The wavelength dependency of interstellar extinction has been examined by comparing stars of the same spectral class. A comparison of the spectrum of a star with negligible foreground dust with a heavily reddened star and the assumption that the extinction goes to zero at very long wavelengths allows to determine the extinction $A_\lambda = 2.5 \log(F_\lambda^0/F_\lambda)$ as a function of wavelength, where $F_\lambda$ is the observed flux and $F_\lambda^0$ is the flux in the absence of reddening (Draine, 2003). The shape of this function gives hints about the nature and size of the absorbing material.

The dimensionless quantity $R_V = A_V/(A_B - A_V)$ is commonly used to describe the slope of the extinction curve in the optical. $A_V$ and $A_B$ are the extinctions measured in the V (5500 Å) and the B (4400 Å) band.

Large grains would produce gray extinction with $R_V \to \infty$ and Rayleigh scattering would produce very steep extinction with $R_V \sim 1.2$. $R_V$ is known to vary between 2.1 up to 5.8 (Wang et al., 2013). Various investigations of interstellar extinction concluded that $R_V = 3.1$ is an average value for diffuse regions in the local Milky Way.

The extinction curve used in this work is a description of Fitzpatrick (1999) which treats the extinction from the far ultraviolet up to the infrared (1000-35000 Å). An example for one extinction curve generated using the parametrisation of Fitzpatrick is shown in Figure 3.8. Also plotted are two showcase SEDs, one with high reddening and one without any reddening. The reddening law (black line) associated to the strongly reddend SED shows a quite prominent extinction feature at 2175 Å. This feature is well-described by a Drude profile. The central wavelength seems to remain the same for all sight-lines but the width may vary from region to region (Draine, 2004). One suspects that this feature is either caused by graphite or some carbon molecule.

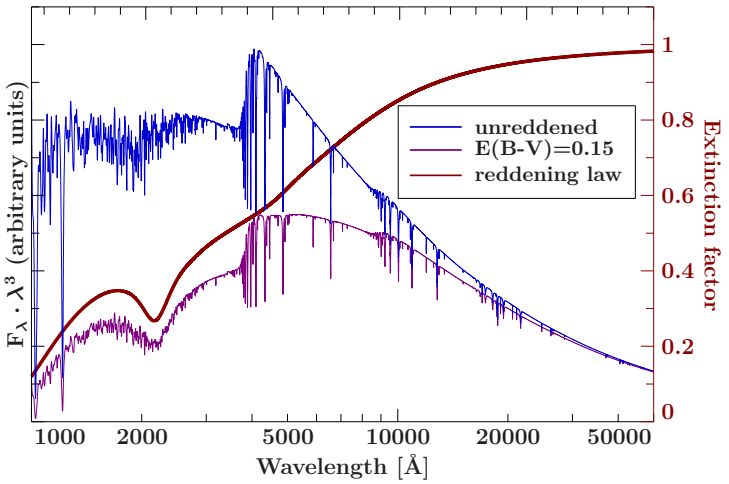


Figure 3.8.: Example for a rather strong reddend SED (red). For comparison the SED of an unreddened star with the same atmospheric parameters is shown in blue. Also plotted is the extinction curve associated to the reddened SED. The color excess E(B-V) is 0.15 and $R_V$ is fixed to 3.1.

The interstellar extinction of every position in the sky has been determined and all-sky extinction maps were created. Schlafly & Finkbeiner (2011) determined the reddening using stars in the SDSS with spectra and compared the observed colors with those derived from the spectra. Schlegel et al. (1998) derived the reddening in the sky from maps of infrared satellites like IRAS and COBE. One should note that the resolution of these maps is rather poor (between a few arcminutes to one degree) and are a proxy to the average extinction along the line of sight because details of the extinction are smeared out.

## 3.6. Color-color-diagram

The deviations of stellar spectra from a blackbody can be visualized quite well in a color-color diagram. In figure 3.9 the color B-V is plotted against the color U-B. The B-V color is proportional to the temperature since it measures the slope in the optical which increases with temperature. The U-B color on the other hand measures part of the ultraviolet region including the Balmer jump. The plotted points in the diagram are the intrinsic colors of main-sequence stars (filled circles) and supergiants (crosses) as a function of spectral type. Also plotted is the locus of blackbodies of different temperature.

For very hot stars like O-type stars there is only a small deviation from the blackbody colors since in these hot stars the Balmer jump has already almost vanished because almost all hydrogen in the stellar atmosphere is ionised. With decreasing temperature the amount of neutral hydrogen in the atmosphere increases which enables increasing absorption below 3600 Å generating opacity. The Balmer jump gets more and more pronounced

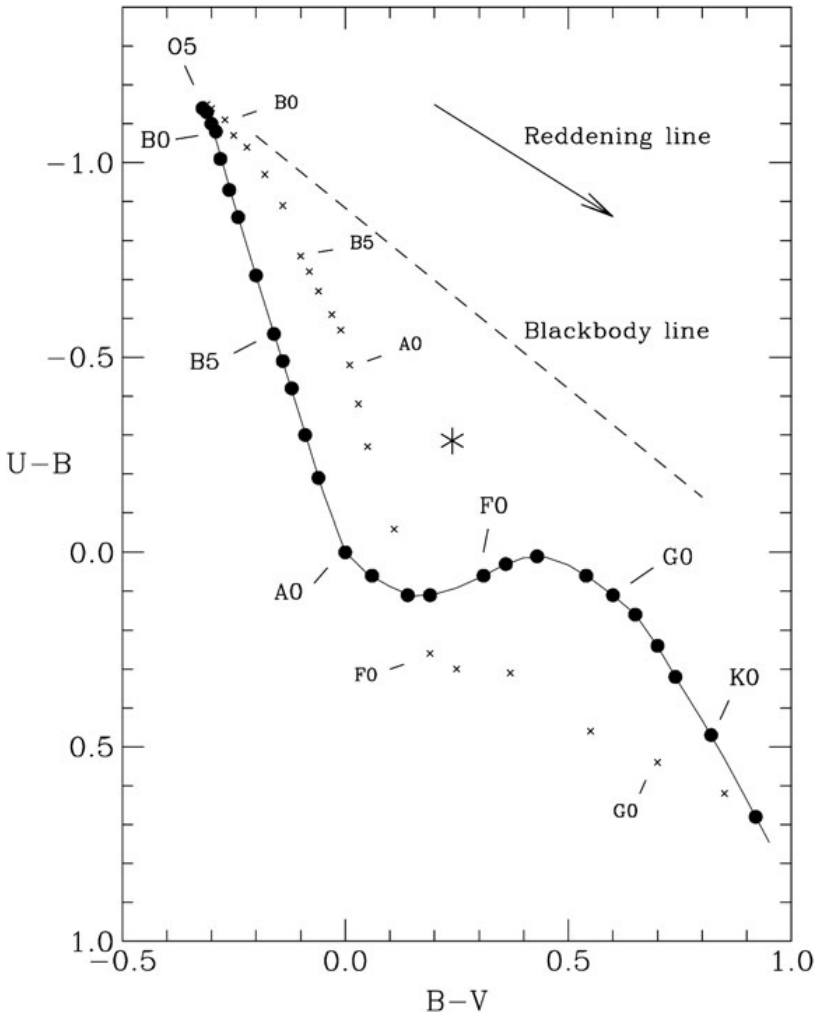


Figure 3.9.: Color-color diagram of UVB photometry. The filled circles indicate the intrinsic colors of main-sequence stars and the crosses stand for supergiants. The dashed blackbody line indicates the color of an object which emits blackbody radiaton. The arrow labeled with "Reddening line" shows the direction an object would shift in the diagram if affected by increasing reddening (Milone & Sterken, 2011).

and the absorption in U increases steadily until to the A-type stars where hydrogen is completely neutral and the discrepancy between main-sequence and blackbody spectrum is the biggest. Below these temperatures the ionization of hydrogen no longer plays a role and the absorption from the $n = 2$ level decreases as the temperature drops. The stellar relation then moves back toward the blackbody line but does not reach it because of $H^-$ opacity and absorption by neutral metals. The deviation from the blackbody again increases for even cooler stars with the occurrence of molecular opacities.

The effect of interstellar reddening can also be extracted from Figure 3.9. The arrow labeled with 'Reddening line' indicates the direction a star would shift in the diagram if there is interstellar dust in the line of sight. Obviously reddening leads to an increase in both B-V and U-B since reddening affects shorter wavelengths more. This means the U magnitude increases relative to B and the B magnitude increases relative to V resulting in an increase in both colors.

## 3.7. Infrared excess and binarity

For some stars the spectral energy distribution shows a much greater flux in the infrared region than expected. This so called infrared excess can be caused by a late-type companion, hot dust surrounding the star or from free-free emission from a stellar wind (Thejll et al., 1995). All these light sources add flux to the spectral energy distribution of the primary in the infrared region.

An infrared excess can also occur when there is a chance alignment of two stars in the sky that lie at different distances. Photometric surveys with high resolution can resolve both stars and measure both separately. Figure 3.10 shows an example where the Sloan Digital Sky Survey can distinguish two separate objects but older surveys like DSS2 or surveys at longer wavelengths like 2MASS cannot resolve the two stars. This leads to problems when combining all these measurements since only one star contributes to the

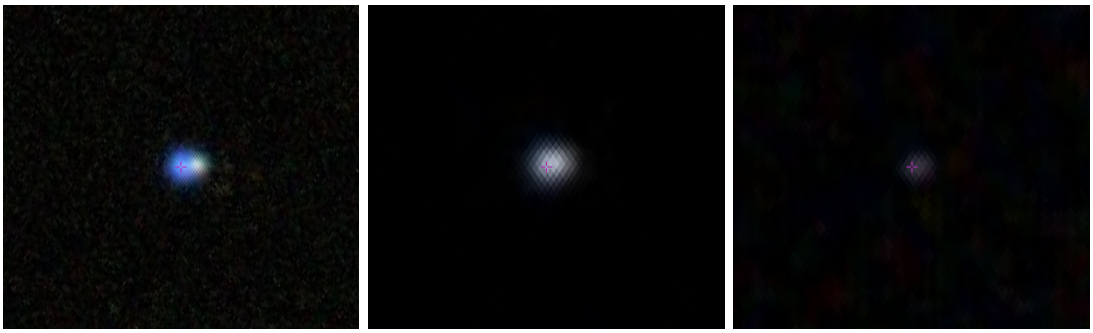

(a) SDSS (b) DSS2 (c) 2MASS

Figure 3.10.: Example of a blended observation. SDSS can resolve two objects. But survey with worse resolution like DSS2 or 2MASS cannot. Source: AladinLite

photometric observation of SDSS whereas in the 2MASS observation the flux of both stars combined is measured.

These optical double stars are not physically connected and are not of interest and therefore omitted.

A gravitationally-bound cool main-sequence companion can be detected in the spectral energy distribution of a hot subdwarf more easily than for a B main-sequence star because the former is more compact and therefore emits less flux than the latter and accordingly does not outshine the companion. The radius of a hot subdwarf is typically of the order of a tenth of a solar radius (between 0.15-0.25 solar radii). This means a solar type companion would be almost ten times larger in terms of radius and a M-type star would have almost the same size. The subdwarf would still remain the major source of radiation since it is much hotter but its radiation maximum is in the ultraviolet to blue region and the flux decreases towards the infrared where the cool companion has its maximum. Figure 3.11 shows an example of a synthetic SED with an infrared excess. Here the

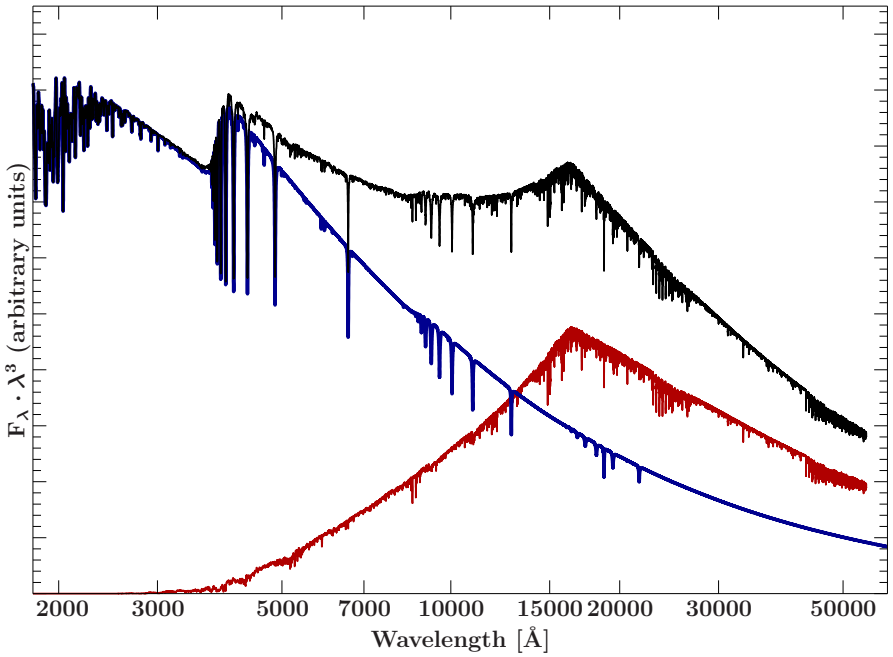


Figure 3.11.: Composite SED (black) of a hot subdwarf star (30000 K, blue) and a cool main-sequence star (5000 K, red)

excess is caused by a main-sequence companion with an effective temperature of 5000 K. The black curve shows the composite SED where the excess between 10000 and 20000 Å is clearly visible. The blue line is the sole SED of the hot subdwarf with an effective temperature of 30000 K. One sees that the composite SED is dominated by the subdwarf in the ultraviolet region and also far into the optical. In the near infrared the SED of the subdwarf and the cool companion (represented by the red curve) contribute equally.

# 4. Photometry

Photometry is the measurement of the apparent brightnesses of objects in the sky using filter sets.

Measurements of this kind were done since ancient times. The Greeks used their naked eye to measure the brightness of stars. The scale used to indicate magnitudes, which is still used today, goes back to Hipparchus and Ptolemy who divided stars visible to the naked eye into six magnitudes. The brightest stars in the sky were said to be first magnitude and the faintest were of sixth magnitude. The system was extended on both ends with the development of telescopes.

The next big step in photometry was the advent of photographic plates which allowed to classify stars concerning their brightness using differential photometry. A big advantage of these plates was that the information was stored permanently and could be looked up at any time. But one should note that the plates where not adapted to astrophysical requirements but were limited by the technical capabilities of the time. Most common for photographic plates were measurements in two bands using a red sensitive and a blue sensitive plate. They have both a wide passband since narrow filters did not exist when photographic photometry was applied and the poor quantum efficiency was unsuitable for narrow filters anyway.

The situation changed with the introduction of photoelectric detectors like photomultiplier or CCD-sensors. Now a choice of passbands regarding the properties of stellar radiation was possible. This led to a large variety of photometric systems. There are systems with broadband filters, which cover a wide range of the spectrum, intermediate ones which can provide more physical information about the stars because they are sensitive to certain features of the star spectrum, and narrow ones which focus on very specific parts of the spectrum.

Information about photometry and different photometric systems can be found in the textbooks by Sterken & Manfroid (1992), Milone & Sterken (2011), Chromey (2010), Budding & Demircan (2007) and Warner (2016) or the publication of Bessell (2005).

## 4.1. Photometric systems

Over time, several photometric systems have been introduced and are defined by filter sets and a set of standard stars, which are tied to the primary standard Vega.

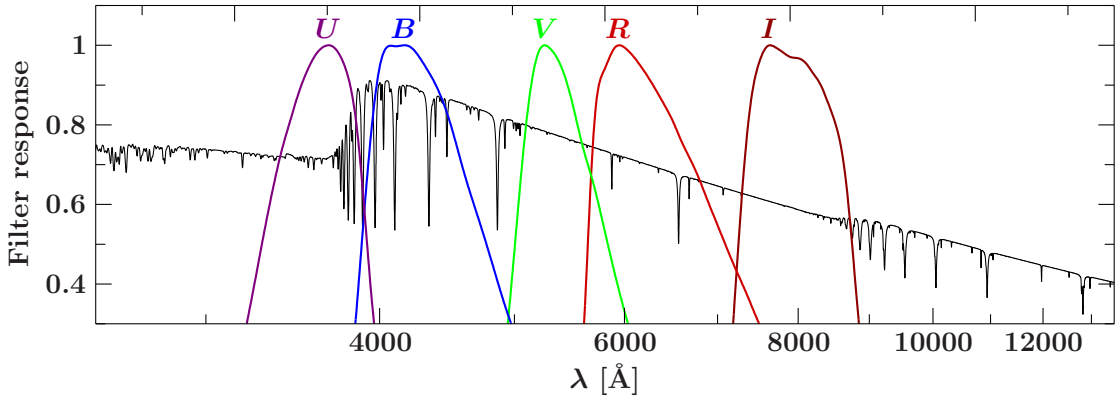


Figure 4.1.: Johnson passbands

| | U | B | V | R | I |
|---|---|---|---|---|---|
| $\lambda_{\text{eff}}$ | 3663 | 4361 | 5448 | 6407 | 7980 |
| $\Delta\lambda$ | 650 | 890 | 840 | 1580 | 1540 |

Table 4.1.: Wavelengths and widths of the Johnson Photometric System in Ångström

### 4.1.1. Visual photometry

#### Johnson $UBV$ photometric System

One of the earliest and most used photometric systems is the $UBV$ system introduced by Johnson & Morgan (1953). The blue $B$ filter was designed to match the photographic bands previously used and the Johnson $V$ should match the photovisual band. The U band provided an important additional band between $B$ and the atmospheric cutoff.

A problem of this system is that originally the short-wavelength cutoff of the U band was not given by the filter response but by the atmosphere. This is not a stable definition since the extinction of the atmosphere changes over time. The long-wavelength cutoff of the V band on the other hand was provided by the detector response. This meant a dependency of the $V$ filter on the temperature and the manufacture of the photomultiplier.

Nevertheless the Johnson photometric system is very suitable for many different astrophysical purposes and became one of the most used photometric systems.

The Johnson $UBV$ system was later extended with two filters in the red ($R$) and infrared ($I$). The definition of these filters commonly used today was given by Bingham & Cousins (1974).

Often not the absolute magnitudes are measured but the difference in magnitudes which is called a color. This is easier to determine because systematic errors, for example from the instrument cancel out. In order to get the absolute value of all colors, the absolute calibration is done very carefully for one magnitude , usually the visual magnitude since

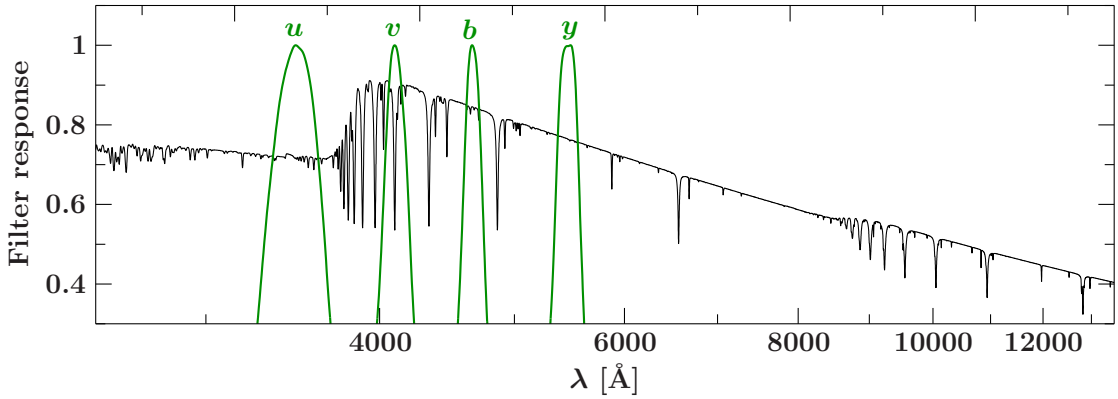


Figure 4.2.: Strömgren passbands

this is a very important one and the effects on the light in this passband are very well investigated.

The visual magnitude in the Johnson system is $V$. All other observations are typically give in colors which are tied to $V$. The colors commonly used in the Johnson system are $U-B$, $B-V$, $V-R$, $V-I$.

For the zero point of the Johnson system Vega was chosen. This means that Vega has a visual magnitude $V_{\text{Vega}} = 0$ and also the colors give zero $(B-V)_{\text{Vega}} = 0$ and $(U-B)_{\text{Vega}} = 0$. Later investigations revealed that $V$ for Vega actually is 0.03.

#### Strömgren *ubvy* photometric system

In contrast to the Johnson System where its passbands are based on historic developments, the Strömgren Photometric System is based on astrophysical considerations. It is optimized for B, A and F stars. It consists of four distinct filters $u$ ultraviolet, $v$ violet, $b$ blue and $y$ yellow (which is actually green). The $y$ passband transforms very well to the Johnson $V$ because at 5480 Å, where the filter is placed, are few absorption lines and the atmospheric transmission as well as the response curves of the detectors are smooth and almost constant. The $u$ band is at 3520 Å blueward of the Balmer discontinuity. The $v$ is centred on the H$\delta$ absorption line. And then there is also a blue filter $b$ at 4688 Å which gives in combination with $y$ a temperature sensitive color index $b-y$. In addition to this color there are two further ones commonly used. The metalicity index $m1 = (v-b)-(b-y)$ and the color index $c1 = (u-v)-(v-b)$ which measures the Balmer discontinuity.

Sometimes the Strömgren photometry is supplemented with two narrow filters around H$\beta$ at 4860 Å. One of them is wide and one is narrow. They give in combination $m_w - m_n$ the $\beta$-index which is free from systematics and interstellar and atmospheric extinction effects. It is a luminosity index for O to mid A-stars and sensitive to the effective temperature for mid A to G stars.

| | u | v | b | y | $\beta_{\text{wide}}$ | $\beta_{\text{narrow}}$ |
|---|---|---|---|---|---|---|
| $\lambda_{\text{eff}}$ | 3520 | 4100 | 4688 | 5480 | 4890 | 4860 |
| $\Delta\lambda$ | 314 | 170 | 185 | 226 | 150 | 30 |

Table 4.2.: Wavelengths and widths of the Strömgren photometric system in Ångström

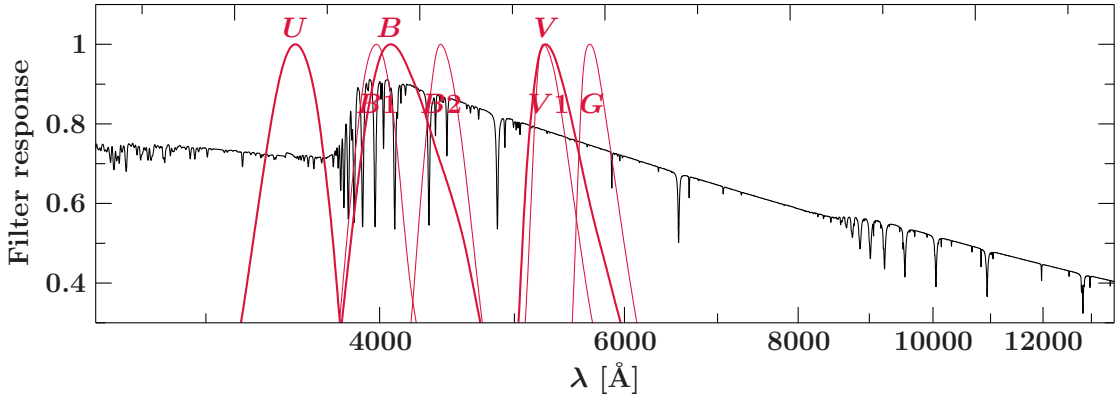


Figure 4.3.: Geneva passbands

### Geneva photometric system

The Geneva photometric system is a 7-color system described by Golay (1966) and it is in-between a wide band and a intermediate band system. It has three wide band filters $UVB$ which are close to Johnson $UVB$. But then there are four additional narrower passbands $B1, B2, V1, G$ which subdivide $B$ and $V$. One should note that all colors are tied to the $B$-magnitude since it is least complicated to measure because it is least sensitive to atmospheric extinction. The whole system is very stable since the defining passbands are accurately known throughout the history of the system and observation and data reduction procedure have not changed since the first day.

| | U | B | B1 | B2 | V | V1 | G1 |
|---|---|---|---|---|---|---|---|
| $\lambda_{\text{eff}}$ | 3438 | 4248 | 4022 | 4480 | 5508 | 5408 | 5814 |
| $\Delta\lambda$ | 170 | 283 | 171 | 164 | 298 | 202 | 206 |

Table 4.3.: Wavelengths and widths of the Geneva Photometric System in Ångström

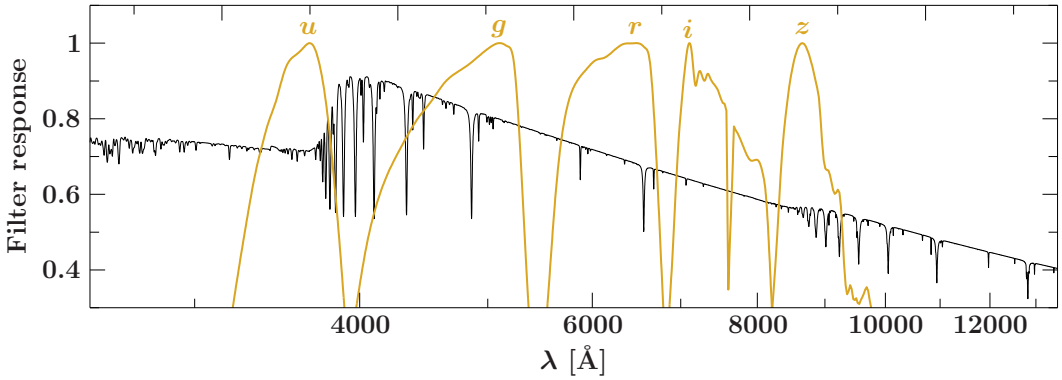


Figure 4.4.: SDSS passbands

| | u' | g' | r' | i' | z' |
|---|---|---|---|---|---|
| $\lambda_{\text{eff}}$ | 3596 | 4639 | 6122 | 7439 | 8896 |
| $\Delta\lambda$ | 570 | 1280 | 1150 | 1230 | 1070 |

Table 4.4.: Wavelengths and widths of the Sloan photometric system in Ångström

### SDSS photometric system

The Sloan Digital Sky Survey (SDSS) is providing a huge amount of photometric observations of stars and galaxies. The newest data release has a sky coverage of about 35%. The photometric system consists of five color bands which divide the range from the atmospheric ultraviolet cutoff to the sensitivity limit of silicon CCDs. The passbands are very wide, some even wider than the Johnson passbands, but still non-overlapping. The broadband character of the filters is needed to ensure high efficiency detection of faint objects. The five filters are

- $u'$ ultraviolet at 3596 Å
- $g'$ green at 4639 Å
- $r'$ red at 6122 Å
- $i'$ infrared at 7439 Å
- $z'$ at 8896 Å

The division of the passbands was chosen to exclude strongest night sky lines like OI at 5577 and HgI at 5460. $u$ was placed shortward of the Balmer discontiuity. This gives, in combination with the $g$-band, a higher sensitivity to the Balmer jump at the cost of a lower throughput.

The SDSS provides several different magnitudes obtained with various methods. There are the Model Magnitudes which assume certain models for the intensity profile of the object. These magnitudes are best used to measure the flux of galaxies. Then there is the

Point-Spread-Function (PSF) Magnitude where the flux of the object is determined by fitting a PSF model to the object. This gives the best results for point sources like stars and therefore will be solely used in the following photometric analysis. An overview of the different magnitudes and a suggestion when to use which magnitude can be found on the web-page of the latest data release (DR12): `http://www.sdss.org/dr12/algorithms/magnitudes/`.

In order to compare the Model magnitude and the PSF magnitude, synthetic magnitudes have been extracted from a large sample of hot subdwarfs (see section 6). Only stars which showed no infrared excess were taken into consideration. This yields approximately 1200 hot subdwarfs. The SEDs were created using all available observations including SDSS. The results are shown in Figure 4.5. The overall conclusion is that the psfMags in general yield better results. The modelMags deviate from the synthetic magitudes between 12th and 16th magnitude in the u and g band and in the z band there seems to be saturation at about 14th magnitude.

The accuracy of the SDSS passbands up to high depths is due to the circumstance that there are barely observations in other photometric systems at this depth and therefore the models used for comparison are solely produced with SDSS observations.

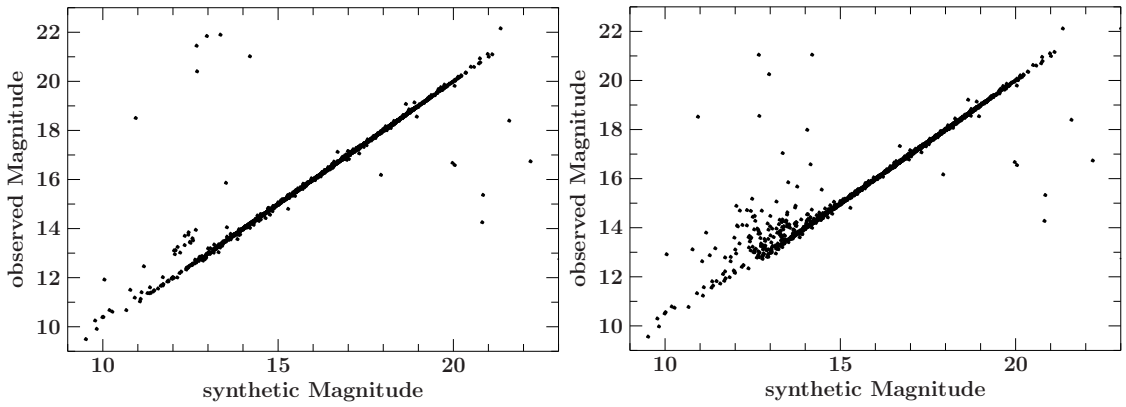


(a) u psfMag




(b) u modelMag

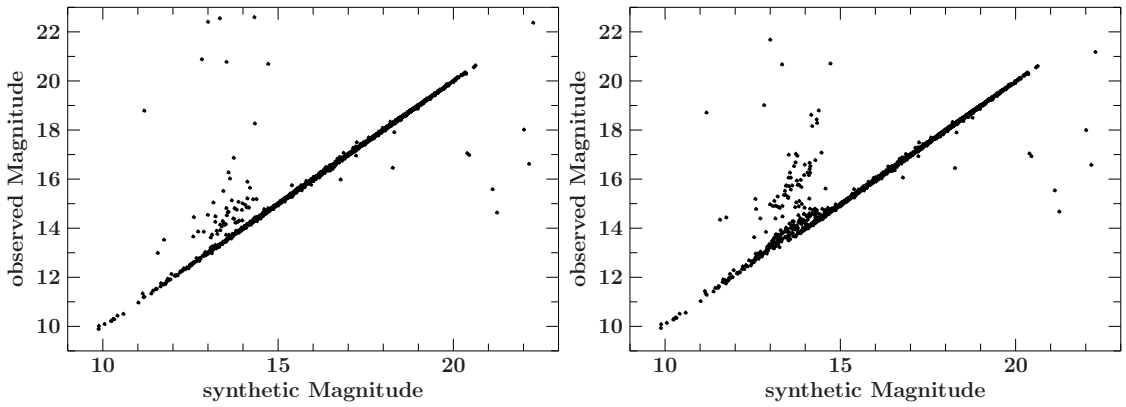


(c) g psfMag




(d) g modelMag

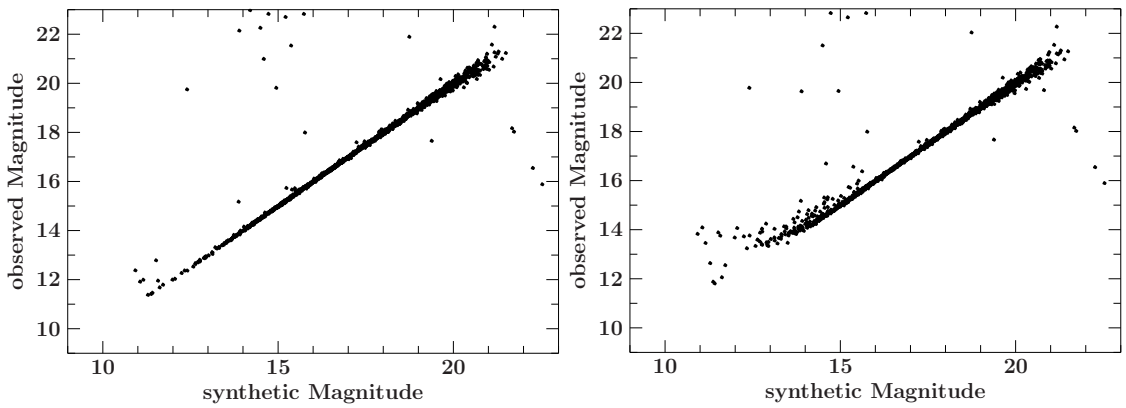


(e) z psfMag




(f) z modelMag

Figure 4.5.: Comparison between observed and synthetic magnitudes of 1200 single sdB stars (from the sample described in section 6) for both the Point-Spread-Function Magnitudes and the Model Magnitudes of the SDSS photometric system

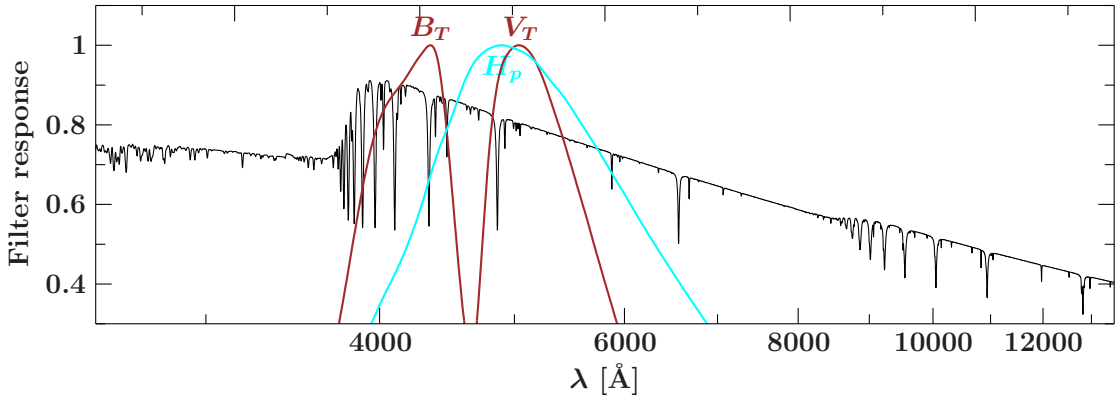


Figure 4.6.: Hipparcos and Tycho passbands

### Hipparcos and Tycho

The Hipparcos mission of the European Space Agency (ESA, 1997) not only provided accurate parallaxes for the nearby stars but also exceedingly precise magnitudes for hundreds of thousands of stars in three independently measured bands (Bessell, 2000).

The main Hipparcos detector provided the $H_p$ magnitude. A very broad passband centred around 5170 Å. For stars brighter than 8.5 a precision of a few tenths of a millimagnitude was reached. In addition, light from the star mapper area was divided by a dichroic beam splitter onto two photomultiplier tubes, providing simultaneously measured $B_T$ and $V_T$ magnitudes. $B_T$ (4217 Å) and $V_T$ (5272 Å) were designed to be close to Johnson $B$ and $V$. The three Hipparcos passbands are plotted on Figure 4.6.

The latest release of Hipparcos data is the Tycho2 catalogue (Høg et al., 2000).

### BATC

The Beijing–Arizona–Taiwan-Connecticut (BATC) Multicolour Survey consists of 15 intermediate-band filters which cover the wavelength range 3000-10000 Å. This system is designed to avoid most of the known bright and variable night-sky emission lines and should provide enough data to create a SED on its own. The goal of the BATC survey is to obtain accurate spectrophotometry for all objects in areas of 1 deg$^2$. The aim is to get 500 areas centered around specific locations like nearby spiral galaxies, various calibration fields, extragalactic objects, as-well as random fields with high Galactic latitudes (Fan et al., 1996). Since the coverage of the sky is rather small (for comparison: the whole sky has an area of approximately 41253 deg$^2$) there are only a few stars that fall into the patches covered by the BATC survey. Within the large sample of over 4400 hot subdwarfs there are only 8 stars which have photometric data in the BATC system (see section 6.1).

The advantage of BATC photometry is that it delivers very accurate photometric data and a good spectral coverage even for very faint and distant stars which are not even

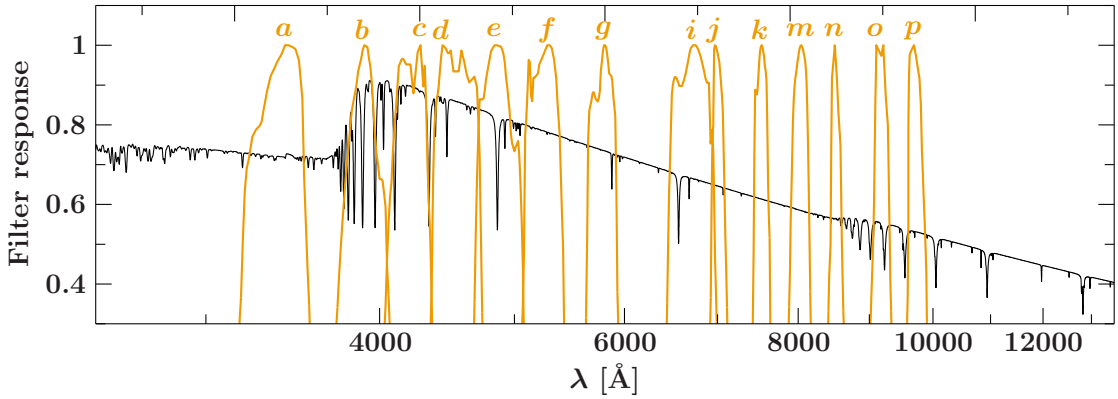


Figure 4.7.: BATC passbands

detected by most other surveys. For example SDSSJ 223740.40+134, which is of 19th magnitude at a distance of approximately 18 kpc. According to Fan et al. (1996) the BATC survey should reach a depth of V=21 mag. But the apparent brightness of such faint objects can only be determined with a 0.3 mag random error.

### APASS photometry

The AAVSO Photometric All-Sky Survey (APASS) is a robotic telescope project by the American Association of Variable Star Observers (AAVSO). They aim at observing the whole sky and measure the position and brightness of 42 million stars with 4 visits per object. There are two robotic telescopes with a 20 cm mirror located at New Mexico and Chile in order to observe both the Northern and the Southern hemispheres. Each telescope is equipped with 5 filters (B,V,g,r,i).

This makes the APASS catalog a very reliable source for both Johnson and Sloan magnitudes. It is valid from about 7th magnitude to about 17th magnitude. The dataset is accessible through the Vizier catalog (Henden et al., 2016).

### Atmospheric extinction

Since most of the observations in the optical are ground-based they are affected by atmospheric extinction. In order to compare these observations to synthetic magnitudes these extinction effects have to be corrected for a priori. These corrections must be determined every night since the atmosphere is not constant. Humidity, smoke or haze, dust and many other sources can affect the transparency of the sky. Also important is the direction the telescope is pointed at since this alters the path length through the Earth atmosphere. The longer the light travels through the atmosphere the more light is extinct. This is measured with the parameter air mass. The shortest way possible is achieved when observing in the zenith. It has an air mass of 1. The way through the atmosphere and consequently the air mass increases as the object gets closer to the

horizon. The air mass $X$ can be determined using the formula $X = \sec(z)$, where $z$ is the zenith distance.

The atmospheric extinction especially affects passbands in the blue and ultraviolet since there the extinction is large and varies significantly across the passband. This increases the uncertainty for ground-based observed U-bands which is quite unfortunate because they are often the only filters shortward the Balmer jump.

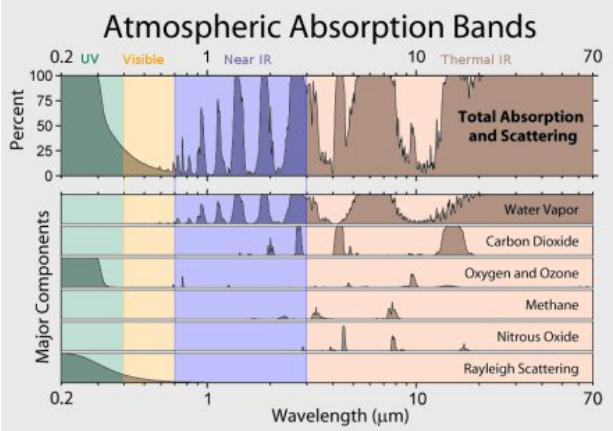


Figure 4.8.: Most light is absorbed by the Earth's atmosphere. Visible light is transmitted but most of the ultraviolet light is absorbed by the ozone layer and water vapor blocks the light in the infrared with the exception of several small windows. Source: `http://ber.parawag.net/images/Atmospheric_Absorption_Bands.jpg`

### 4.1.2. Infrared photometry

The primary objects of infrared astronomy are either very cool substellar objects like brown dwarfs or very distant high redshift objects like galaxies or quasars.

#### 2MASS photometry

The Two Micron All Sky Survey (2MASS) (Skrutskie et al., 2006) is an near infrared survey which was scanning the whole sky from the year 1997 to 2001 at wavelengths from 1.25 $\mu$m to 2.17 $\mu$m. The 2MASS survey uses in principle the infrared extension of the Johnson system (JHK) but the K band has a bluer red cutoff to reduce the effects of thermal emission. Also one should note that the red cutoff of the J band is determined by the atmospheric extinction which varies with the amount of water vapour from night to night. These atmospheric transmission uncertainties limit the precision of 2MASS magnitudes to about 0.04 mag. Also objects brighter than 4th magnitude are saturated in any of the 2MASS passbands. The dataset is accessible through its Vizier catalog (Skrutskie et al., 2006).

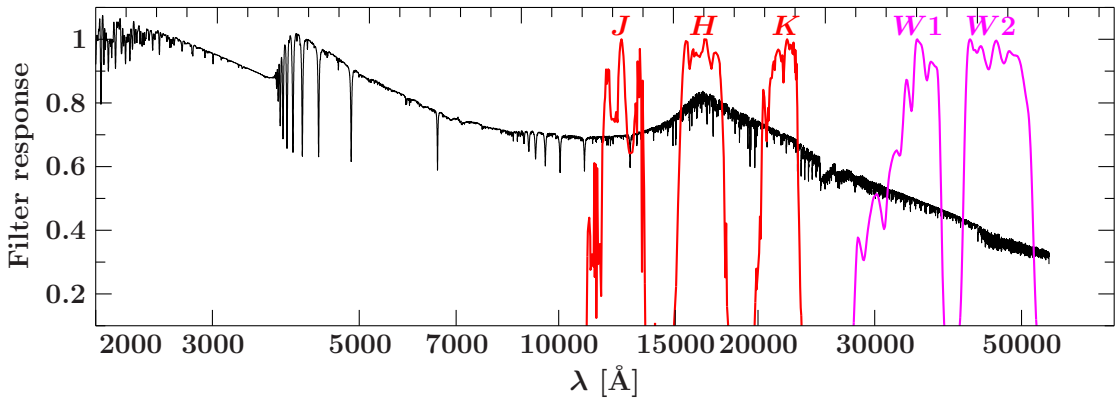


(a) 2MASS and WISE

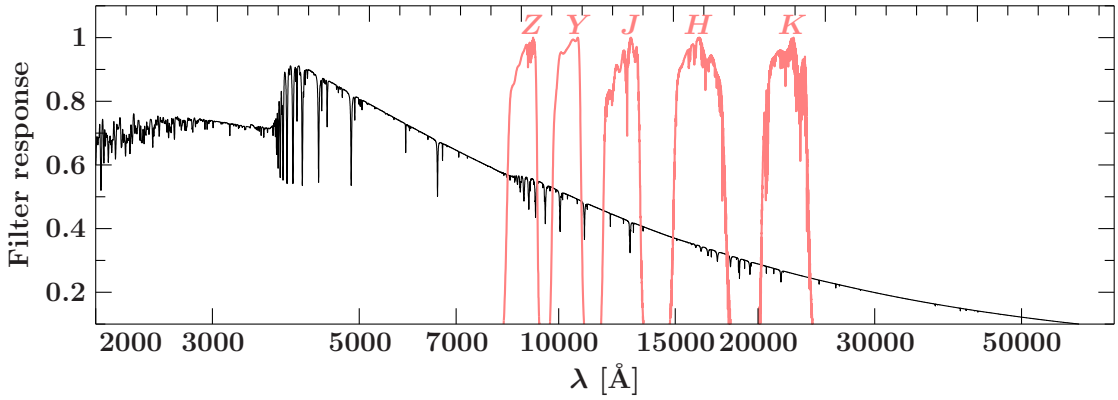


(b) UKIDSS

Figure 4.9.: Infrared passbands. The upper SED is a composite SED with a cool main-sequence component demonstrating the importance of infrared photometry for detecting an infrared excess.

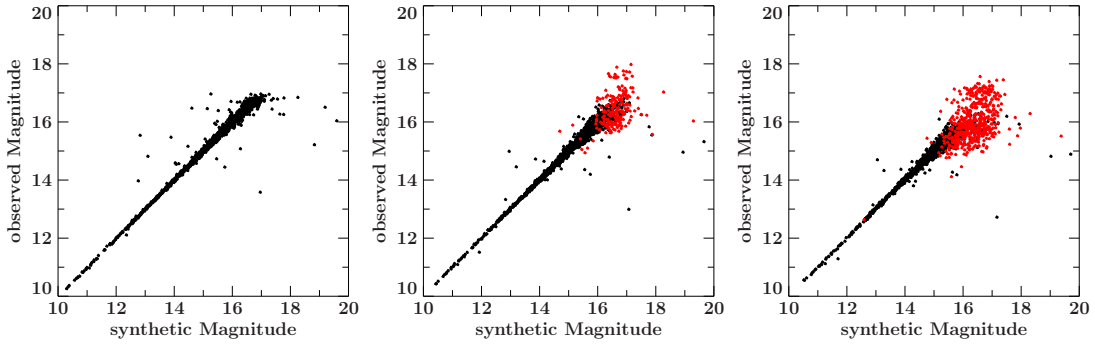


(a) J (b) H (c) K

Figure 4.10.: Comparison between observed and synthetic magnitudes for the three 2MASS passbands. The magnitudes are taken from a sample of 1200 single subdwarfs satars. The red dots are data points which are flagged for bad quality.

To check the accuracy of the 2MASS observations the magnitudes are compared to synthetic ones analogous to the SDSS magnitudes (see Fig. 4.5). The results can be found in Figure 4.10. Although 2MASS published observations deeper than 17th magnitude, looking at Figure 4.10 the uncertainty of 2MASS photometry in the J band is already quite large at 16th magnitude and also the number of outliers increases. For the H and K band it is even worse.

### UKIDSS

The United Kingdom Infrared Telescope (UKIRT) Infrared Deep Sky Survey (UKIDSS) (Hewett et al., 2006) is the successor to 2MASS. UKIDSS began in May 2005 to scan a large fraction of the Northern sky up to 18th magnitude. Thus it is about three magnitudes deeper than 2MASS.

The UKIDSS comes with 5 different filters ZYJHK. In principle the 2MASS photometric system JHK has been adopted but with an extension of 2 filters shortward of 1.2 $\mu$m. These new filters improve the discrimination between brown dwarfs and high-redshift quasars. The Z-Band is related to the sloan $z$ with small adaptions in order to be better suited for the observation of brown dwarfs and quasars (Hewett et al., 2006).

### WISE

The Wide-Field Infrared Survey Explorer (WISE) (Wright et al., 2010) is an infrared space telescope from NASA launched in December 2009. The WISE mission observes the whole sky in mid-infrared and is aimed at finding the coldest stars, near Earth asteroids and ultra-luminous infrared galaxies. The WISE satellite is equipped with

several detectors in order to observe in four different wavelength bands. The passbands W1 to W4 range from 3.4 microns to 22 microns. In this work only the first two passbands W1 and W2 (see Figure 4.9a) are used since the uncertainties on the other two passbands are quite high.

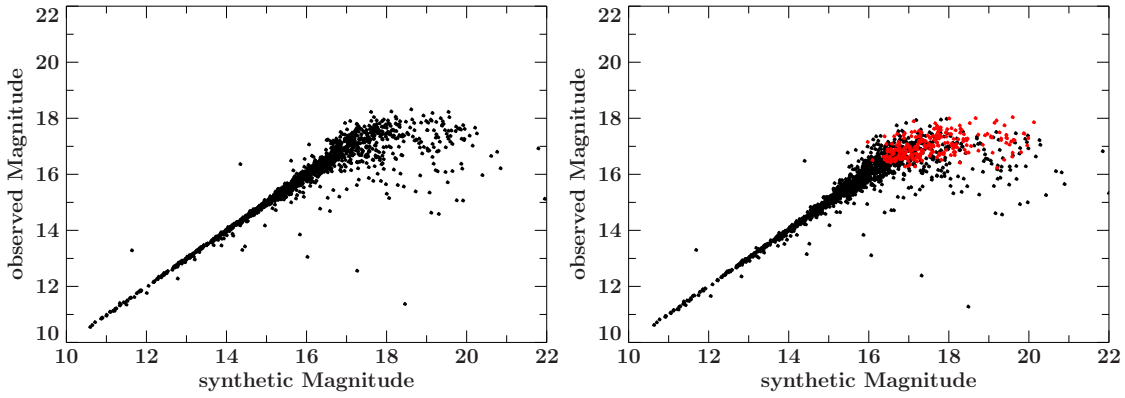


(a) W1 (b) W2

Figure 4.11.: Comparison between observed and synthetic magnitudes for the WISE passbands. The magnitudes are taken from a sample of 1200 single subdwarfs satars. The red dots are data points which are flagged for bad quality.

For the WISE system the comparison between observed and synthetic magnitudes also was done (see Figure 4.11). Already at 15th magnitude the errors of WISE data start to exceed 0.3 mag which is too large to be useful. Also the occurrence of outliers increases. The WISE magnitudes for this work are taken from the ALLWISE vizier catalogue (Cutri & et al., 2013).

### 4.1.3. Ultraviolet photometry

The ultraviolet part of the spectrum ranges from 100 to 3200 Å. It is typically subdivided into near-UV (NUV, 2000-3200 Å) far-UV (FUV 1000-2000 Å) and extreme-UV (EUV 100-1000 Å). Light at these wavelengths is absorbed by the Earth's atmosphere, so observations must be performed from space.

The UV light is well suited for the observation and analysis of hot stars since they emit most of their flux in the ultra-violet.

#### IUE

The International Ultraviolet Explorer (IUE) (Bogges, 1978) was a very important satellite for UV-astronomy. It delivered UV data for 18 years (from 1978 to 1996). The IUE mission obtained over 100000 UV spectra in the wavelength range 1150-3250 Å.

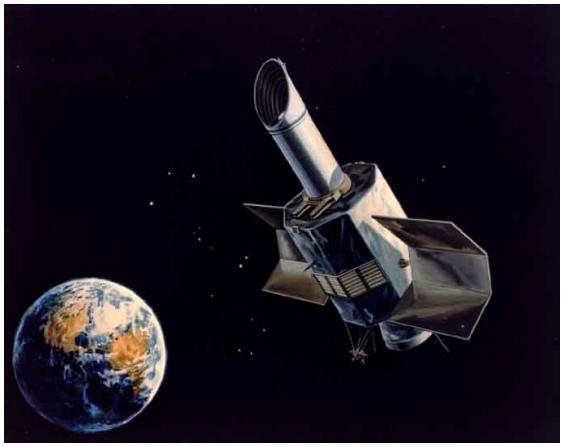

Figure 4.12.: Artistic impression of the IUE satellite orbiting the Earth. (Source: `https://upload.wikimedia.org/wikipedia/commons/1/1b/IUE_1.jpg`)

The satellite was equipped with two independently working spectrographs, one for the long wavelength range (1910-3300 Å) and one for the short wavelengths (1150-1975 Å). Both spectrographs had a prime and a redundant camera. The default cameras were the Long-Wavelength Prime (LWP) and the Short-Wavelength Prime (SWP). The Long-Wavelength Redundant (LWR) camera and respectively the Short-Wavelength Redundant (SWR) would be used if one of the two cameras had failed or would produce errors. Each spectrograph had both high and low resolution modes, with spectral resolutions of 0.2 and 6 Å respectively. The two spectrographs also had two entrance apertures each, a small circular aperture with a 3 arcsec diameter and a large rectangular aperture with the dimensions 10 arcsecs by 20 arcsecs. Since the point-spread-function of the telescope was 3 arcsecs in diameter the small aperture would require very accurate pointing in order to capture all the light of the object and therefore was only used if there was unwanted light from other sources in the field of view.

The large aperture spectra are flux-calibrated and can be used for spectrophotometry. Because we have to combine them with broad and intermediate band optical and infrared photometry we defined a suitable set of filters to derive UV-magnitudes from IUE spectra.

In order to avoid giving them a too strong statistical weight (a typical low resolution IUE spectrum consists of 500 data points) they were broken down into three artificial magnitudes using box filter. This means that the filter response of these artificial magnitudes is 1 within the boundaries of the box and 0 outside. Since the IUE spectrum is discrete this essentially means simply adding up all the fluxes within the range of the box. The position and range of the three boxes was chosen in order to avoid the edges of the spectra because there the uncertainties of the flux grow larger. The region around the Lyman-alpha line at 1215 Å was also excluded because of strong contribution from interstellar gas absorption. Thereby to have same sized boxes one box was chosen to be from 1300 to 1800 Å and therefore covers the spectral range of the short wavelength

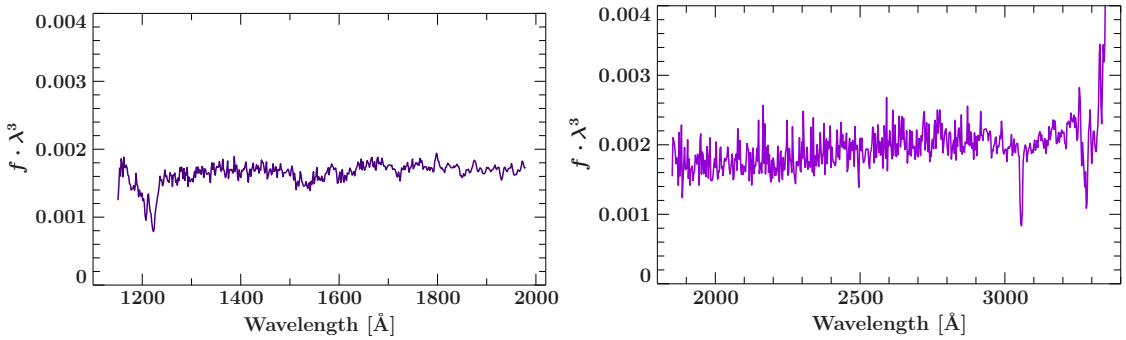


(a) Short-Wavelength Prime

(b) Long-Wavelength Prime

Figure 4.13.: Example of large aperture low resolution spectra of IUE's two spectrographs.

spectrograph and the other two boxes range from 2000-2500 Å and 2500-3000 Å and thus sample the long wave spectrum.

This choice gives the additional advantage that the reddening feature at 2175 Å is well sampled because one box filter lies on top of the bump and the other two enclose it. This increases the sensitivity to interstellar reddening drastically.

For the box filter the low resolution spectra with large aperture were always taken since the flux calibration for low resolution should be better and because details of the spectrum do not matter. Large aperture was taken and well exposed spectra were favoured in order to get spectra with the best signal-to-noise ratio.

Many observations of the IUE satellite are publicly available in the Mikulski Archive for Space Telescopes (MAST). The target can be found via its name or its coordinates and the spectra can be downloaded as ASCII tables.

### GALEX

The Galaxy Evolution Explorer (GALEX) (Martin & GALEX Team, 2005) is an orbiting ultraviolet space telescope launched on April 28, 2003, and operated until early 2012. The GALEX satellite performed an all-sky survey in the ultraviolet. It created a database with more than 200 million point source measurements in its two broad bands, the far-UV (1344-1786 Å) and the near-UV (1771-2831 Å). GALEX reaches a depth up to 21st magnitude in the NUV. One field of interest for GALEX was the observation of white dwarfs (WD). They form as very hot stellar cores with temperatures in the order of 100000 K. As they cool their luminosity shifts from the extreme and far ultraviolet into the near ultraviolet and optical. GALEX can detect these stars at distances of several kiloparsecs. One practical use of white dwarfs is as flux calibration standards. They are very suitable since their SED is continuum dominated, their atmosphere is fully radiative and stable over a wide range of temperatures, the opacities are almost

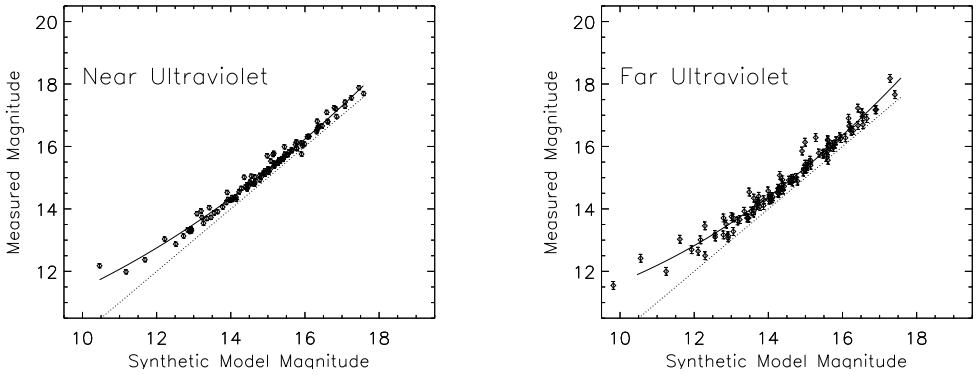


Figure 4.14.: The correlation between the observed GALEX NUV and FUV magnitudes and synthetic magnitudes. The dashed lines are the expected one-to-one correlations (Camarota & Holberg, 2014).

exclusively due to neutral and ionized hydrogen and are thus very well determined, the emergent stellar fluxes depend only on $T_{\rm eff}$ and $\log g$ and therefore can be determined using spectroscopy and because they are relatively close they are only weakly affected by interstellar reddening.

Camarota & Holberg (2014) compiled a sample of 108 white dwarfs with the intention to evaluate the GALEX absolute calibration. Synthetic spectra were computed for each star with atmospheric parameters obtained from spectroscopic analysis. Then synthetic magnitudes in the two GALEX passbands FUV and NUV were extracted and compared to GALEX observations. The empirical correlation between observed GALEX magnitudes and synthetic model fluxes are shown in Figure 4.14. The dashed line indicates a one-to-one correlation. Clearly visible is non-linearity for bright stars which is connected to detector dead-time corrections. But also the overall uncertainty of GALEX observations are relatively high considering the results of Camarota & Holberg (2014) in particular for the FUV band (see Fig. 4.14). That is why GALEX observations in general are not used in this work although the ultraviolet region is quite important for the analysis of hot stars.

### 4.1.4. Summary

In order to obtain the spectral energy distribution of a particular star, all available photometric observations in the various photometric systems discussed above have been collected from Vizier catalogues (Paunzen, 2015; Cutri et al., 2003; Cutri & et al., 2013; Lawrence et al., 2007), the SDSS SkyServer DR12 (`http://cas.sdss.org/dr12/`), Roy Ostensen's Subdwarf Database (Østensen, 2006) and the General Catalogue of Photometric Data (Mermilliod et al., 1997). IUE-spectra were also downloaded from the MAST archive (`https://archive.stsci.edu/`) if available, in order to get photometric measurements in the ultraviolet.

Table 4.5.: Overview over the photometric systems used in this work

| System | Passbands | Source |
|---|---|---|
| | Optical | |
| Johnson | UVBRI | Roy's catalog |
| Strömgren | uvby$\beta$ | Roy's catalog |
| Geneva | U,B,B1,B2,V,V1,G | GCPD catalog |
| SDSS | ugriz | SDSS SkyServer DR12 |
| APASS | B,V,g,r,i | Vizier catalog |
| | Infrared | |
| 2MASS | JHK | Vizier catalog |
| UKIDSS | ZYJHK | Vizier catalog |
| WISE | W1,W2 | Vizier catalog |
| | Ultraviolet | |
| GALEX | NUV,FUV | Vizier catalog |
| IUE | Box-Filter | Mast archive |

Then the data is compared to synthetic photometry extracted from synthetic spectra via $\chi^2$ statistics (see section 4.2). If a passband in one photometric system is completely off it was removed.

## 4.2. Fitting procedure

In order to obtain physical parameters like effective temperature, surface gravity or distance from photometry, one has to compare all the observed magnitudes in the various photometric systems to synthetic magnitudes calculated from a synthetic spectrum and modify the model parameters such that the predicted magnitudes match the observed ones.

Dr. Andreas Irrgang developed in the course of his PhD thesis a fitting procedure for this purpose. His procedure is used in this work and the following description is based on Irrgang (2014).

The magnitude of any photometric passband can be calculated by integrating the flux $f(\lambda)$ arriving at the detector weighted with the filter response function $r_x(\lambda)$. The full definition is given by the following expression

$$\mathrm{mag}_x = -2.5 \log \left( \frac{\int_0^\infty r_x(\lambda) f(\lambda) \lambda \mathrm{d}\lambda}{\int_0^\infty r_x(\lambda) f^{\mathrm{ref}}(\lambda) \lambda \mathrm{d}\lambda} \right) + \mathrm{mag}_x^{\mathrm{ref}} \tag{4.1}$$

Note that the weighted flux of the object of interest is compared to those of a reference object which defines the zero-point of the photometric system. For most systems this reference object is the A-type star Vega. The additional factor $\lambda$ under the integral signs

arises from the assumption of photon-counting detectors (see Appendix E4 of Bessell et al. (1998)).

In order to get synthetic magnitudes from a synthetic spectrum $F(\lambda)$, which describes the flux at the surface of the star, one has to find the flux $f(\lambda)$ a detector would measure if directed at this theoretical star. The first correction is the transition from the surface of the star to the surface of the Earth where the flux is drastically reduced with the distance $d$. Assuming a spherically symmetric object the following relation holds

$$4\pi d^2 f(\lambda) = 4\pi R^2 F(\lambda) \tag{4.2}$$

Since the radius $R$ of the object is in general unknown, we express it with the angular diameter $\theta = \frac{2R}{d}$ and obtain $f(\lambda) = \theta^2 F(\lambda)/4$.

To further account for interstellar extinction the synthetic flux has to be multiplied with a reddening factor $10^{-0.4A(\lambda)}$, where $A(\lambda)$ is the extinction at the wavelength $\lambda$ expressed in magnitudes. $A(\lambda)$ is given as a function of $E(B-V)$ and $R_V = A(V)/E(B-V)$ by Fitzpatrick (1999). $R_V$ is usually close to 3.1 which is the value for the diffuse interstellar medium.

This yields the following expression for calculating the synthetic magnitude

$$\mathrm{mag}_x = -2.5 \log \left( \frac{\theta^2 \int_0^\infty r_x(\lambda) 10^{-0.4A(\lambda)} F(\lambda) \lambda \mathrm{d}\lambda}{4 \int_0^\infty r_x(\lambda) f^{\mathrm{ref}}(\lambda) \lambda \mathrm{d}\lambda} \right) + \mathrm{mag}_x^{\mathrm{ref}} \tag{4.3}$$

To decrease the computation time the synthetic magnitudes are extracted from a pre-calculated grid of spectra. The grid provides synthetic data for a well-defined combination of parameters. For arbitrary values the fitting routine interpolates between consecutive spectra.

To get fairly good starting parameters for the distance, $\theta$ was calculated with formula 4.3 for each passband for a random spectrum. The average of all these $\theta$ was adopted.

An educated guess for a good starting value for E(B-V) can be done by looking at the difference between the observed B-V color and the intrinsic B-V color. If Johnson V or B is lacking Strömgren b-y can be used instead.

### 4.2.1. Uncertainties

In order to determine the confidence intervals for the various fitting parameters $1\,\sigma$ single-parameter confidence limits were computed using the ISIS tool conf_loop. The confidence level search forces the fit to scan the full parameter space. This is very beneficial if the $\chi^2$-landscape is quite complicated which is for instance the case for a composite SED fit because there it often occurs that the fit converges into a local minimum which may not be the best-fit. If an improved fit is found during the confidence limit search, the function updates the internal parameters with the new best-fit and starts over from the beginning. Hence a composite fit should always be done with confidence level search although it is more time consuming because the best fit is rarely found in the first instance.

Table 4.6.: Grid parameters

| | $T_{eff}$ | $\log g$ | He | z |
|---|---|---|---|---|
| sdB | 20000-50000 | 4.6-6.2 | -3.05 | -1 to 1 |
| MS | 2300-12000 | 2-5 | -1.05 | -1 |

## 4.3. Synthetic model grids

For the photometric fitting of composite spectral energy distributions of a hot subdwarf and a cool main-sequqence companion two grids of spectra with various combinations of parameters are needed. For this work the following grids are used.

### 4.3.1. Hot subdwarf star model grid

For the hot subdwarfs the grid was calculated by Dr. Andreas Irrgang using the ATLAS12 code (Kurucz, 1996). The temperature ranges from 15000 K to 55000 K, the surface gravity from 4.6 to 6.2. The wavelengths from 300 Å to 100000 Å (far UV to far infrared) are covered and sampled by 27720 data points.

The metalicity $z$ can vary between -1 and +1. That is either a tenth or ten times the typical composition of a hot subdwarf (see section 2.2). For the elements not listed in Naslim et al. (2013) the reference abundance is solar (Asplund et al., 2009). One should note that iron and nickel are the dominant absorber and have the greatest influence on the metalicity $z$ because they have many absorption lines and their absolute abundance is very large. Very heavy elements like zinc or lead are not even treated by ATLAS because their absolute abundance is so low. An example where the metalicity could be determined quite well is discussed in section 4.5.

The helium abundances was set to a very low value (one hundredth solar) in order to avoid artefacts caused by He II absorption edges in the UV for the hotter models. This barely changes the results of the analysis.

### 4.3.2. Cool main-sequence star model grid

For the cool main-sequence companion a synthetic model grid was downloaded from the Göttingen Spectral Library (`http://phoenix.astro.physik.uni-goettingen.de/`). This grid for is based on the stellar atmosphere code PHOENIX (Husser et al., 2013) and covers the wavelengths from 500-55000 Å. This range is sampled with 47006 data points. Its temperature range is 2300 K to 12000 K, the surface gravity lies within 2 and 5 dex. The helium abundance and the metalicity is fixed to solar.

In order to test the reliability of the Phoenix grid the spectroscopic results of Scholz et al. (2015) for the F-star WISE J0725-2351 were reproduced using the Phoenix grid and checked for consistency. The results are shown in Table 4.7 and Figure 4.15 and are in good agreement with Scholz et al..

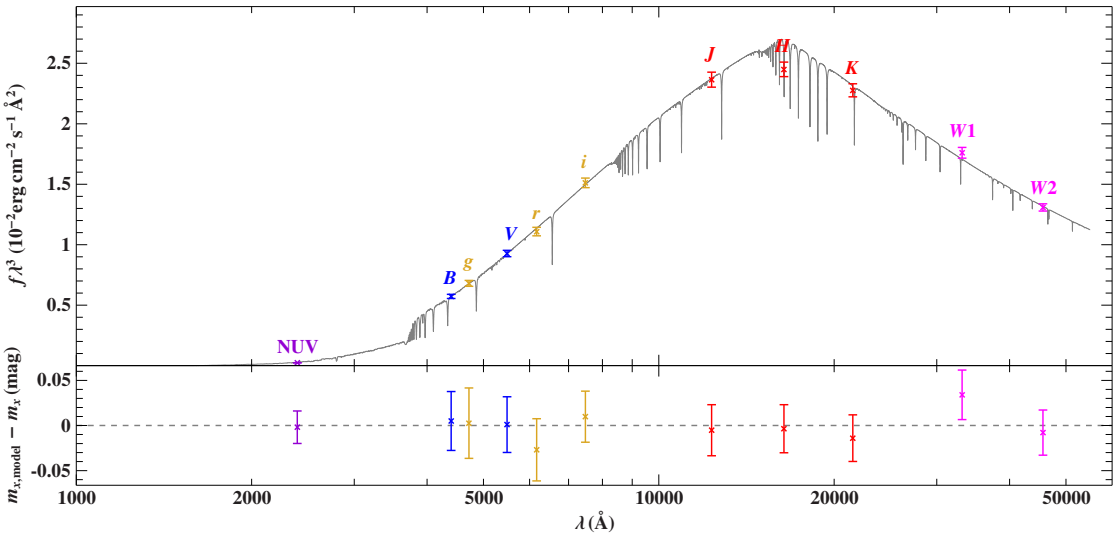


Figure 4.15.: Spectral energy distribution of the F-star WISE J0725-2351

Table 4.7.: Results

| | This work | Scholz et al |
|---|---|---|
| $T_{\mathrm{eff}}[K]$ | $6580^{+230}_{-220}$ | $6250 \pm 100$ |
| $\log g$ | $3.7 \pm 0.4$ | $4.0 \pm 0.2$ |
| E(B-V) | $0.10 \pm 0.04$ | 0.03 |
| $d$ [kpc] | $0.49^{+0.21}_{-0.16}$ | $0.43^{+0.12}_{-0.09}$ |

## 4.4. Example of a single SED

Figure 4.16 shows a prime example where data in almost every photometric system was available. Only GALEX and UKIDSS photometry is missing since this star is too bright for these surveys (Johnson $V = 10.2$).

The main panel of the figure is a graph where the flux $f$ times the wavelength cubed ($\lambda^3$) in units of $\frac{\mathrm{erg\AA}^2}{\mathrm{cm}^2 s}$ is plotted against the wavelength in Ångström. It shows the synthetic spectrum of the best-fitting model (continuous grey line in the background) and, for visualization, the observed magnitudes which are converted into fluxes (colored and labeled bars), are overplotted. The black crosses labeled with 'box' in the left part of the panel (which corresponds to the ultraviolet range) show the three box filter used in this analysis. The horizontal lines indicate the spectral width of the box filter and the vertical line give the uncertainty. The pink line behind the boxes is a visualization of the IUE spectra used to obtain the magnitudes. The other colored bars each represent a passband in one of the photometric systems used. Bars with the same color belong to the same system. From the visual to the infrared the color code of the system is: Johnson-

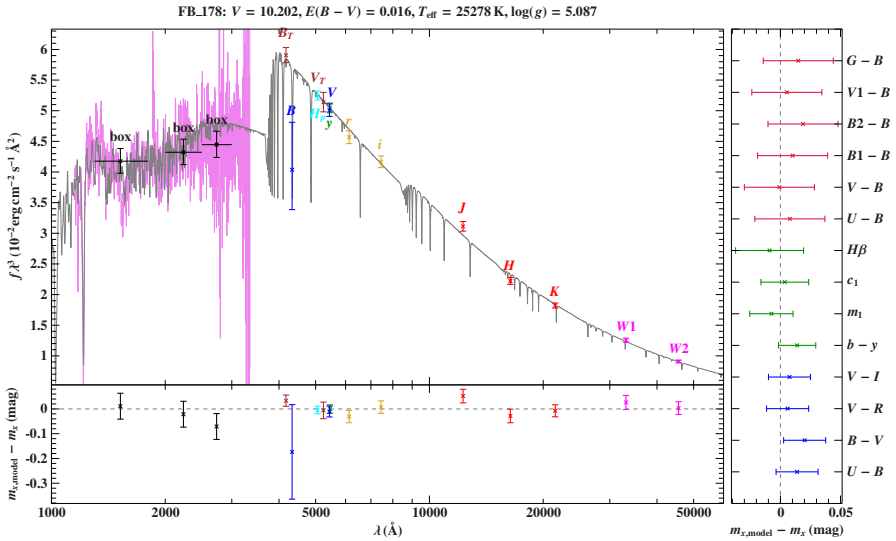


Figure 4.16.: Prime example with data in all major photometric systems. The star modeled here is FB 178 which is one of the brighter sdB stars with a visual magnitude of about 10 mag. It is well described with a single SED. There is no signature of an infrared excess or a cool companion. Resulting $T_{\rm eff}$, $\log g$ and $E(B-V)$ are given on the top of the panel.

Cousin (blue), Strömgren (green), SDSS (goldenrod), Tycho (brown), Hipparcos (cyan), Geneva (crimson), 2MASS (red), WISE (magenta). The colors vaguely correspond to the wavelength they cover. That is why the color of the GALEX passbands, which are not used here, would be violet.

One should note that since the converted magnitudes are tied to the flux of the synthetic spectrum the position of the magnitudes can be misleading. For example here it looks like the Johnson B observation does not fit to the model. But in reality this is not the case. It just happens to be that the effective wavelength of the B passband coincides with an absorption line of the spectrum. Therefore in order to quantify the goodness of the fit the lower panel should be consulted where the difference between the synthetic magnitudes and the observed magnitudes (i.e. the residuals) is plotted. There is an extra panel for the residuals of the colors on the right hand side.

## 4.5. Example of a star with peculiar metalicity

The OB subdwarf Feige 66 is an example of a star where an IUE spectrum is available and also the chemical composition was determined independently using UV spectroscopy (O'Toole & Heber, 2006). This means we can determine the metalicity using the photometric observations and compare to the results of O'Toole & Heber (2006).

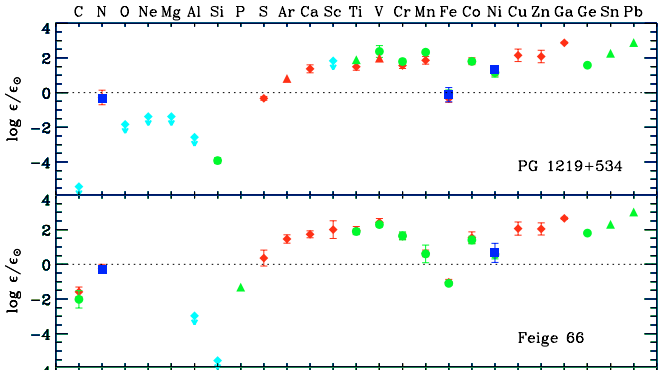


Figure 4.17.: Chemical composition of PG 1234+253 (Feige 66) (O'Toole & Heber, 2006)

Feige 66 has an effective temperature of $T_{\text{eff}} = 33400 \pm 1000\,\text{K}$ and a surface gravity $\log g = 6.2 \pm 0.15$ (Saffer et al., 1994). Also the helium abundance is low ($\log y = -1.800 \pm 0.1$).

The SED fit of Feige 66 (see Figure 4.18a) yielded a slightly lower metalicity than the average ($z = -0.31$). This is in agreement with the results from O'Toole & Heber (2006) (see Figure 4.17) because they found a more than 10 times reduced abundance of iron which influences the opacity through metalicity very much because it has many absorption lines. For comparison and to show the effects of metalicty a fit where $z$ was

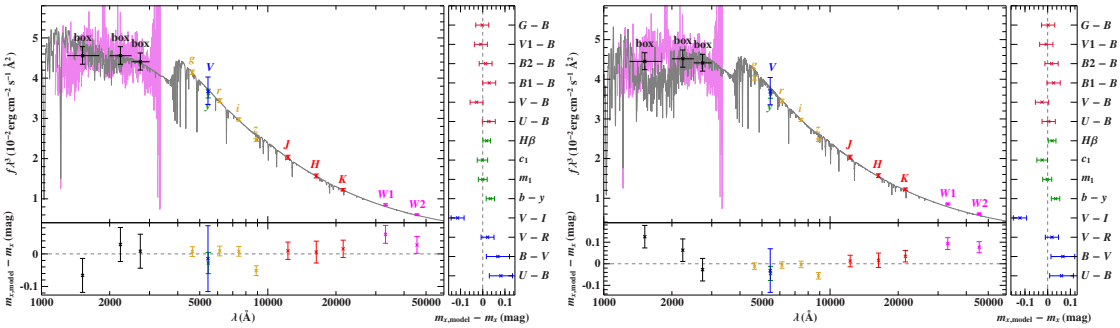


(a) low metalicty (b) high metalicity

Figure 4.18.: SED fit of Feige 66 (a). A low metalicity was found ($z = -0.31$). To show the effects of metalicity a fit where the metalicity was fixed to a high value ($z = 1$) is also shown (b).

fixed to a high value ($z = 1$) is also shown (see Figure 4.18b). One can see that mostly the passbands in the ultraviolet are affected in particular the FUV box. For high metalicity it tends to be too large and for low metalicity it is too small.

## 4.6. Example of a strongly reddened star

There are also stars which are strongly affected by interstellar reddening. One example is the moderately helium-rich and metal-poor sdO star LS IV -12°,1 (Bauer & Husfeld, 1995). The SED is shown in Figure 4.19. The atmospheric parameters of the fit were $T_{\rm eff} = 36000^{+6000}_{-4000}$ K and $\log g = 5.64^{+0.53}_{-0.26}$. For the metalicity a very low value of $z = -1.0^{+0.4}_{-0.0}$ was found, which is in good agreement with the fact that this star is metal-poor. The high interstellar reddening is expressed in the SED by the reddening bump at 2175 Å. The value of $E(B-V)$ was $0.202 \pm 0.009$ for this star. $R_V$ was fixed to 3.1 which is the value for the diffuse interstellar medium. The large amount of interstellar reddening is also visible in the IUE spectrum (pink) and is in agreement with the extinction values from reddening maps ($E(B-V) = 0.2656 \pm 0.0058$ (Schlafly & Finkbeiner, 2011) or $E(B-V) = 0.3089 \pm 0.0067$(Schlegel et al., 1998)). The resulting distance for this fit was $d = 0.115^{+0.130}_{-0.010}$ kpc.

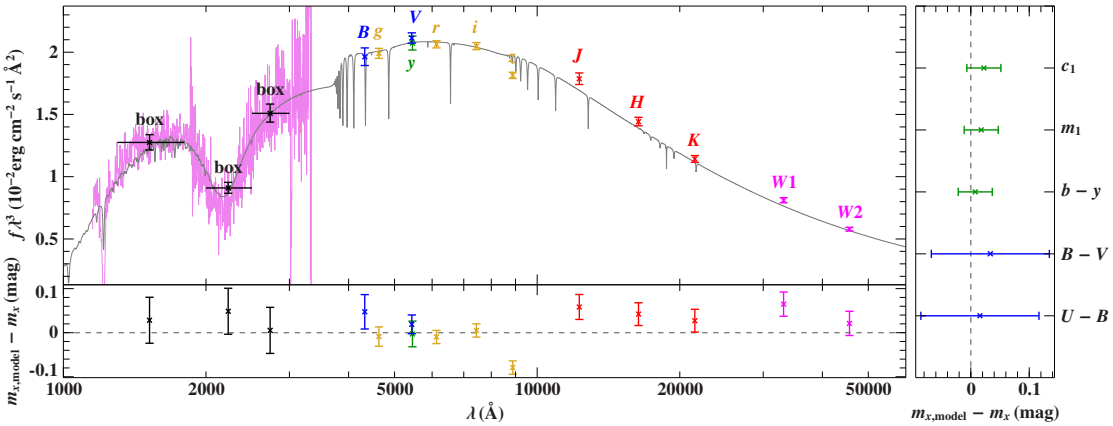


Figure 4.19.: LS IV -12 1, an example of a strongly reddened star ($E(B-V) = 0.2$)

## 4.7. Example of a composite SED

A sizeable amount of stars showed systematics in the residuals like PG 0749+658 (see Figure 4.20a). A first guess was that these systematics are caused by an infrared excess most likely produced by a cool companion. In order to handle this infrared excess the spectrum of a blackbody was added to the spectral energy distribution of the hot subdwarf. The resulting SED can be seen in Figure 4.20b. As one can see easily the quality of the fit increases drastically but especially in the infrared region small deviations from the actual data remain. This is presumably because there is some discrepancy between the spectrum of a cool star and a blackbody (see figure 3.2a) especially in the infrared where a drop in $H^-$-opacity causes an increase in flux at around 17000 Å.

To further increase the quality of the fit instead of a blackbody the spectral energy distribution of a cool main-sequence star was added to the SED of the hot subdwarf and the composite spectral energy distribution was fitted to the data. The results are shown in Figure 4.20c and yield a very convincing model. The effective temperature of the sdB is $T_{\rm eff} = 22400^{+500}_{-400}$ K and the surface gravity $\log g = 5.55^{+0.14}_{-0.17}$. For the companion an effective temperature of $4750 \pm 80$ K was found. The ratio of the surfaces is $A_{\rm c}/A_{\rm sd} = 17.2^{+0.9}_{-1.2}$. The star is not reddened by interstellar extinction and has a distance $d = 320^{+80}_{-60}$ pc.

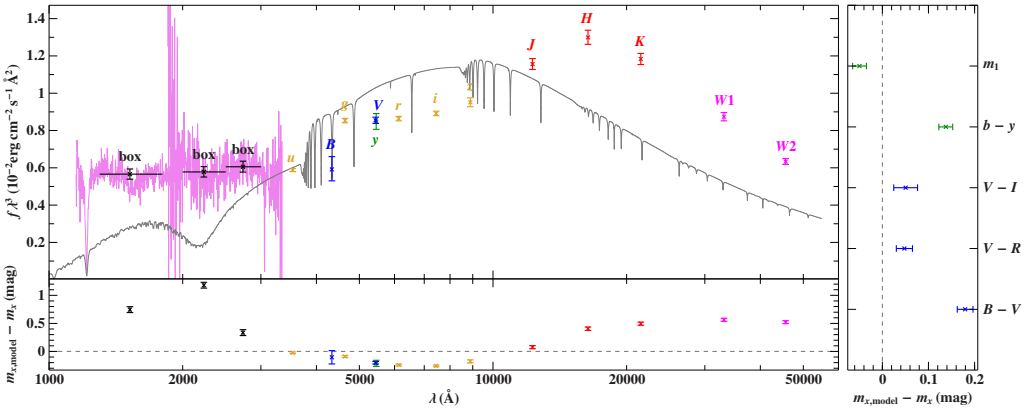


(a) Single SED

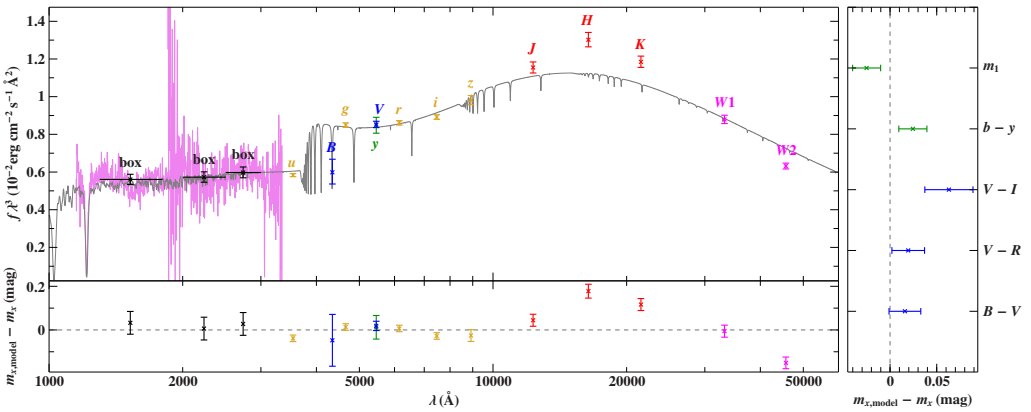


(b) Composite with blackbody

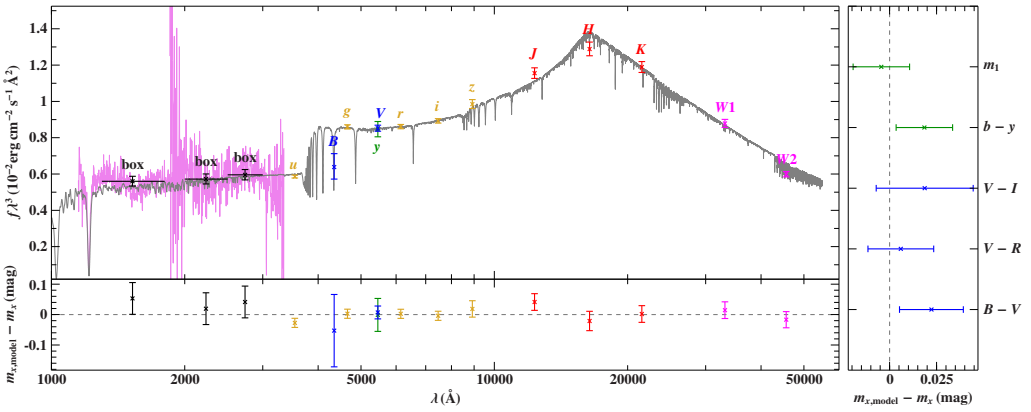


(c) Composite with cool main-sequence companion

Figure 4.20.: PG 0749+658 was modeled with a single SED of a hot subdwarf (a) but showed systematics in the residuals. In a first try the spectrum of a blackbody was added to the star's SED (b). Since there were still deviations especially in the infrared part of the SED a composite SED of a hot subdwarf and a cool main-sequence star was fitted (c) which yields a very convincing model.

# 5. Application to different samples of hot subdwarfs

The fitting procedure discussed above was applied to five different samples of hot subdwarfs.

1. Sample of known binaries, most companions unseen, but RV curve reduced (Kupfer et al., 2015).
2. Sample of 105 single or wide binaries (Geier & Heber, 2012).
3. Homogeneous sample of 76 sdB stars from SPY with high quality UVES spectra (Lisker et al., 2005).
4. Sample of 181 subdwarfs in the Tycho catalog in preparation of the upcoming Gaia data release.
5. Large sample of more than 4400 hot subdwarfs compiled from all larger subdwarf catalogs by Dr. Stephan Geier.

## 5.1. Quality rating system

Since the quality of the fits depend on the number of observations and on which parts of the spectrum are covered a rating system was introduced to quantify the quality of the observational basis. Grades from 1 to 6 indicate for each star what kind of observations are available.

A rating of 6 is the worst grade and indicates that there are only observations in the optical (Johnson, Strömgren, Geneva, SDSS) excluding the U-band.

If there is in addition a U-band observation like Johnson $U$ or the Stömgren color index $c1$ which contains the Strömgren $u$ passband, a rating of 5 is awarded because this significantly improves the validity for the fit of the hot subdwarf since the Balmer jump is sampled. But due to the lack of infrared observations no statement about a companion can be made.

Therefore the rating of 4 is awarded when there are magnitudes in the optical (but no U-Band) and the infrared (2MASS, UKIDSS, WISE). This allows to detect and characterize potential companions.

If there is infrared photometry and a U-Band observation the rating will be 3.

The second best rating is awarded when there are also observations in the ultraviolet since this significantly improves the fit because it enables to determine the metalicity and makes the fit very sensitive to interstellar reddening and is a good consistency check for the U-band observations.

Table 5.1.: Quality rating system

| Rating | Observations |
|---|---|
| 1 | Hbeta+Ultraviolet+Optical+U-band+Infrared |
| 2 | Ultraviolet+Optical+U-band+Infrared |
| 3 | Optical+U-band+Infrared |
| 4 | Optical+Infrared |
| 5 | Optical+U-band |
| 6 | Optical |

A rating of 1 is awarded when there is in addition an observation in the narrow band filter $H_\beta$ of the Strömgren photometric system because this gives the possibility to constrain the surface gravity of the star. The grading system is summarized in Table 5.1.

## 5.2. Short period binary systems

The first sample is a list of 142 spectroscopically analysed sdB stars which showed radial velocity variability (Kupfer et al., 2015). The atmospheric parameters $T_{\rm eff}$ and $\log g$ from Kupfer et al. (2015) are plotted in Figure 5.1.

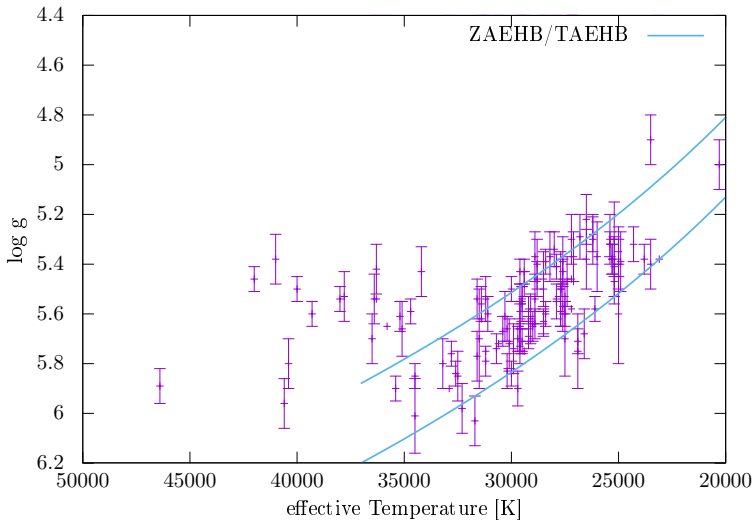


Figure 5.1.: Spectroscopic values for the short-period sample (Kupfer et al., 2015) in the $T_{\rm eff} - \log g$ diagram. Most of the stars lie between the theoretical Zero-Age EHB and the Terminal-Age EHB.

The RV-curve has been solved for all stars and therefore the period $P$ and the semi-

amplitude $K$ are known which allows the calculation of the mass function:

$$f_m = \frac{PK^3}{2\pi G} = \frac{M^3 \sin^3(i)}{(M + M_{\mathrm{sdB}})^2} \,. \tag{5.1}$$

This means all these stars should have an unseen companion whose mass can be limited by the mass function when assuming the canonical mass ($0.47\,\mathrm{M}_\odot$) for the hot subdwarf.

The companion can either be a white dwarf which should not contribute to the flux of the subdwarf or a low-mass main-sequence star. Substellar objects like brown dwarfs or planets are also possible. For some stars the nature of the companion can be deduced from a spectroscopic analysis. If the companion is a bright low-mass main-sequence star the spectrum should be double-lined caused by the Doppler motion of the two stars. If there is no sign of a companion in the spectrum, the object is either a dim normal star or a white dwarf.

The SEDs of these stars can be used as a consistency check. For a white dwarf companion one would not expect any contribution in the spectral energy distribution of the companion because white dwarfs are much more compact than hot subdwarfs. If on the other hand the companion is a cool main-sequence star there should be a contribution in the infrared and a composite SED has to be fitted.

But two components fits have many free parameters ($\mathrm{T_{eff,sd}}$, $\log g_{\mathrm{sd}}$, $\mathrm{T_{eff,comp}}$, $\log g_{\mathrm{comp}}$, $A_{\mathrm{c}}/A_{\mathrm{sd}}$, E(B-V), $\theta$) which leads to degeneracy making it more difficult to find the best suiting fit. Also the surface gravities of both the subdwarf and its companion are difficult to constrain. The mass function helps since it is possible to express the surface ratio $A_{\mathrm{c}}/A_{\mathrm{sd}}$ in terms of the mass ratio which can be extracted from the mass function. The total flux of the composite spectrum is given by the following equation

$$F_{\mathrm{tot}}(\lambda) = \frac{1}{d^2}\left(R^2_{\mathrm{sdB}} F_{\mathrm{sdB}}(\lambda) + R^2_{\mathrm{MS}} F_{\mathrm{MS}}(\lambda)\right) \tag{5.2}$$

As one can see the fluxes of the hot subdwarf and the main-sequence star are scaled with respect to each other by the ratio of the radii squared. But they can be substituted using Newton's third law $g = \frac{GM}{R^2}$ which yields

$$F_{\mathrm{tot}}(\lambda) = \frac{GM_{\mathrm{sdB}}}{d^2 g_{\mathrm{sdB}}}\left(F_{\mathrm{sdB}}(\lambda) + \frac{1}{q}\frac{g_{\mathrm{sdB}}}{g_{\mathrm{MS}}}(\lambda)\right) \tag{5.3}$$

with the mass ratio $q = \frac{M_{\mathrm{sdB}}}{M_{\mathrm{MS}}}$. This leads to a surface ratio that only depends on the ratio of the surface gravities and the mass ratio $q$ which can be deduced from the mass function (eq. 5.1). Note that the mass function introduces a new free parameter, the inclination $i$. However in contrast to the surface ratio, the inclination is constrained to values between 0 and 90 degrees.

Kupfer et al. (2015) could identify a white dwarf companion for 52 systems using the mass function which gives a limiting lower mass at the maximal inclination of 90 degree. If this limiting mass exceeds a certain value the companion should be visible in the spectrum. If not it is most likely a white dwarf.

50 of the 52 systems could be modelled with a single SED which confirms a white dwarf companion. No infrared excess was in sight. Two systems showed a signature of a companion in the SED (PG 1101+249, LB 1516). These systems might be hierarchical triple systems where a main-sequence star orbits a WD/sdB-binary.

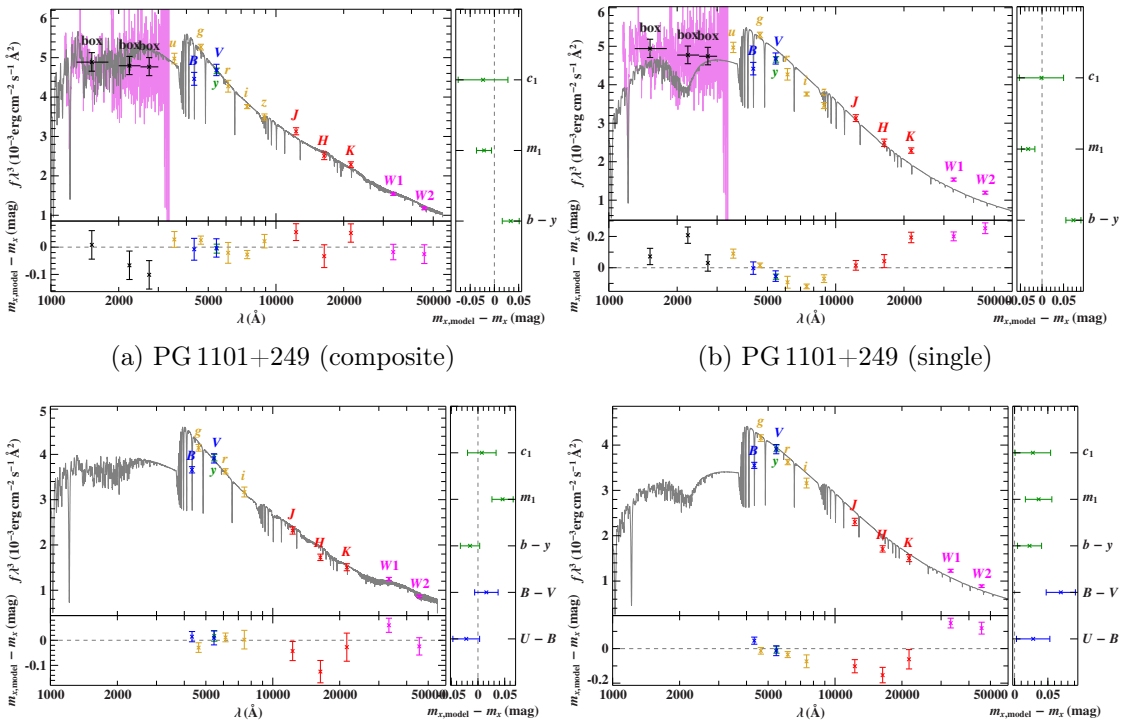


(a) PG 1101+249 (composite)

(b) PG 1101+249 (single)

(c) LB 1516 (composite)

(d) LB 1516 (single)

Figure 5.2.: Kupfer et al. (2015) states a WD companion but an infrared excess was found in the SED.

For 28 stars Kupfer et al. (2015) suggest a main-sequence companion because it either shows up in the spectrum or a reflection effect was observed. The small separation between the subdwarf and its companion causes a heat up on one side or one spot of the companion which leads to a varying flux emission depending on the orbital phase of the binary system. These systems are therefore not analysed in this work since time-resolved photometry in all passbands would be necessary in order to describe these stars properly. But most of the time only observations without known orbital phase are available. Moreover most of these systems are already well-described because the combination of light-curve and radial-velocity curve allows to fully solve the system and to determine all relevant parameters of the system. A list of the 26 stars that show a reflection effect can be found in Table 5.2. Two of these stars have a brown dwarf companion instead of a main-sequence star (SDSS J082053.53+000843.4, SDSS J162256.66+473051.1).

Table 5.2.: Stars in the Kupfer sample which are known to show a reflection effect

| | | | |
|---|---|---|---|
| HW Vir | HE 0230-4323 | KIC 9472174 | ASAS J102322-3737.0 |
| JL 82 | V1405 Ori | EC 10246-2707 | GALEX J032139.8+472716 |
| KBS 13 | PG 1438-029 | HS 2231+2441 | 2MASS J15334944+3759282 |
| PHL 457 | PG 1329+159 | NSVS 14256825 | SDSS J192059.77+372220.0 |
| AA Dor | CPD-64 481 | HS 0705+6700 | SDSS J082053.53+000843.4 |
| Lan 30 | HS 2333+3927 | PG 1017-086 | SDSS J162256.66+473051.1 |
| PG 1336-018 | BPS CS 22169-0001 | | |

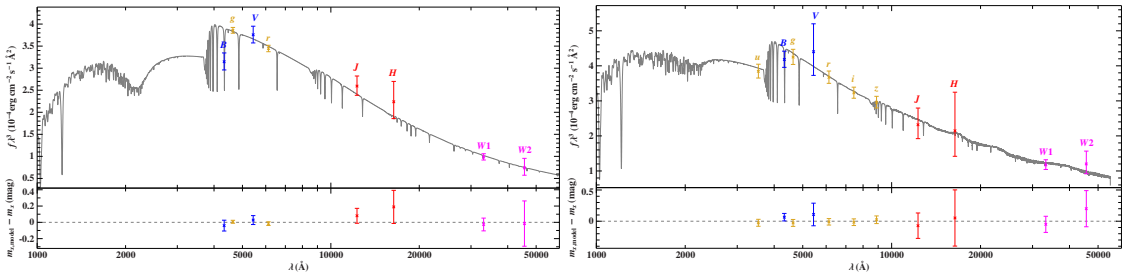

(a) HE 1421-1206 (b) SDSS J012022.94+395059.4

Figure 5.3.: Two stars where a main-sequence companion has been identified by Kupfer et al. (2015). Only SDSS J012022.94+395059.4 could be modelled with a composite spectrum ($T_{eff,comp} = 2700$ K).

This leaves 4 stars where a companion was detected within the stellar spectrum:

- OGLE BUL-SC16 335: Here the SED could not be constructed due to insufficient data points. This is because this star is in a very crowded field in the Galactic bulge.
- HE 1421-1206 showed no signature of a companion in the SED. But the number of available observations for this star is very low and also their quality is poor (see Fig. 5.3a).
- HS 2043+0615 also has insufficient data points.
- SDSS J012022.94+395059.4 showed a very small infrared excess which could be described with a very cool main-sequence star ($T_{eff,comp} = 2700$ K). The composite SED fits are shown (see Figure 5.3b).

60 systems remain where the spectroscopic analysis left the nature of the companion unclear. 49 stars could be modelled with a single SED suggesting a white dwarf companion. 10 systems show an infrared excess and are modelled with a composite SED (see Table 5.3).

Table 5.3.: Results of the composite SED fits in the Kupfer sample. The atmospheric parameters of the subdwarf where fixed within the uncertainty of the spectroscopic values if available.

| Object | $\frac{T_{eff,sd}}{T_{eff,MS}}$ [K] | $\frac{\log g_{sd}}{logg_{MS}}$ | z | E(B-V) | $\theta \cdot 10^{-12}$ | $\frac{A_c}{A_{sd}}$ | $i$ [°] | Qual. |
|---|---|---|---|---|---|---|---|---|
| PG 0850+170 | $26600^{+\ 900}_{-\ 500}$<br>$2900^{+800}_{-600}$ | $5.27^{+0.15}_{-0.00}$<br>$4.80^{+0.21}_{-0.33}$ | $-1.00^{+1.05}_{-0.00}$ | $0.00^{+0.01}_{-0.01}$ | $10.74^{+0.21}_{-0.24}$ | 3 | $90^{+\ 0}_{-61}$ | 3 |
| EGB 5 | $33810^{+\ 1380}_{-\ \ \ 0}$<br>$2300^{+321}_{-\ \ 0}$ | $5.85^{+0.11}_{-0.10}$<br>$5.00^{+0.00}_{-1.00}$ | $+0.55^{+0.46}_{-1.55}$ | $0.00^{+0.02}_{-0.00}$ | $8.57^{+0.27}_{-0.41}$ | 18 | $13^{+77}_{-\ 2}$ | 3 |
| PB 5333 | $39788^{+\ 1624}_{-\ \ \ 0}$<br>$4300 \pm 200$ | $5.86^{+0.20}_{-0.00}$<br>$5.00^{+0.00}_{-0.21}$ | $+0.18^{+0.33}_{-0.45}$ | $0.04^{+0.01}_{-0.01}$ | $12.35^{+0.31}_{-0.34}$ | 28 | $6^{+\ 3}_{-\ 0}$ | 2 |
| SDSSJ183249.0 | $27000^{+\ 600}_{-\ 900}$<br>$2500^{+8300}_{-\ 300}$ | $5.38^{+0.00}_{-0.18}$<br>$4.23^{+0.77}_{-0.76}$ | $+1.00^{+0.00}_{-2.00}$ | $0.09^{+0.04}_{-0.10}$ | $4.47^{+0.49}_{-1.23}$ | 15 | $90^{+\ 0}_{-78}$ | 3 |
| SDSSJ011857.2 | $28200^{+\ 300}_{-\ 1000}$<br>$2900^{+1100}_{-\ 500}$ | $5.48^{+0.15}_{-0.00}$<br>$3.98^{+1.02}_{-0.09}$ | $+1.00^{+0.00}_{-2.00}$ | $0.06^{+0.02}_{-0.03}$ | $6.51^{+0.53}_{-0.26}$ | 15 | $90^{+\ 0}_{-78}$ | 3 |
| SDSSJ204613.4 | $30968^{+\ 749}_{-\ \ \ 0}$<br>$3500^{+1200}_{-1100}$ | $5.44^{+0.20}_{-0.00}$<br>$4.23^{+0.78}_{-0.15}$ | $-1.00^{+1.26}_{-0.00}$ | $0.05^{+0.03}_{-0.04}$ | $3.45^{+0.12}_{-0.23}$ | 12 | $90^{+\ 0}_{-74}$ | 3 |
| PG 0940+068 | $26200^{+\ 4100}_{-\ 1300}$<br>$2800^{+400}_{-500}$ | $5.78^{+0.13}_{-1.19}$<br>$5.00^{+0.00}_{-1.39}$ | $+1.00^{+0.00}_{-2.00}$ | $0.05^{+0.02}_{-0.02}$ | $11.81^{+0.26}_{-0.32}$ | 8 | $90^{+\ 0}_{-66}$ | 3 |
| PG 1253+284 | $28000^{+\ 4900}_{-\ 2600}$<br>$6600 \pm 200$ | $6.09^{+0.11}_{-0.67}$<br>$3.99^{+0.69}_{-0.58}$ | $+1.00^{+0.00}_{-0.82}$ | $0.11^{+0.07}_{-0.07}$ | $13.10^{+4.43}_{-3.70}$ | 32 | $90^{+\ 0}_{-73}$ | 1[1]* |
| PG 1247+554 | $31000^{+\ 4400}_{-\ 1900}$<br>$5000 \pm 200$ | $6.20^{+0.00}_{-0.34}$<br>$5.00^{+0.00}_{-0.84}$ | $+0.47^{+0.53}_{-1.48}$ | $0.00^{+0.01}_{-0.00}$ | $14.60^{+1.42}_{-1.32}$ | 83 | $6^{+12}_{-\ 2}$ | 2 |
| SDSSJ095101.2 | $25600^{+\ 5900}_{-\ 1800}$<br>$4800^{+300}_{-400}$ | $4.90^{+1.31}_{-0.30}$<br>$3.50^{+1.51}_{-0.35}$ | $+1.00^{+0.00}_{-2.00}$ | $0.02^{+0.01}_{-0.02}$ | $3.85^{+0.27}_{-0.29}$ | 12 | $90^{+\ 0}_{-80}$ | 3 |

[2]

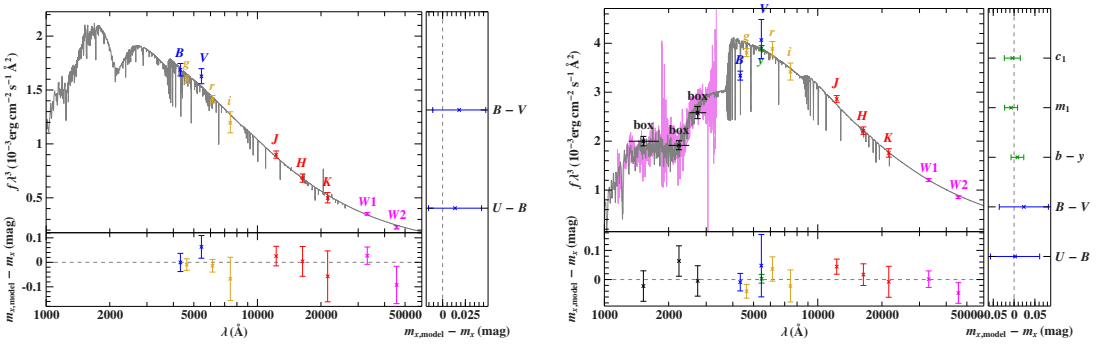


(a) EC 00042-2737 (b) EC 19563-7205

Figure 5.4.: Two stars that show no infrared excess although according to Geier & Heber (2012) a companion is visible in the spectrum.

## 5.3. Single and wide binary subdwarf B stars

The second sample consists of 105 sdB stars from Geier & Heber (2012), which are either single stars or in wide binaries where tidal effects become negligible. The spectral analysis in Geier & Heber (2012) showed that 71 stars are single-lined sdBs with no sign of a companion. 18 stars on the other hand have a visible spectral signature of a cool main-sequence companion. The orbital period of these systems should be long (in the order of months or years). The separation between the two stars is therefore so wide that they barely affected each other gravitationally.

For the 18 systems that show a MS-companion in the spectrum this could be confirmed by looking at the SED except for three stars: for HS 2125+1105 no statement about a possible companion could be made due to a lack of infrared photometry. EC 00042-2737 and EC 19563-7205 on the other hand have good coverage of the infrared part of the spectrum (2MASS + WISE) but nevertheless show no sign of an infrared excess or companion (see Figure 5.4). Hence the classification of these objects as a SB2 system may not be correct.

In addition to these 18 stars there were 6 stars that also show an infrared excess or yield better results when fitted with a composite spectrum although there is no sign of a companion in the spectrum according to Geier & Heber (2012). These six stars are HE 0016+0044, EC 03470-5039, HE 1519-0708, HE 1450-0957, GD 619 and PB 5333 and are likely composite binaries. The results for the composite SED fits are shown in Table 5.4. The remaining stars could be well modeled with a single SED. The results for these fits are shown in Table A.2 in the appendix.

Table 5.4.: Results for the composite SED fits in the Geier & Heber (2012) sample.

| Object | $T_{\rm eff,sd}$ [K] | $\log g_{\rm sd}$ | $T_{\rm eff,MS}$ | $\log g_{\rm MS}$ | $\frac{A_{\rm c}}{A_{\rm sd}}$ | E(B-V) | $d$ [kpc] | Qual. |
|---|---|---|---|---|---|---|---|---|
| EC 19563-7205 [no i.e.] | $24000^{+600}_{-600}$ | $4.81^{+0.36}_{-0.21}$ | – | – | – | $0.10^{+0.01}_{-0.01}$ | $0.99^{+0.29}_{-0.34}$ | 2 |
| GD 619 [new] | $34100^{+1800}_{-3300}$ | $5.19^{+0.54}_{-0.59}$ | $4700^{+700}_{-700}$ | $5.20^{+0.00}_{-3.20}$ | $6^{+2}_{-1}$ | $0.00^{+0.01}_{-0.00}$ | $1.79^{+1.88}_{-0.85}$ | 2 |
| PB 5333[new] | $36000^{+2800}_{-2100}$ | $5.98^{+0.22}_{-0.48}$ | $4400^{+200}_{-200}$ | $5.20^{+0.00}_{-0.22}$ | $26^{+2}_{-3}$ | $0.02^{+0.02}_{-0.02}$ | $0.41^{+0.20}_{-0.02}$ | 2 |
| EC 00042-2737[no i.e.] | $55000^{+0}_{-11614}$ | $4.60^{+1.61}_{-0.00}$ | – | – | – | $0.08^{+0.03}_{-0.02}$ | $3.94^{+0.05}_{-3.41}$ | 3 |
| KUV 01542-0710 | $32600^{+7800}_{-7400}$ | $4.60^{+1.61}_{-0.00}$ | $4900^{+1500}_{-1700}$ | $2.00^{+3.20}_{-0.00}$ | $7^{+6}_{-2}$ | $0.07^{+0.07}_{-0.07}$ | $7.21^{+2.12}_{-6.13}$ | 3 |
| HE 2322-0617 | $28100^{+6400}_{-6200}$ | $4.60^{+1.61}_{-0.00}$ | $5000^{+600}_{-1100}$ | $3.50^{+1.71}_{-1.50}$ | $18^{+12}_{-6}$ | $0.00^{+0.13}_{-0.00}$ | $6.37^{+1.72}_{-5.51}$ | 3 |
| PG 0258+184 | $30900^{+7400}_{-7800}$ | $4.60^{+1.61}_{-0.00}$ | $4900^{+500}_{-800}$ | $5.20^{+0.00}_{-3.20}$ | $20^{+26}_{-5}$ | $0.19^{+0.11}_{-0.19}$ | $4.69^{+2.13}_{-3.88}$ | 3 |
| HE 0016+0044[new] | $26700^{+1200}_{-2700}$ | $4.60^{+0.44}_{-0.00}$ | $3300^{+200}_{-200}$ | $4.87^{+0.34}_{-0.49}$ | $14^{+2}_{-2}$ | $0.07^{+0.02}_{-0.02}$ | $3.44^{+0.09}_{-1.34}$ | 3 |
| HE 1254-1540 | $25800^{+7200}_{-6800}$ | $4.60^{+1.61}_{-0.00}$ | $4200^{+500}_{-600}$ | $4.72^{+0.48}_{-2.73}$ | $17^{+10}_{-6}$ | $0.00^{+0.08}_{-0.00}$ | $5.31^{+1.39}_{-4.53}$ | 3 |
| HE 1038-2326 | $26300^{+5600}_{-6300}$ | $4.60^{+0.80}_{-0.01}$ | $5300^{+300}_{-300}$ | $3.00^{+2.21}_{-1.00}$ | $39^{+34}_{-18}$ | $0.00^{+0.10}_{-0.00}$ | $7.05^{+2.49}_{-3.28}$ | 3 |
| TON S 155 | $20800^{+11200}_{-5800}$ | $6.20^{+0.00}_{-1.61}$ | $5600^{+900}_{-1500}$ | $2.00^{+3.20}_{-0.00}$ | $8^{+11}_{-5}$ | $0.00^{+0.18}_{-0.00}$ | $0.86^{+1.29}_{-0.10}$ | 3 |
| HE 1221-2618 | $26700^{+13000}_{-6700}$ | $6.20^{+0.00}_{-1.61}$ | $4300^{+300}_{-300}$ | $4.78^{+0.43}_{-2.51}$ | $46^{+30}_{-17}$ | $0.13^{+0.12}_{-0.14}$ | $0.53^{+3.64}_{-0.10}$ | 3 |
| HE 1422-1851 | $27400^{+4600}_{-5400}$ | $4.60^{+1.48}_{-0.00}$ | $5600^{+300}_{-700}$ | $3.00^{+2.21}_{-1.00}$ | $25^{+14}_{-12}$ | $0.00^{+0.14}_{-0.00}$ | $9.69^{+2.25}_{-7.75}$ | 3 |
| HS 2216+1833 | $39900^{+15200}_{-10600}$ | $4.60^{+1.61}_{-0.00}$ | $4100^{+300}_{-600}$ | $5.20^{+0.00}_{-1.08}$ | $25^{+18}_{-6}$ | $0.34^{+0.06}_{-0.02}$ | $2.12^{+0.52}_{-1.82}$ | 3 |
| HE 1450-0957[new] | $34000^{+15300}_{-8400}$ | $4.60^{+0.80}_{-0.00}$ | $2900^{+400}_{-600}$ | $2.00^{+2.45}_{-0.00}$ | $25^{+31}_{-8}$ | $0.09^{+0.03}_{-0.02}$ | $5.06^{+0.78}_{-4.29}$ | 3 |
| PG 0909+164 | $31900^{+4100}_{-3600}$ | $4.66^{+0.84}_{-0.07}$ | $8800^{+3300}_{-6500}$ | $2.00^{+3.20}_{-0.00}$ | $0^{+2}_{-0}$ | $0.02^{+0.02}_{-0.02}$ | $2.59^{+0.87}_{-1.97}$ | 3 |
| HE 1352-1827 | $38600^{+16500}_{-21200}$ | $4.60^{+1.61}_{-0.00}$ | $5000^{+900}_{-1200}$ | $5.20^{+0.00}_{-3.20}$ | $57^{+71}_{-44}$ | $0.00^{+0.24}_{-0.00}$ | $11.17^{+5.49}_{-10.20}$ | 3 |
| PG 2122+157 | $15000^{+40000}_{-0}$ | $4.80^{+1.40}_{-0.21}$ | $5600^{+1000}_{-1200}$ | $2.00^{+3.20}_{-0.00}$ | $7^{+196}_{-5}$ | $0.10^{+0.22}_{-0.10}$ | $1.53^{+8.12}_{-1.29}$ | 4 |
| HE 2156-3927 | $30300^{+24700}_{-11500}$ | $6.20^{+0.00}_{-0.80}$ | $4800^{+300}_{-500}$ | $2.37^{+2.78}_{-0.38}$ | $23^{+20}_{-12}$ | $0.00^{+0.06}_{-0.00}$ | $0.64^{+4.26}_{-0.14}$ | 4 |
| EC 03470-5039[new] | $42000^{+13000}_{-22200}$ | $4.86^{+1.35}_{-0.26}$ | $4700^{+400}_{-500}$ | $5.20^{+0.00}_{-3.20}$ | $37^{+12}_{-28}$ | $0.00^{+0.10}_{-0.00}$ | $2.57^{+1.51}_{-2.24}$ | 4 |
| HE 1519-0708[new] | 37700 | 5.78 | 3600 | 4.50 | 18 | 0.01 | 0.00 | 4 |
| HE 1441-0558 | $26000^{+29100}_{-11000}$ | $4.61^{+1.59}_{-0.02}$ | $4300^{+200}_{-300}$ | $5.20^{+0.00}_{-0.64}$ | $55^{+26}_{-34}$ | $0.04^{+0.13}_{-0.05}$ | $3.44^{+2.16}_{-3.02}$ | 4 |
| HE 1419-1205 | 32400 | 5.74 | 4600 | 2 | – | 0.21 | 1.00 | 4 |
| HE 1200-0931 | 35300 | 6.06 | 6200 | 4 | – | 0.05 | 0.14 | 4 |
| HS 2125+1105[no i.e.] | $38900^{+16200}_{-12100}$ | $5.00^{+1.21}_{-0.40}$ | – | – | – | $0.10^{+0.06}_{-0.07}$ | $6.29^{+6.71}_{-5.00}$ | 5 |

[no i.e.] No infrared excess was found.

[new] Infrared excess was detected altough Geier & Heber (2012) did not find a companion in the spectrum.

## 5.4. SPY

The third sample is drawn from the ESO **S**upernova Ia **P**rogenitor Surve**y** (SPY), which is a large survey in search of double degenerate binaries meaning two white dwarfs as potential progenitors of type Ia supernovae. The survey was carried out with the UVES spectrograph at the Very Large Telescope (Napiwotzki et al., 2001; Stroeer et al., 2007). In the course of this survey high-resolution optical spectra of more than 1000 white dwarf candidates have been obtained. Among these 1000 objects about 140 misclassified white dwarfs have been found which turned out to be hot subdwarfs of various types (Lisker et al., 2005). This provides a homogeneous sample with high-quality, high-resolution spectra with large wavelength coverage for each star. In Lisker et al. (2005) a sample of 76 sdB stars has been introduced. The spectral analysis of these stars exposed that 24 show signs of a cool companion in the spectrum. This could be confirmed photometrically for all these stars except for HS 2125+1105 where no data in the infrared was available. In addition to that, 5 stars have been found which have not been known so far to contain a main-sequence companion. The parameter of the companions are listed in Table 5.5.

Table 5.5.: Binaries in the SPY sample. The results for the subdwarf component are shown in Table A.3 in the Appendix.

| Object | Lisker et al. (2005) | $T_{\rm eff}$ (comp) | $\frac{A_{\rm c}}{A_{\rm sd}}$ | E(B-V) |
|---|---|---|---|---|
| HE 1038-2326 | F7 | $5360^{+220}_{-230}$ | $51^{+19}_{-26}$ | $\leq 0.011$ |
| HE 1140-0500 | G1 | $4900^{+2400}_{-1400}$ | $9.8^{+2.4}_{-4.2}$ | $0.12^{+0.06}_{-0.12}$ |
| HE 1221-2618 | G0 | $4510 \pm 110$ | $51^{+13}_{-\ 7}$ | $0.17^{+0.05}_{-0.06}$ |
| HE 1309-1102 | G9 | 5300 | 5.5 | 0.3 |
| HE 1352-1827 | G3 | $5000^{+\ 800}_{-1100}$ | $54^{+20}_{-35}$ | $\leq 0.21$ |
| HE 1422-1851 | F9 | $5820^{+250}_{-150}$ | $40^{+\ 9}_{-16}$ | $\leq 0.09$ |
| HE 1441-0558 | G5 | $4340 \pm 70$ | $62^{+12}_{-11}$ | $0.10 \pm 0.07$ |
| HE 2156-3927 | K3 | $4740^{+240}_{-410}$ | $20.3^{+2.3}_{-7.5}$ | $\leq 0.06$ |
| HE 2322-0617 | G9 | $5000^{+\ 500}_{-1000}$ | $18^{+9}_{-6}$ | $\leq 0.12$ |
| HE 2322-4559 | G4 | $3200^{+1000}_{-\ 900}$ | $37^{+67}_{-22}$ | $\leq 0.029$ |
| HS 1536+0944 | K0 | $5240^{+150}_{-290}$ | $45^{+23}_{-\ 8}$ | $0.08 \pm 0.08$ |
| HS 2216+1833 | G1 | Photometry blended | | |
| PG 0258+184 | G8 | $5000^{+400}_{-800}$ | $23^{+24}_{-\ 7}$ | $0.15^{+0.05}_{-0.16}$ |
| PG 2122+157 | F7 | $6000^{+\ 500}_{-1000}$ | $20^{+45}_{-15}$ | $0.12^{+0.18}_{-0.11}$ |
| TON S155 | F7 | $8000^{+4000}_{-6000}$ | $28^{+121}_{-\ 28}$ | $0.108^{+0.022}_{-0.109}$ |
| HE 1200-0931 | K1 | 5200 | 7.0 | 0.28 |
| HE 1254-1540 | K7 | $4300^{+500}_{-700}$ | $21^{+8}_{-5}$ | $\leq 0.08$ |
| HE 1419-1205 | K5 | 4600 | 7.6 | 0.2 |
| KUV 01542-0710 | K2 | $5200^{+900}_{-600}$ | $7.8^{+2.3}_{-1.4}$ | $0.04 \pm 0.04$ |
| HS 2125+1105 | K4 | not enough photometric data | | |
| HE 1459-0234 | – | $5890^{+130}_{-150}$ | $70^{+70}_{-50}$ | $0.07^{+0.17}_{-0.08}$ |
| HS 1530+0542 | – | $6270^{+370}_{-230}$ | $45^{+156}_{-\ 28}$ | $0.16^{+0.07}_{-0.13}$ |
| GD 617 | – | $6550^{+210}_{-220}$ | $70 \pm 60$ | $\leq 0.01$ |
| GD 1237 | – | $4700^{+1700}_{-1300}$ | $24^{+177}_{-\ 21}$ | $0.42^{+0.09}_{-0.43}$ |
| Formerly unknown binary systems (composite) | | | | |
| HE 0016+0044 | – | $3140^{+460}_{-240}$ | $16^{+6}_{-5}$ | $0.080^{+0.032}_{-0.022}$ |
| HE 0230-4323 | – | $5000^{+400}_{-800}$ | $13.9^{+1.9}_{-4.8}$ | $\leq 0.05$ |
| HE 1450-0957 | – | $2900^{+400}_{-600}$ | $25^{+16}_{-\ 7}$ | $0.087^{+0.019}_{-0.018}$ |
| GD 619 | – | $4500^{+1200}_{-\ 900}$ | $7.0^{+2.8}_{-1.2}$ | $0.008^{+0.011}_{-0.008}$ |
| HE 1519-0708 | – | 3100 | 24 | 0.015 |

## 5.5. TGAS

A sample of 181 sdB stars in the Tycho catalog in preparation of the upcoming Gaia data release was also examined. The Gaia satellite is a space observatory aimed at the astrometric measurement of approximately 1 billion astronomical objects. It will provide very precise measurements of position, distance and apparent motion of many stars. In order to disentangle the parallax and the proper motion roughly 14 measurements of each star have been made so far. But because this is not sufficient the Gaia data will be combined with positions extracted from the Tycho-2 catalog, based on data taken between 1989 and 1993 by Gaia's predecessor, the Hipparcos satellite. That is why stars which are both in the Tycho and the Gaia catalog will be released first on September 14, 2016 and therefore are of particular interest (Michalik et al., 2015).

This leads to a very diverse sample with all kinds of hot subdwarfs. The sample contains some very hot ($T_{\rm eff} > 50000$) subdwarfs which cannot be examined with the current SED model grid, since its maximum temperature is 50000 K. Also there is a sizeable amount of helium rich subdwarfs ($z > -0.5$) which also are not covered by the grid. A list of the stars in this sample that could not be modeled can be found in Table 5.6.

Moreover there were 2 stars (PG 1051+501 and KUV 16256+4034) where the photometry was blended by nearby stars and therefore the results were discarded.

Table 5.6.: 23 Stars in TGAS sample which can't be modelled because either their helium abundance or their surface temperature is too high. The values for the effective temperature and $\log y$ are obtained by a spectroscopic analysis.

| Object | $T_{\text{eff}}$ | $\log y$ |
|---|---|---|
| FB 3 [i.e.] | 38000 | -0.2 |
| SB 705 | 45090 | 1.0 |
| JL 285 | 41000 | 2.3 |
| PG 0314+146 | 47520 | 0.9 |
| CD-31 4800 | 43000 | 2.75 |
| GALEX J07581-0432 | 41360 | 0.54 |
| UVO 0832-01 | 44000 | 2.0 |
| UVO 0904-02 | 46200 | 1.91 |
| GALEX J09529-3719 | 44230 | 0.53 |
| CD-24 9052 | 41700 | -0.35 |
| HD 113001[i.e] | 41000 | 0.5 |
| HD 127493 | 42500 | 0.62 |
| GALEX J17558+5012 | 40370 | 1.3 |
| LSIV+10 9 | 45700 | 0.78 |
| JL 87 | 25800 | 0.33 |
| GALEX J19111-1406 | 55970 | 0.25 |
| BD+37 442 | 60000 | – |
| BD-3 2179 | 62000 | 0.3 |
| CD-51 11879 | 72300 | 0.02 |
| CD-45 5058 | 75000 | 0.5 |
| LSE 153 | 70000 | – |
| LSIV-12 1 | 60000 | -0.950 |
| BD+28 4211 | 81300 | -1.120 |

[i.e.] infrared excess was detected

### 5.5.1. Feige 34

One of the stars with an effective temperature above 50000 K could be analysed with a synthetic model provided by Dr. Marilyn Latour. This stars is commonly known as Feige 34 and has an effective temperature of 63000 K and a surface ratio $\log g = 6.0$.
In the SED (Figure 5.5) the signature of a cool companion was detected. The parameters of the fit were:

| | |
|---|---|
| $T_{\mathrm{eff,sd}}$ | 63000 K (fixed) |
| $\log g_{\mathrm{sd}}$ | 6.0 dex (fixed) |
| $T_{\mathrm{eff,comp}}$ | 3300-3800 K |
| $\log g_{\mathrm{comp}}$ | 2.3-4.13 dex |
| $A_{\mathrm{c}}/A_{\mathrm{sd}}$ | 22.5-29.5 |
| $E(B-V)$ | 0-0.01 |
| distance | 247-254 pc |

The slight deviation in the ultraviolet could be a sign of a metal deficiency in the used model.

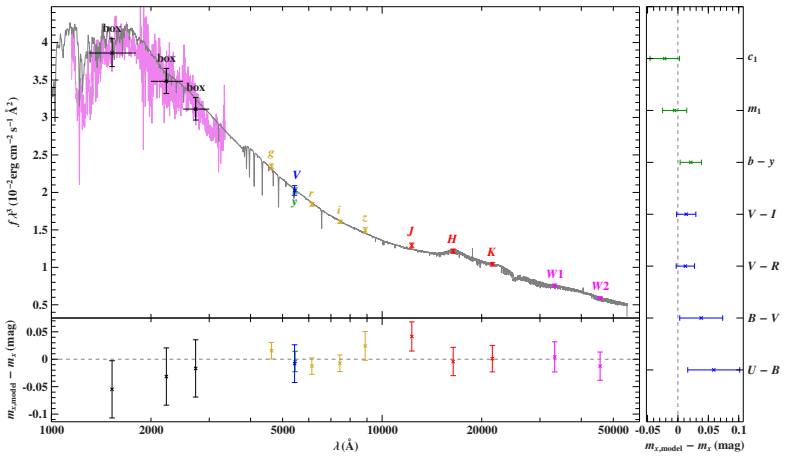


Figure 5.5.: Spectral energy distribuion of Feige 34. A cool main-sequence companion was modeled as well.

### 5.5.2. The restricted TGAS sample

101 stars in the sample could be modeled by a single SED since they show no sign of a cool companion. For all these stars both the effective temperature and the surface gravity were restricted to lie within the error margin of the spectroscopic values in order to get a well defined distance. The results can be found in the Appendix in table A.4. But there is also a quite large fraction of stars that could only be modelled with a composite SED because there was an infrared excess (54 stars). The results for these fits are shown in the Appendix (Table A.5)

## 5.6. Combined results of four surveys

In order to test the performance of the photometric analysis, the photometric results of the four sample previously discussed, were compared to spectroscopic ones (see Figure 5.6a). A color and symbol coding was used to show the different quality grades (see caption). The general trend is the worse the photometric quality the larger is the scattering of the data points. A closer examination has been carried out by fitting a linear function two the data in each grade individually (see Figure 5.7). For grade 1, where observations in almost every photometric system including the narrow band filter Hbeta are available, the deviations from a line through the origin are very low. The Root-mean-square error (RMS) is about 1000 K. For all other grades the scatter becomes large for stars hotter than 40000 K. Therefore we exclude them from the fit. This gives Root-mean-square errors of 2420 K for grade 2 and 3391 K for grade 3.

Grade 4 shows larger scattering because here observations in the UV are completely missing (there isn't even a U-Band observation). The quality 5 category though yields better results again because an U-Band observation is present. And for the worst grade (6) the effective temperature cannot be restrained at all.

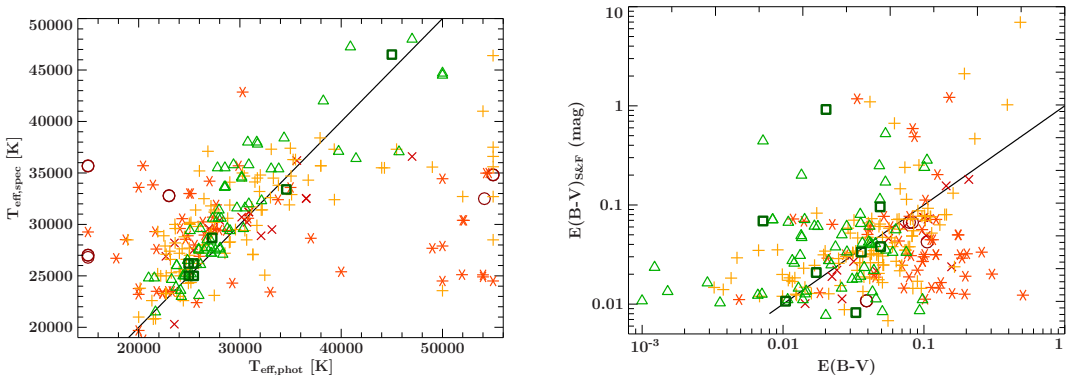


(a) effective temperature of hot subdwarfs

(b) reddening

Figure 5.6.: Comparison between results for the effective temperature from photometry and spectroscopy and for the reddening with the extinction map from Schlafly & Finkbeiner (2011). Only stars that could be modelled with a single SED where taken into consideration here. The colors and symbols encode the quality of the data: darkred circle = 6, red cross = 5, orange asterisk = 4, yellow cross = 3, green triangle = 2, darkgreen square = 1. The straight line indicates equality.

Beside the comparison with the effective temperature from spectroscopy, a comparison of the determined interstellar reddening $E(B-V)$ with values gained from the extinction maps of Schlafly & Finkbeiner (2011) was carried out (see Figure 5.6b).

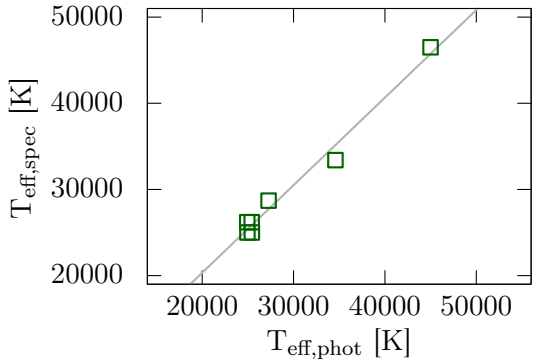


(a) Grade 1, RMS: 1029 K, m=1.01

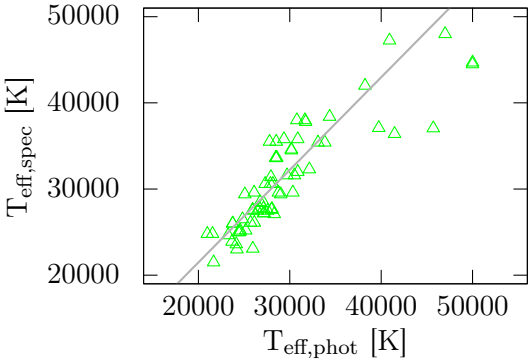


(b) Grade 2, RMS: 2420 K, m=1.07

*g*

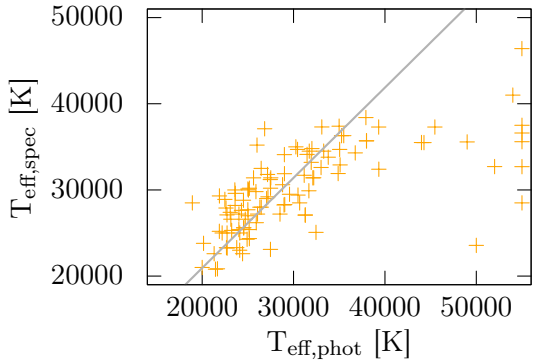


(c) Grade 3, RMS: 3391 K, m=1.05

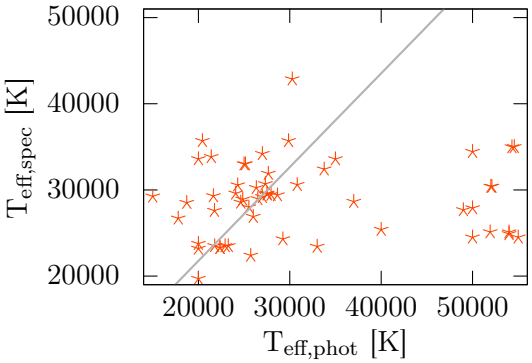


(d) Grade 4, RMS: 6394 K, m=1.09

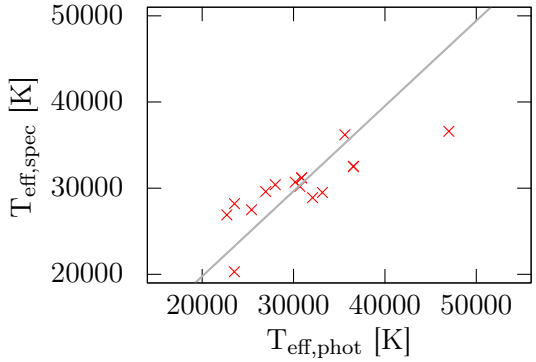


(e) Grade 5, RMS: 2955 K, m=0.99

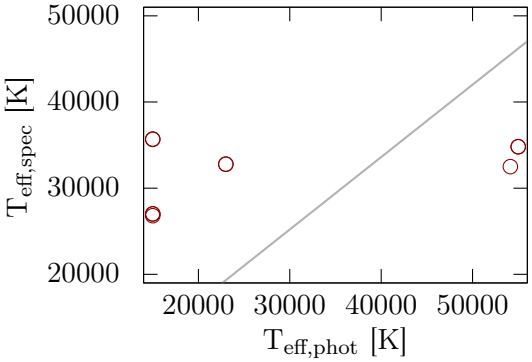


(f) Grade 6, RMS: 16575 K, m=0.84

Figure 5.7.: Comparison between results for the effective temperature from photometry and spectroscopy. A linear function ($y = m \cdot x$) was fitted to the data. The Root-mean-square error (RMS) and the slope (m) is shown in the individual captions. For grade 2-5 stars hotter than 40000 K were excluded from the fit.

# 6. Large subdwarf catalog

The last sample was a compilation of all larger subdwarf catalogues by Dr. Stephan Geier. This yields a very large and heterogeneous sample of roughly 4500 stars from various sources and with a wide range of parameters. This also means all the stars from the samples discussed in the previous section are included. The main aim of the investigation of this sample is to provide distances and reddening for kinematic analyses.

For about a third of all stars (1600) atmospheric parameters are available from spectroscopic analysis. For these stars the effective temperature and the surface gravity were restricted to be within the uncertainty of the spectroscopic values in order to get a well constrained distance and to improve potential binary fits, where the determination of the effective temperature of the hot subdwarf can become more and more difficult with increasing brightness of the companion.

The analysis of these 1600 stars reveals that roughly 20% of them shows an infrared excess. The classification into single SED fit and composite SED fit allows to compare the distribution of the atmospheric parameters of stars with no visible companion and stars which show signs of a cool main-sequence companion (see Figure 6.1 and 6.2). The distribution of the effective temperature for single SED stars peaks at around 30000 K. The composite SED stars on the other hand exhibits a small dip at this region instead stars accumulate at around 36000 K. Figure 6.2c shows that the majority of the cool companions have an effective temperature of about 5000 K and therefore most likely are G- or K-type stars.

The ratio of the surface areas, which is one of the fitting parameters in case of a composite SED, can be used to calculate the radius of the companion. The ratio of the areas can be expressed by the ratio of the stellar radii squared $A_c/A_{sd} = R_c^2/R_{sd}^2$ and the radius of the subdwarf can be calculated via $R = \frac{GM}{g}$. Note that this is only an approximation because one has to assume a canonical mass for the subdwarf and the uncertainty of the surface gravity propagates to the uncertainty of the radius. But nevertheless this can be used to get a rough estimation about the consistency of the composite fit. For the sample where the surface gravity is known from spectroscopy and therefore the uncertainties are not too big, the radius of the companion was plotted against its effective temperature (see Figure 6.3). Since most of the companion are rather cool they tend to evolve very slowly and therefore most of them should be found on the main sequence. For comparison the radius and effective temperature of typical main-sequence stars is also plotted (black line). One can see that apart from a few outliers the radius is suitable for a main-sequence star.

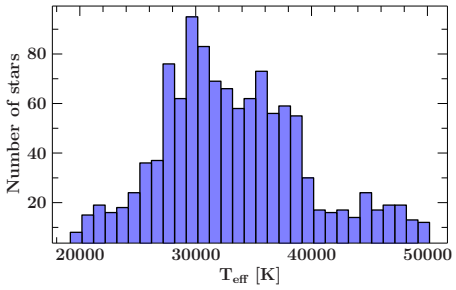


(a) effective temperature distribution (from literature)

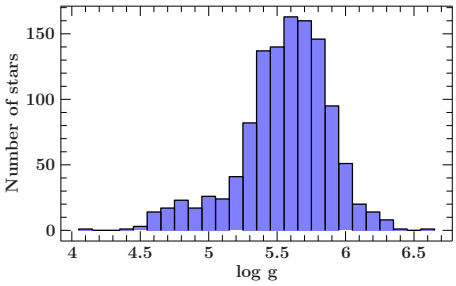


(b) surface gravity distribution (from literature)

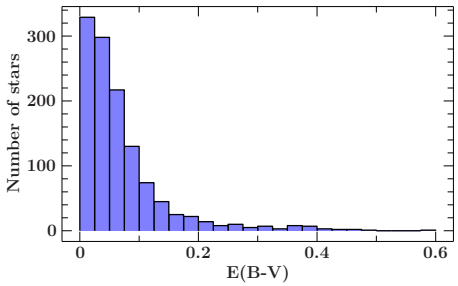


(c) reddening distribution

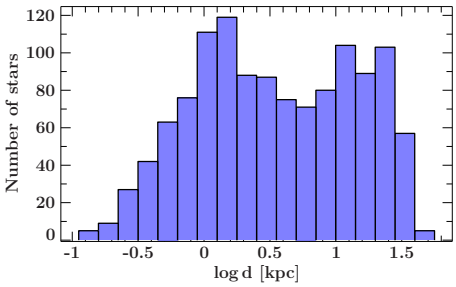


(d) distance distribution (logarithmic)

Figure 6.1.: Single SED (no infrared excess)

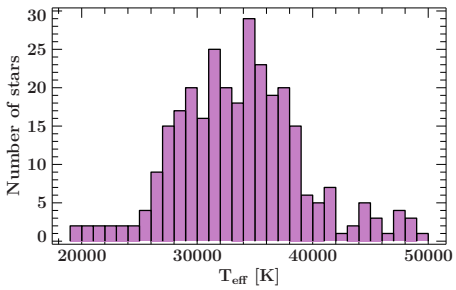


(a) $T_{eff}$ distribution for the sdB component (from literature)

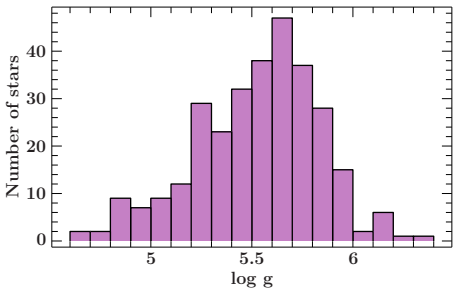


(b) surface gravity distribution for the sdB component (from literature)

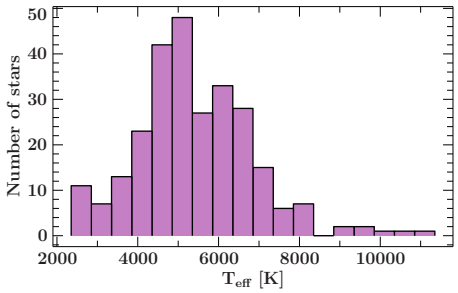


(c) effective temperature distribution (companion)

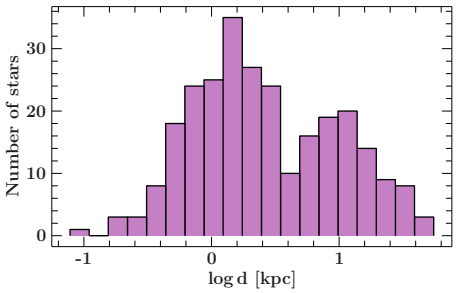


(d) distance distribution (logarithmic)

Figure 6.2.: Composite SED (infrared excess)

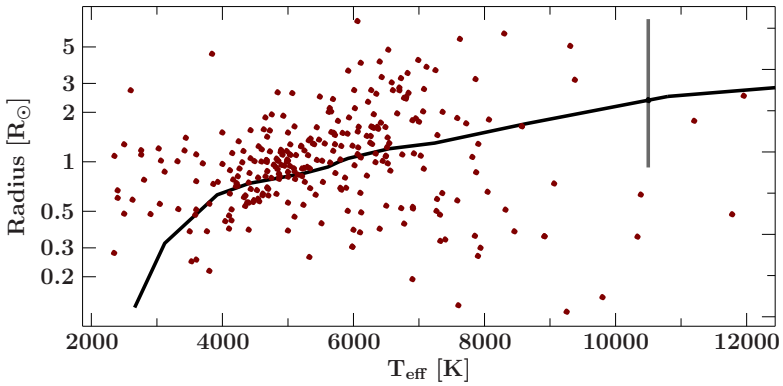


Figure 6.3.: Radius of the companion plotted against its effective temperature. The black line indicates the radius-temperature relation for a solar-metalicity main-sequence star. The mean uncertainty is plotted at $T_{\rm eff} = 10500\,{\rm K}$. Note that there is a large variance and that there are many points with lower uncertainty (this depends on the quality of the photometric data).

For the remaining 2900 stars no atmospheric parameters are accessible and must be obtained from the photometeric fitting. This is especially difficult for the surface gravity as previous discussions showed. Unfortunately the surface gravity strongly affects the determination of the distance since $d = \sqrt{\frac{4GM}{\theta^2 g}}$ and therefore $\log g$ probably is the major contributor to the uncertainty of the distance. To still be able to constrain the distance to some extend we used evolution tracks of hot subdwarfs to link the surface gravity to the effective temperature (see Fig. 6.5). Most of the stars should be found on the Extreme Horizontal Branch (EHB) where they are in the state of helium core burning. The beginning of the EHB is marked by the Zero Age EHB (ZAEHB) and the end is given by the Terminal Age EHB (TAEHB) which is the point where all the helium in the core is burned. After that the stars start to burn helium in the shell and expands slightly but this does not last for long and the subdwarf evolves towards the white dwarf cooling sequence. Figure 6.4 shows the evolution of several stars with different envelope masses in a $T_{\rm eff} - \log g$ diagram. The Extreme Horizontal Branch band is also shown in this figure indicated with two blue dashed lines. Stars on the EHB have constant luminosity $L = 4\pi R^2 \sigma T^4$ or by using $g = \frac{GM}{R^2}$ one can substitute $R$ with $g$ which gives $L = 4\pi \frac{GM}{g} T^4$. Therefore, for constant mass and luminosity the surface gravity is proportional to the fourth power of the effective temperature $g \propto T^4$. The constant of proportionality is determined by fitting a power law through the beginning of the evolution tracks for various masses which gives the ZAEHB and fitting through the point where the helium abundance in the core reaches zero which gives the TAEHB. For a given temperature the surface gravity $\log g$ then should be within these boundaries. The evolution tracks used here are taken from Dorman et al. (1993). A comparison with the 1600 stars where atmospheric parameters were already determined by spectroscopy

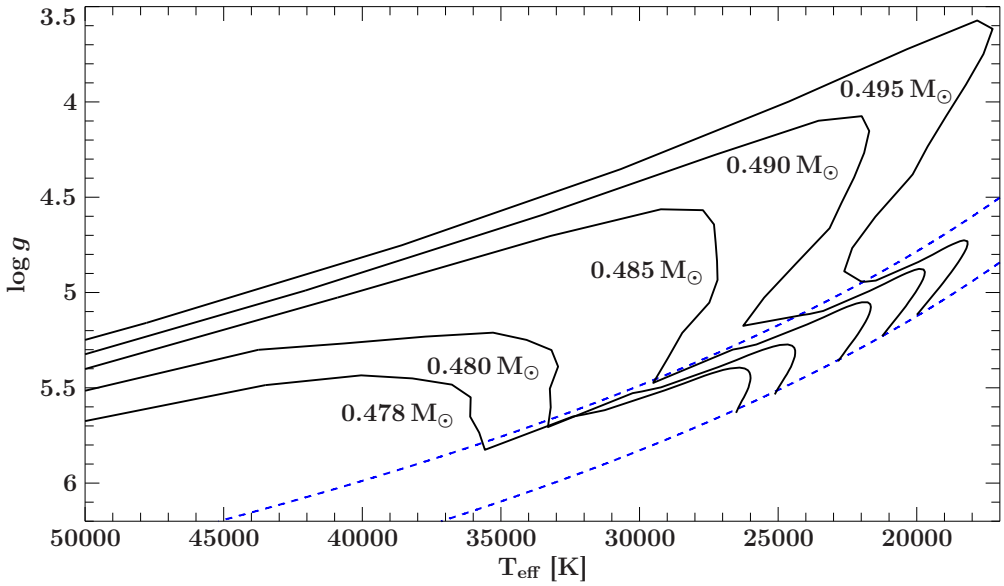


Figure 6.4.: Evolution tracks of sdB stars (black). The dashed lines in blue mark the ZAEHB and TAEHB.

(Figure 6.5) shows that a large fraction of the stars lies above the TAEHB. This indicates that the theoretical EHB is too narrow. One explanation is that the lifetime on the EHB is increased by convection and overshooting which increases the amount of helium in the core. Therefore a wider constrain (blue line) is chosen to cover the majority of stars in the plot. In addition, above 35000 K a constant relation between $\log g$ and temperature is assumed to cover the population of helium rich subdwarfs. With these constraints the uncertainty of $\log g$ should be $\pm 0.3$ dex if the temperature is well-constrained. This translates into a uncertainty of about 30% for the distance.

The analysis of the 2900 stars without atmospheric parameters from spectroscopy reveals that approximately 1600 stars show no sign of a companion and circa 1300 star exhibit an infrared excess. The distribution of the effective temperature shows a pile up of stars at both the hot end and the cool end of the grid (Figure 6.7a and 6.8a). This causes a pile up in the surface gravity as well (Figure 6.7b and 6.8b) since they are linked by the constrains discussed above. The stars where the fit converges to parameters at either the cool or the hot end of the synthetic model grid are removed from our sample because the parameters are obviously not reliable.

The distribution of the companion's effective temperature (Figure 6.8c) peaks around 5800 K which is roughly the temperature of the sun and therefore is a G-type star.

For the composite SEDs the ratio of the surface areas $A_c/A_{sd}$ was plotted against the effective temperature of the companion (Figure 6.6). With increasing temperature more and more stars show higher surface ratios as one would expect. There are also a couple of stars where the surface ratio hits the limit of 1000. These stars either have poor

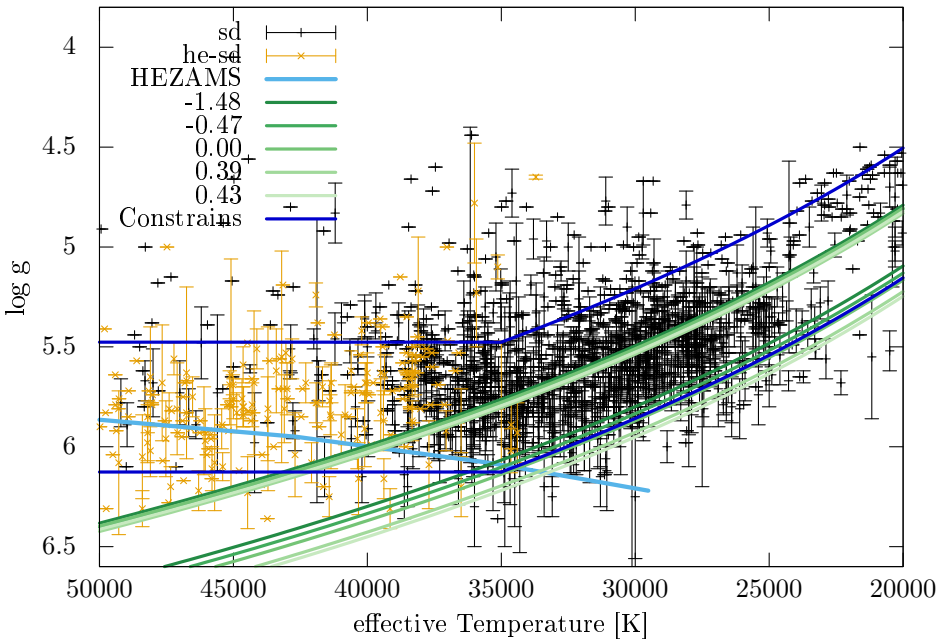


Figure 6.5.: T-log $g$ diagram of all hot subdwarfs with spectroscopic atmospheric parameters in the sample. The green lines indicate ZAEHB and TAEHB for different metalicities. As one can see the theoretical TAEHB is 0.3 dex too low. Therefore the adopted constraints for $\log g$ are given by the darkblue line.

photometric data, an already evolved and expanded companion or are simply misclassified and are rather main-sequence stars of spectral type A to F. A spectroscopic analysis of these stars is needed to obtain additional information.

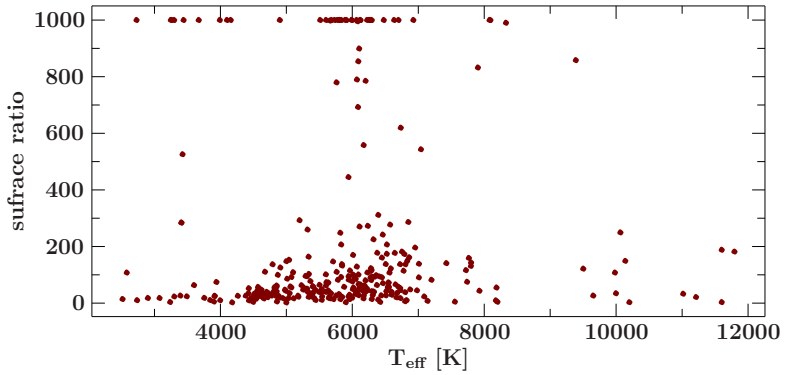


Figure 6.6.: Ratio of the surface areas of subdwarf and cool companion plotted against the surface temperature of the companion.

Looking at the various distance distributions one can see that there is a fraction of stars with a distance larger than 3 kpc. These objects are probably halo stars but for absolute certainty, a kinematic analysis with Gaia radial velocities must be carried out.

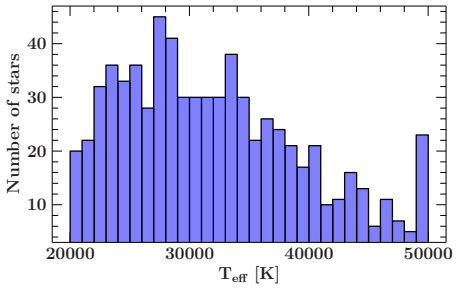


(a) effective temperature distribution

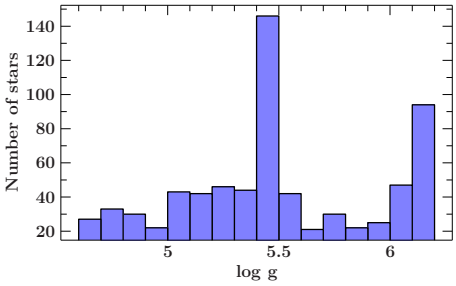


(b) surface gravity distribution

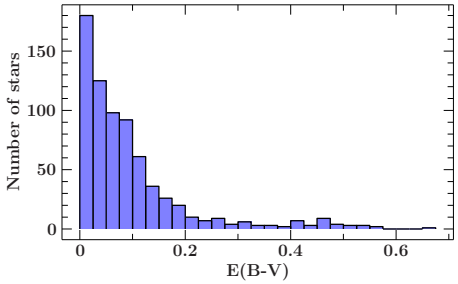


(c) reddening distribution

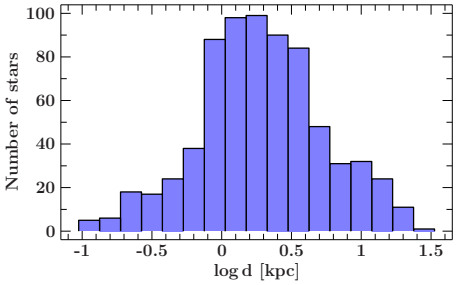


(d) distance distribution (logarithmic)

Figure 6.7.: Single SED (no infrared excess)

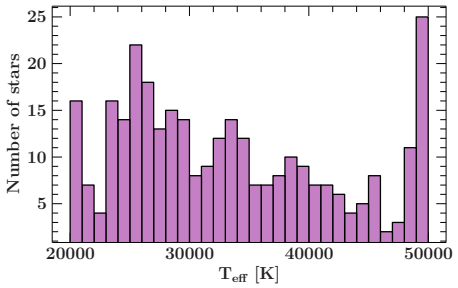


(a) effective temperature distribution (hot subdwarf)

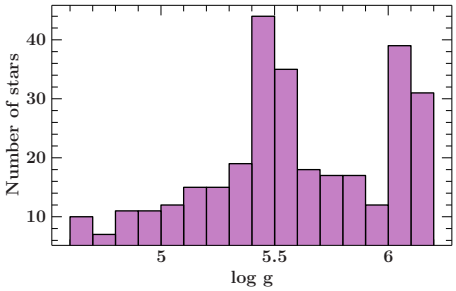


(b) surface gravity distribution (hot subdwarf)

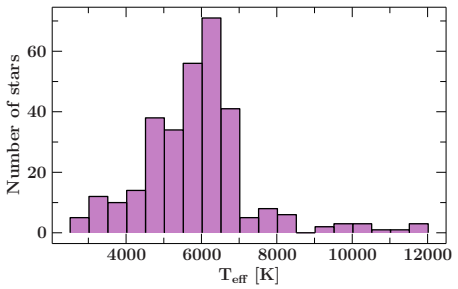


(c) effective temperature distribution (companion)

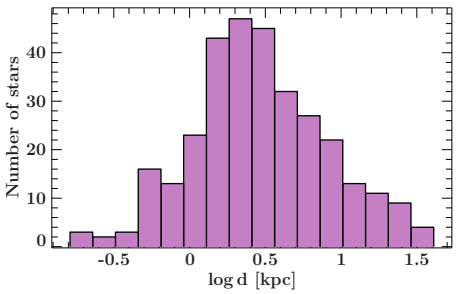


(d) distance distribution (logarithmic)

Figure 6.8.: Composite SED (infrared excess)

## 6.1. Multi-colour optical photometry BATC

Within the large sample of subdwarfs 8 stars lie within one of the observed patches of the sky of the BATC survey (see section 4.1.1). These stars therefore have very good optical coverage because the BATC survey consists of 15 intermediate-band filters evenly distributed over the visual range including the U-band. To check for consistency and to further improve the fit all observations from the other photometric systems were added as well.

Table 6.1.: Atmospheric parameters of the primary

| Object | V | $T_{phot}/T_{spec}$ | $\log g$ | E(B-V) | d [kpc] | z | Qual. |
|---|---|---|---|---|---|---|---|
| PG 2223+171 [i.e.] | 14.73 | $38100^{+4700}_{-2800}$<br>37890±1300 | $5.83^{+0.34}_{-0.38}$<br>5.67±0.13 | $0.02^{+0.04}_{-0.03}$ | $1.26^{+0.74}_{-0.42}$ | $-0.50^{+1.28}_{-0.50}$ | 3+ |
| PG 0132+151 | 15.25 | $20000^{+190}_{-0}$<br>– | $5.13^{+0.09}_{-0.17}$<br>– | $0.12^{+0.01}_{-0.01}$ | $1.55^{+0.30}_{-0.14}$ | $-1.00^{+0.26}_{-0.00}$ | 3+ |
| HS 1753+7025 [i.e.] | 15.37 | $50000^{+0}_{-29878}$<br>– | $5.60^{+0.58}_{-0.11}$<br>– | $0.08^{+0.14}_{-0.09}$ | $3.37^{+0.79}_{-2.58}$ | $-1.00^{+2.00}_{-0.00}$ | 3+ |
| SDSSJ 123137.55+074 | 17.21 [g] | $25500^{+600}_{-200}$<br>26760 | $4.94^{+0.26}_{-0.15}$<br>5.06 | $0.04^{+0.02}_{-0.02}$ | $7.49^{+1.00}_{-1.87}$ | $-1.00^{+2.00}_{-0.00}$ | 3+ |
| SDSSJ 215648.71+003 | 17.68[g] | $28300^{+1400}_{-1000}$<br>30800±800 | $5.10^{+0.73}_{-0.22}$<br>5.77±0.12 | $0.03^{+0.01}_{-0.02}$ | $8.57^{+0.48}_{-4.77}$ | $-1.00^{+1.91}_{-0.00}$ | 3+ |
| SDSSJ 214307.36+005 | 18.78[g] | $50000^{+0}_{-8126}$<br>39270 | $6.12^{+0.06}_{-0.70}$<br>5.53 | $0.23^{+0.02}_{-0.03}$ | $5.16^{+6.47}_{-0.51}$ | $+1.00^{+0.00}_{-2.00}$ | 3+ |
| SDSSJ 121856.75+465 | 19.07[g] | $48400^{+1700}_{-2200}$<br>– | $5.47^{+0.70}_{-0.05}$<br>– | $0.07^{+0.02}_{-0.03}$ | $15.79^{+1.08}_{-6.35}$ | $-1.00^{+0.53}_{-0.00}$ | 4+ |
| SDSSJ 223740.40+134 | 19.28[g] | $26500^{+3100}_{-4900}$<br>– | $4.99^{+0.78}_{-0.36}$<br>– | $0.06^{+0.03}_{-0.04}$ | $17.87^{+2.14}_{-0.01}$ | $-1.00^{+2.00}_{-0.00}$ | 4+ |

Table 6.2.: Atmospheric parameters of the companion

| Object | $T_{eff}$ | $\log g$ | sur-ratio |
|---|---|---|---|
| PG 2223+171 | $4900 \pm 100$ | $5.20^{+0.00}_{-3.20}$ | $47^{+2}_{-5}$ |
| HS 1753+7025 | $7200^{+500}_{-400}$ | $5.20^{+0.00}_{-1.20}$ | $63^{+114}_{-37}$ |

[i.e.] infrared excess was detected

[g] SDSS g was used instead of Johnson $V$

Table 6.1 shows the results for the SED fitting with BATC data. As one can see the results are in very good agreement with the spectroscopic values. Figure 6.9 shows the spectral energy distribution for each of the 8 stars with BATC data. PG 2223+171 and HS 1753+7025 both clearly show an infrared excess. The results for the composite SED fitting are shown in Table 6.2. The companion of PG 2223+171 seems to be a K-type star with a temperature of roughly 4900 K and the companion to HS 1753+7025 should be a F-type star with a temperature of about 7200 K.

As one can see the large number of passbands evenly distributed over the optical range remarkably increases the accuracy. With the third data release (DR3), Gaia will provide

similar data. There are two Photometers, a blue and a red one, which obtain low-resolution spectro-photometry. The two photometer have a resolution between 30 and 270 Å/pixel and cover the wavelengths from 3300 Å to 10500 Å. This means there should be approximately 70 passbands including about 10 bluewards of the balmer jump. This should give very accurate SEDs for a lot of stars and hence be a good tool to determine their effective temperature and interstellar reddening.

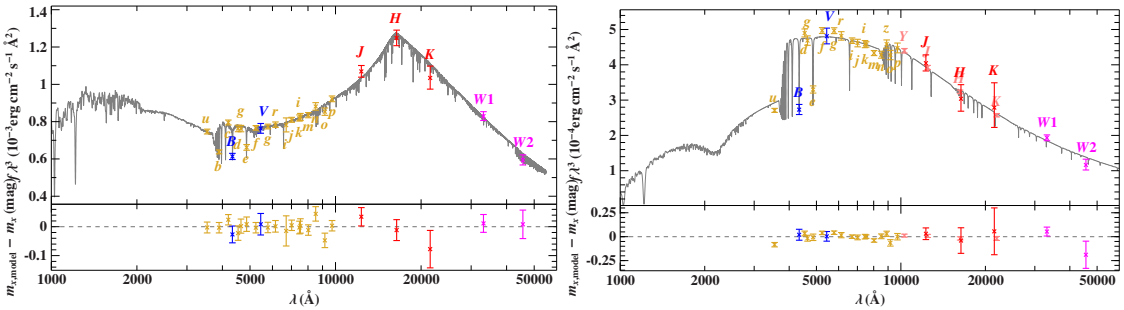

(a) PG 2223+171



(b) PG 0132+151

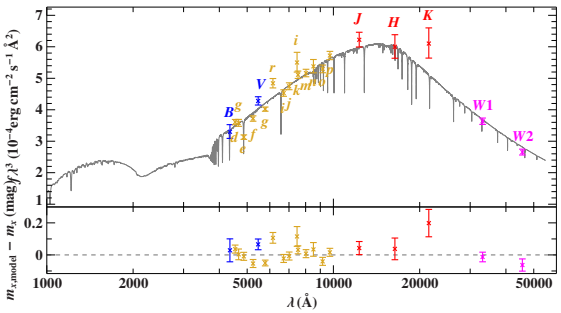

(c) HS 1753+7025

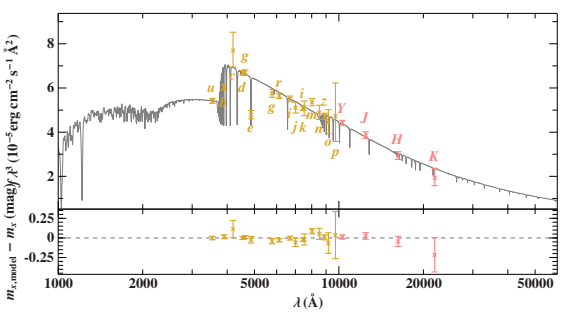

(d) SDSSJ 123137.55+074621.7

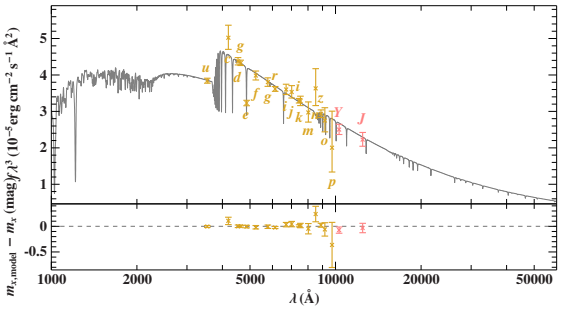

(e) SDSSJ 215648.71+003620.7

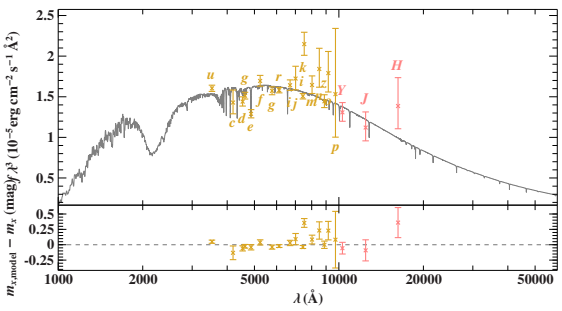

(f) SDSSJ 214307.36+005123.6

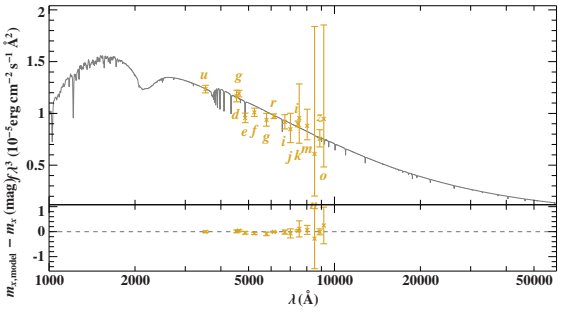

(g) SDSSJ 121856.75+465111.1

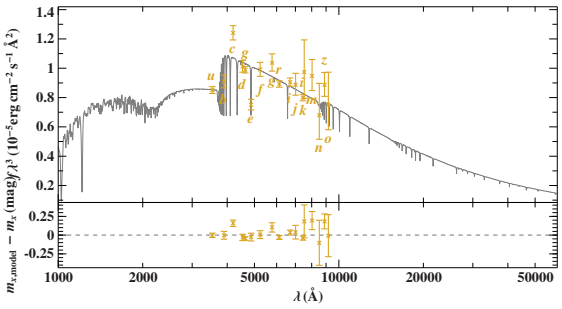

(h) SDSSJ 223740.40+134850.4

Figure 6.9.: SEDs for stars with BATC photometry

# 7. Conclusion

The stellar parameters and distances are the most fundamental parameters of the stars. The most reliable atmospheric parameters can be obtained by quantitative spectral analyses using sophisticated model atmospheres. Generally this has to be done for each star individually and hence is very time consuming. Spectroscopy can also be quite costly since large telescope are needed for high-quality spectra of faint objects.

Using photometry can be an alternative because modelling the spectral energy distribution of a star with the aid of photometric observations over a broad spectral range also allows to determine the fundamental stellar parameters. This gives an excellent tool to analyse larger samples of stars. Atmospheric parameters like the effective temperature and the surface gravity can be determined as well as interstellar reddening. Also the distance can be given derived if a mass estimate is available. In the case of sdB stars the canonical mass of $0.47\,M_{\odot}$ can be adopted.

For hot stars like sdBs and sdOs the observation in ultraviolet light is very important because they emit most of their flux in that region. It also allows to sample the Balmer discontinuity which is very sensitive to changes in effective temperature but also slightly to surface gravity. Therefore a good observational coverage of the Balmer jump highly increases the accuracy of the determination of the atmospheric parameters. The effects of interstellar reddening are also most dominant in the ultraviolet and properties like the extinction bump at 2175 Å are only observable in the UV. In addition differences in metalicity can only be detected in the ultraviolet since there the number of absorption lines of metals is quite high and therefore the opacity in the ultraviolet increases with the number of metal atoms as more and more light can be absorbed. The metalicity effect in other spectral regions like the visible or infrared is negligible. Unfortunately photometric measurements in the ultraviolet always face the problem that the extinction of earth's atmosphere and in particular the absorption of light by the ozone layer rapidly increases in the UV. This makes ground based observations in the ultraviolet very difficult to impossible. The U-Band as it is realized in photometric systems like the Johnson, Strömgren or Geneva is one of the few ground-based photometric passbands that slightly probes the longer wavelengths of the UV. It is sufficient to sample the Balmer jump but does not cover the interstellar extinction bump or helps when trying to determine the metalicity. Also observations in the U-Band are less frequent and bear larger uncertainties because they involve difficult corrections of the atmospheric extinction. Therefore observations from space are necessary where atmospheric extinction by the earth does not play a role. The GALEX mission performed photometric measurements for a large number of point sources but unfortunately the observations of the GALEX satellite are not at the level of accuracy required. Instead spectra obtained during the IUE missions

are taken and converted into photometric observations using special purpose box filter. In this way the spectral range from 1300-3000 Å is covered for those stars where IUE spectra are obtainable and metalicity and interstellar reddening can be determined.

Although the metalicity could not be determined for most stars because observations in the ultraviolet were missing, we left the metalicity $z$ as a free parameter because it influences the determination of the distance. A larger value of $z$ means more overall absorption leading to a larger distance because the object appears dimmer. Therefore the uncertainty of the metalicity increases the uncertainty of the distance. er der Zweitgutachterin gegengezeichnet werden kann . Sollten beide There was also a significant fraction of stars that showed an infrared excess in the spectral energy distribution. This is most likely a sign of a cool companion. We could model these systems with a composite SED, a combination of the SED of a hot subdwarf and the SED of a cool main-sequence star.

For the SED of the hot subdwarfs a synthetic model grid was calculated using the ATLAS12 code (Kurucz, 1996). The grid covers an effective temperature range from 20000 K to 50000 K and surfaces gravities $\log g$ from 4.6 to 6.2. The wavelength coverage of each SED is from 300 Å to 100000 Å (far UV to far infrared). This wavelength range is sampled by 27720 data points. The metalicity of the synthetic models can vary between a tenth and ten times the typical chemical composition of a hot subdwarf.

For the main-sequence companion a synthetic model grid was downloaded from the Göttingen Spectral Library (`http://phoenix.astro.physik.uni-goettingen.de/`). These models were calculated using the stellar atmosphere code PHOENIX (Husser et al., 2013). The temperature of this grid ranges from 12000 K to 2300 K and the surfaces gravity from 2 to 5. The metalicity is fixed to solar. The wavelengths from 500 Å to 55000 Å are covered. This wavelength range is sampled by 47006 data points.

But this increases the number of free parameters and introduces degeneracy among them because not only the atmospheric parameters of the hot subdwarf ($T_{\rm eff}$, $\log g$), the interstellar reddening E(B-V) and the distance have to be determined but also the atmospheric parameters of the companion and the ratio of the surface of the two components. This makes it difficult for the minimization algorithm to find the best fit. Most of the time the best fit is only found in the confidence level computation where a large fraction the parameter space is sampled. Nevertheless stars that showed an infrared excess could be modelled quite well with a composite SED and the results for the companion are convincing.

In this work 5 different samples of hot subdwarf stars from various sources and of different nature were analysed.

The first sample consisted of 142 short period binary systems containing a hot subdwarf compiled by Kupfer et al. (2015). In order to clarify the nature of the companion and to check the already known systems for consistency the spectral energy distribution for all systems has been constructed. For systems with a white dwarf companion it should be possible to model them with a single SED with hot subdwarf characteristics. Systems with a cool main-sequence companion should show an infrared excess and therefore should be modeled by a composite spectrum of a subdwarf and a MS-star. For 42 of these stars the companion could be identified as cool-main sequence companion. Amongst them are

26 stars which are known for showing a time-variable reflection effect and are therefore omitted in this work. For the remaining subdwarfs the nature of the companion could be limited to a very cool star, a white dwarf or an substellar object.

The second sample consists of 105 subdwards discussed in Geier & Heber (2012) which show no periodic variability in the radial velocity curve. The existence of a cool companion could be confirmed for the 18 systems where the signature of a companion was already visible in the optical spectrum. In addition six new systems with cool MS companions were found. Since all these systems show no radial velocity variability the orbits must be wide so they don't interact gravitationally. The remaining stars of the sample could be modelled with a single SED properly.

Sample 3 consists of 76 sdB stars found in the SPY survey by Lisker et al. (2005). The photometric analysis showed that 29 stars probably revolve around a common center-of-mass with a cool main-sequence companion. The remaining stars showed no infrared excess and were modelled with a single hot subdwarf SED.

The fourth sample prepared for the first Gaia data release and consists of 181 stars. Due to limitations in the model grid only a fraction of this heterogeneous sample could be investigated. 23 stars had to be dismissed because either their temperature or their helium abundance was too high. 54 stars showed an infrared excess and where modelled with a composite SED whereas 104 stars showed no sign of a companion and could be modelled with a single SED.

After the investigation of the large sample compiled by Dr. Stephan Geier we could conclude that more than 30% of all hot subdwarfs show signs of a cool main-sequence companion in the spectral energy distribution. Furthermore the interstellar reddening and the distance of approximately 4500 hot subdwarfs was determined. Among them is a large fraction of stars with distances larger than 3 kpc. These objects are most likely halo stars, but only a kinematic analysis with Gaia's radial velocities will give absolute certainty.

# A. Appendix

Table A.1.: Results for the single SED fits in the Kupfer sample (see section 5.2)

| Object | $T_{\rm eff}$ [K] | $\log g$ | z | E(B-V) | $\theta$ | Quality |
|---|---|---|---|---|---|---|
| PG 1619+522 | $32100^{+1900}_{-1700}$ | $5.73^{+0.48}_{-0.93}$ | $0.12^{+0.29}_{-0.54}$ | $0.03^{+0.02}_{-0.02}$ | $12.34^{+0.49}_{-0.50}$ | 2 |
| Feige 108 | $30200^{+1100}_{-1000}$ | $5.56^{+0.40}_{-0.46}$ | $0.30^{+0.18}_{-0.18}$ | $0.05^{+0.01}_{-0.01}$ | $15.14^{+0.34}_{-0.36}$ | 2 |
| PG 1032+406 | $29700^{+700}_{-500}$ | $5.79^{+0.41}_{-0.51}$ | $-0.07^{+0.21}_{-0.43}$ | $0.00^{+0.01}_{-0.00}$ | $29.25^{+0.53}_{-0.61}$ | 2 |
| CD-24 731 | $33100^{+1900}_{-1000}$ | $6.20^{+0.00}_{-0.41}$ | $0.04^{+0.24}_{-0.64}$ | $0.01^{+0.01}_{-0.01}$ | $23.51^{+0.83}_{-0.87}$ | 2 |
| PG 0839+399 | $31700^{+2300}_{-1800}$ | $5.96^{+0.25}_{-1.36}$ | $0.21^{+0.29}_{-0.90}$ | $0.01^{+0.02}_{-0.02}$ | $7.57^{+0.36}_{-0.36}$ | 2 |
| TON S135 | $24400^{+700}_{-500}$ | $5.22^{+0.26}_{-0.32}$ | $-0.37^{+0.29}_{-0.27}$ | $0.00^{+0.01}_{-0.01}$ | $15.39^{+0.23}_{-0.26}$ | 2 |
| PG 0934+186 | $30900^{+4000}_{-2900}$ | $5.82^{+0.38}_{-0.87}$ | $-0.47^{+0.79}_{-0.53}$ | $0.02^{+0.03}_{-0.03}$ | $13.76^{+1.23}_{-1.32}$ | 2 |
| PG 0958-073 | $26100^{+600}_{-600}$ | $5.27^{+0.50}_{-0.67}$ | $-0.23^{+0.32}_{-0.47}$ | $0.04^{+0.01}_{-0.01}$ | $13.48^{+0.23}_{-0.20}$ | 2 |
| TON 245 | $25200^{+900}_{-900}$ | $5.93^{+0.27}_{-0.60}$ | $0.43^{+0.22}_{-0.23}$ | $0.04^{+0.01}_{-0.02}$ | $12.07^{+0.26}_{-0.26}$ | 2 |
| PG 1300+279 | $30300^{+1500}_{-1300}$ | $5.94^{+0.26}_{-0.64}$ | $0.34^{+0.23}_{-0.23}$ | $0.02^{+0.02}_{-0.02}$ | $8.08^{+0.27}_{-0.29}$ | 2 |
| HD 171858 | $27100^{+800}_{-900}$ | $5.59^{+0.25}_{-0.28}$ | $-1.00^{+0.24}_{-0.00}$ | $0.05^{+0.01}_{-0.01}$ | $75.40^{+1.50}_{-1.36}$ | 2 |
| [CW83] 1735+22 | $31700^{+3300}_{-2000}$ | $5.27^{+0.77}_{-0.63}$ | $-1.00^{+0.37}_{-0.00}$ | $0.01^{+0.02}_{-0.02}$ | $24.06^{+1.38}_{-1.79}$ | 2 |
| PG 1000+408 | $41500^{+10300}_{-3500}$ | $4.80^{+0.97}_{-0.20}$ | $-0.31^{+0.78}_{-0.69}$ | $0.00^{+0.03}_{-0.01}$ | $9.54^{+0.61}_{-1.15}$ | 2 |
| PG 1452+198 | $29000^{+1800}_{-2000}$ | $6.20^{+0.00}_{-1.20}$ | $0.07^{+0.25}_{-0.75}$ | $0.04^{+0.02}_{-0.03}$ | $20.08^{+0.99}_{-0.85}$ | 2 |
| PG 1230+052 | $28300^{+1600}_{-1300}$ | $5.80^{+0.40}_{-0.66}$ | $0.28^{+0.29}_{-0.27}$ | $0.03^{+0.02}_{-0.02}$ | $13.92^{+0.53}_{-0.60}$ | 2 |
| TON S183 | $25900^{+500}_{-300}$ | $5.62^{+0.17}_{-0.19}$ | $-0.13^{+0.18}_{-0.25}$ | $0.00^{+0.01}_{-0.00}$ | $19.68^{+0.19}_{-0.23}$ | 2 |
| KPD 2215+5037 | $28800^{+4200}_{-3100}$ | $5.41^{+0.80}_{-0.81}$ | $0.42^{+0.59}_{-0.75}$ | $0.11^{+0.04}_{-0.04}$ | $12.16^{+1.31}_{-1.38}$ | 2 |
| PG 1648+536 | $27900^{+5100}_{-3200}$ | $5.27^{+0.93}_{-0.68}$ | $-1.00^{+0.85}_{-0.00}$ | $0.06^{+0.05}_{-0.04}$ | $10.55^{+0.81}_{-1.22}$ | 2 |
| PG 0101+039 | $27600^{+1300}_{-1200}$ | $5.65^{+0.49}_{-0.68}$ | $-0.43^{+0.54}_{-0.57}$ | $0.04^{+0.02}_{-0.02}$ | $25.30^{+0.77}_{-0.79}$ | 2 |
| PG 1519+640 | $28100^{+3900}_{-2000}$ | $5.88^{+0.32}_{-0.66}$ | $-0.78^{+0.93}_{-0.23}$ | $0.01^{+0.03}_{-0.02}$ | $20.68^{+1.16}_{-2.27}$ | 2 |
| PG 1743+477 | $28000^{+1400}_{-1400}$ | $5.91^{+0.29}_{-0.98}$ | $-0.07^{+0.27}_{-0.67}$ | $0.04^{+0.02}_{-0.02}$ | $11.48^{+0.43}_{-0.42}$ | 2 |
| [CW83] 1419-09 | $49200^{+5800}_{-10300}$ | $6.19^{+0.02}_{-1.45}$ | $-1.00^{+0.76}_{-0.00}$ | $0.05^{+0.02}_{-0.02}$ | $16.34^{+2.23}_{-1.15}$ | 2 |
| PG 0919+273 | $35100^{+2800}_{-2800}$ | $6.11^{+0.09}_{-0.35}$ | $-1.00^{+1.18}_{-0.00}$ | $0.01^{+0.01}_{-0.01}$ | $15.26^{+0.73}_{-0.78}$ | 3 |
| CS 1246 | $55000^{+0}_{-19218}$ | $4.60^{+1.61}_{-0.00}$ | $1.00^{+0.00}_{-2.00}$ | $0.48^{+0.04}_{-0.04}$ | $9.55^{+2.43}_{-0.21}$ | 3 |
| PG 1110+294 | $25000^{+3800}_{-1700}$ | $5.11^{+1.01}_{-0.51}$ | $1.00^{+0.00}_{-1.80}$ | $0.02^{+0.02}_{-0.02}$ | $9.81^{+0.34}_{-0.34}$ | 3 |
| PHL 861 | $25100^{+3800}_{-800}$ | $5.47^{+0.74}_{-0.87}$ | $1.00^{+0.00}_{-2.00}$ | $0.01^{+0.02}_{-0.02}$ | $6.90^{+0.25}_{-0.25}$ | 3 |
| HE 1448-0510 | $30400^{+1000}_{-1700}$ | $6.20^{+0.00}_{-0.45}$ | $1.00^{+0.00}_{-0.84}$ | $0.06^{+0.02}_{-0.02}$ | $6.94^{+0.27}_{-0.26}$ | 3 |
| PG 0907+123 | $25900^{+2900}_{-3700}$ | $5.19^{+0.72}_{-0.59}$ | $-0.00^{+1.01}_{-1.00}$ | $0.01^{+0.02}_{-0.02}$ | $10.79^{+0.62}_{-0.65}$ | 3 |
| PG 1244+113 | $35300^{+1400}_{-5400}$ | $6.20^{+0.00}_{-0.56}$ | $-0.00^{+1.01}_{-1.00}$ | $0.03^{+0.02}_{-0.02}$ | $7.64^{+0.52}_{-0.40}$ | 3 |
| PB 7352 | $24100^{+1800}_{-1700}$ | $4.60^{+0.29}_{-0.00}$ | $0.17^{+0.64}_{-1.17}$ | $0.03^{+0.01}_{-0.01}$ | $24.69^{+0.44}_{-0.42}$ | 3 |
| KPD 0025+5402 | $23600^{+2300}_{-3100}$ | $4.60^{+0.77}_{-0.00}$ | $-1.00^{+2.00}_{-0.00}$ | $0.09^{+0.03}_{-0.03}$ | $13.94^{+0.66}_{-0.72}$ | 3 |
| V1093 Her | $23100^{+2500}_{-900}$ | $4.60^{+1.05}_{-0.00}$ | $1.00^{+0.00}_{-0.48}$ | $0.01^{+0.02}_{-0.02}$ | $10.95^{+0.29}_{-0.40}$ | 3 |
| KPD 2040+3955 | $22600^{+3700}_{-1800}$ | $4.60^{+0.95}_{-0.00}$ | $0.52^{+0.49}_{-1.52}$ | $0.19^{+0.02}_{-0.02}$ | $12.09^{+0.36}_{-0.41}$ | 3 |
| PG 1512+244 | $31700^{+4100}_{-6200}$ | $5.72^{+0.48}_{-1.13}$ | $-1.00^{+2.00}_{-0.00}$ | $0.06^{+0.03}_{-0.04}$ | $13.84^{+1.23}_{-1.16}$ | 3 |
| PG 0133+114 | $23600^{+1200}_{-900}$ | $5.30^{+0.52}_{-0.70}$ | $1.00^{+0.00}_{-0.53}$ | $0.05^{+0.01}_{-0.02}$ | $24.58^{+0.44}_{-0.43}$ | 3 |
| HE 1047-0436 | $27500^{+3800}_{-1800}$ | $6.20^{+0.00}_{-1.26}$ | $1.00^{+0.00}_{-2.00}$ | $0.06^{+0.03}_{-0.02}$ | $6.32^{+0.30}_{-0.38}$ | 3 |
| PG 2331+038 | $26100^{+1800}_{-1400}$ | $4.81^{+0.49}_{-0.22}$ | $-0.00^{+0.39}_{-1.00}$ | $0.10^{+0.01}_{-0.01}$ | $7.59^{+0.13}_{-0.14}$ | 3 |
| HS 2359+1942 | $25600^{+6100}_{-1300}$ | $4.60^{+1.45}_{-0.00}$ | $1.00^{+0.00}_{-2.00}$ | $0.04^{+0.03}_{-0.02}$ | $4.81^{+0.17}_{-0.29}$ | 3 |
| HE 2135-3749 | $23600^{+5500}_{-1000}$ | $4.60^{+1.48}_{-0.00}$ | $0.93^{+0.07}_{-1.94}$ | $0.00^{+0.02}_{-0.01}$ | $10.65^{+0.31}_{-0.59}$ | 3 |
| PG 0918+029 | $31200^{+1500}_{-4100}$ | $6.20^{+0.00}_{-0.90}$ | $-1.00^{+2.00}_{-0.00}$ | $0.01^{+0.02}_{-0.01}$ | $12.41^{+0.49}_{-0.46}$ | 3 |

| | | | | | | |
|---|---|---|---|---|---|---|
| PG 1116+301 | $26500^{+4800}_{-1300}$ | $4.60^{+1.12}_{-0.00}$ | $0.69^{+0.31}_{-1.70}$ | $0.02^{+0.02}_{-0.02}$ | $8.33^{+0.19}_{-0.35}$ | 3 |
| PG 1248+164 | $24700^{+4700}_{-1300}$ | $4.60^{+1.61}_{-0.00}$ | $1.00^{+0.00}_{-1.84}$ | $0.05^{+0.03}_{-0.02}$ | $8.51^{+0.28}_{-0.48}$ | 3 |
| PG 1725+252 | $22500^{+2000}_{-500}$ | $5.09^{+0.57}_{-0.49}$ | $1.00^{+0.00}_{-0.99}$ | $0.03^{+0.01}_{-0.02}$ | $18.20^{+0.36}_{-0.28}$ | 3 |
| HE 1059-2735 | $54000^{+1100}_{-20300}$ | $4.80^{+1.40}_{-0.21}$ | $1.00^{+0.00}_{-2.00}$ | $0.11^{+0.03}_{-0.03}$ | $3.38^{+0.97}_{-0.08}$ | 3 |
| PG 0001+275 | $25100^{+3200}_{-3000}$ | $4.60^{+1.03}_{-0.00}$ | $-1.00^{+1.38}_{-0.00}$ | $0.04^{+0.04}_{-0.04}$ | $15.80^{+0.98}_{-1.19}$ | 3 |
| HE 1318-2111 | $35500^{+3100}_{-1900}$ | $4.60^{+0.73}_{-0.00}$ | $-1.00^{+0.64}_{-0.00}$ | $0.11^{+0.02}_{-0.01}$ | $6.53^{+0.26}_{-0.31}$ | 3 |
| KUV 16256+4034 | $27500^{+2200}_{-4100}$ | $4.60^{+1.61}_{-0.00}$ | $-1.00^{+2.00}_{-0.00}$ | $0.06^{+0.02}_{-0.02}$ | $20.74^{+0.64}_{-0.84}$ | 3 |
| GALEXJ234947.7+384440 | $20100^{+1000}_{-1800}$ | $4.60^{+1.11}_{-0.00}$ | $-1.00^{+1.81}_{-0.00}$ | $0.07^{+0.02}_{-0.02}$ | $41.89^{+0.63}_{-0.87}$ | 3 |
| Feige 48 | $29600^{+2000}_{-3500}$ | $4.79^{+1.42}_{-0.19}$ | $-0.79^{+1.56}_{-0.22}$ | $0.04^{+0.02}_{-0.02}$ | $12.67^{+0.44}_{-0.44}$ | 3 |
| PG 1528+104 | $24000^{+4200}_{-3600}$ | $4.60^{+0.91}_{-0.00}$ | $-1.00^{+1.61}_{-0.00}$ | $0.03^{+0.04}_{-0.03}$ | $14.39^{+1.00}_{-1.43}$ | 3 |
| PG 0941+280 | $30500^{+18100}_{-6700}$ | $4.60^{+1.61}_{-0.00}$ | $-1.00^{+2.00}_{-0.00}$ | $0.05^{+0.05}_{-0.05}$ | $13.46^{+1.64}_{-3.39}$ | 3 |
| KPD 1930+2752 | $26000^{+13800}_{-3000}$ | $4.60^{+1.61}_{-0.00}$ | $0.93^{+0.08}_{-1.93}$ | $0.23^{+0.04}_{-0.03}$ | $13.87^{+1.32}_{-2.62}$ | 3 |
| KPD 0422+5421 | $22200^{+2900}_{-1200}$ | $6.20^{+0.00}_{-0.49}$ | $1.00^{+0.00}_{-2.00}$ | $0.39^{+0.02}_{-0.03}$ | $14.40^{+0.43}_{-0.42}$ | 3 |
| SDSSJ095238.93+625818.9 | $25000^{+3000}_{-2800}$ | $5.91^{+0.30}_{-1.31}$ | $1.00^{+0.00}_{-2.00}$ | $0.02^{+0.02}_{-0.03}$ | $7.26^{+0.26}_{-0.25}$ | 3 |
| SDSSJ134632.65+281722.7 | $24500^{+4000}_{-1500}$ | $4.60^{+1.03}_{-0.00}$ | $0.88^{+0.12}_{-1.89}$ | $0.02^{+0.02}_{-0.02}$ | $6.78^{+0.24}_{-0.30}$ | 3 |
| SDSSJ002323.99-002953.2 | $27200^{+3600}_{-3100}$ | $5.15^{+1.06}_{-0.55}$ | $0.47^{+0.53}_{-1.48}$ | $0.03^{+0.02}_{-0.02}$ | $4.85^{+0.19}_{-0.16}$ | 3 |
| SDSSJ113241.58-063652.8 | $55000^{+100}_{-23100}$ | $4.60^{+1.61}_{-0.00}$ | $1.00^{+0.00}_{-2.00}$ | $0.04^{+0.03}_{-0.05}$ | $2.24^{+0.54}_{-0.22}$ | 3 |
| SDSSJ150513.52+110836.6 | $31900^{+4200}_{-5900}$ | $4.60^{+1.61}_{-0.00}$ | $-1.00^{+2.00}_{-0.00}$ | $0.02^{+0.03}_{-0.02}$ | $4.68^{+0.32}_{-0.36}$ | 3 |
| SDSSJ225638.34+065651.0 | $30700^{+5600}_{-3400}$ | $4.60^{+1.61}_{-0.00}$ | $0.75^{+0.25}_{-1.76}$ | $0.13^{+0.02}_{-0.02}$ | $5.43^{+0.35}_{-0.41}$ | 3 |
| SDSSJ172624.09+274419.3 | $33000^{+7500}_{-6600}$ | $4.60^{+1.61}_{-0.00}$ | $-1.00^{+2.00}_{-0.00}$ | $0.03^{+0.04}_{-0.03}$ | $3.47^{+0.30}_{-0.40}$ | 3 |
| SDSSJ113840.68-003531.7 | $27500^{+6100}_{-3600}$ | $5.29^{+0.91}_{-0.70}$ | $0.65^{+0.36}_{-1.65}$ | $0.01^{+0.03}_{-0.02}$ | $7.68^{+0.51}_{-0.66}$ | 3 |
| SDSSJ083006.17+475150.4 | $23200^{+5400}_{-1400}$ | $4.60^{+1.61}_{-0.00}$ | $0.87^{+0.13}_{-1.88}$ | $0.03^{+0.03}_{-0.03}$ | $4.25^{+0.14}_{-0.20}$ | 3 |
| SDSSJ152222.14-013018.3 | $21900^{+7500}_{-2500}$ | $4.60^{+1.61}_{-0.00}$ | $1.00^{+0.00}_{-2.00}$ | $0.16^{+0.05}_{-0.06}$ | $2.38^{+0.19}_{-0.22}$ | 3 |
| PG 1439-013 | $49000^{+6100}_{-8300}$ | $5.69^{+0.51}_{-1.10}$ | $-0.38^{+0.60}_{-0.63}$ | $0.05^{+0.02}_{-0.02}$ | $7.11^{+0.61}_{-0.49}$ | 3 |
| EC 20369-1804 | $55000^{+0}_{-10602}$ | $4.60^{+1.61}_{-0.00}$ | $-1.00^{+0.74}_{-0.00}$ | $0.08^{+0.02}_{-0.02}$ | $8.94^{+1.00}_{-0.11}$ | 3 |
| EC 12408-1427 | $23600^{+2400}_{-800}$ | $4.60^{+1.50}_{-0.00}$ | $1.00^{+0.00}_{-0.43}$ | $0.02^{+0.02}_{-0.01}$ | $18.23^{+0.42}_{-0.58}$ | 3 |
| EC 13332-1424 | $24300^{+3900}_{-4200}$ | $4.60^{+0.89}_{-0.00}$ | $-0.00^{+1.01}_{-1.00}$ | $0.04^{+0.03}_{-0.03}$ | $15.24^{+0.98}_{-1.10}$ | 3 |
| HS 1741+2133 | $28500^{+5000}_{-4700}$ | $4.60^{+1.61}_{-0.00}$ | $0.06^{+0.94}_{-1.07}$ | $0.09^{+0.03}_{-0.03}$ | $10.51^{+0.74}_{-0.86}$ | 3 |
| KIC 11558725 | $50000^{+5100}_{-27400}$ | $4.60^{+1.61}_{-0.00}$ | $1.00^{+0.00}_{-2.00}$ | $0.06^{+0.05}_{-0.06}$ | $4.42^{+2.86}_{-0.40}$ | 4 |
| CPD-20 1123 | $21800^{+2800}_{-4400}$ | $4.60^{+1.56}_{-0.00}$ | $-1.00^{+2.00}_{-0.00}$ | $0.01^{+0.04}_{-0.02}$ | $30.67^{+1.52}_{-1.91}$ | 4 |
| HE 1421-1206 | $24100^{+17000}_{-8200}$ | $6.20^{+0.00}_{-1.61}$ | $-1.00^{+2.00}_{-0.00}$ | $0.05^{+0.09}_{-0.06}$ | $6.12^{+1.13}_{-1.90}$ | 4 |
| V2579 Oph | $23300^{+5700}_{-6200}$ | $6.20^{+0.00}_{-1.61}$ | $-1.00^{+2.00}_{-0.00}$ | $0.04^{+0.06}_{-0.04}$ | $20.59^{+2.11}_{-2.46}$ | 4 |
| HE 0929-0424 | $27500^{+27500}_{-12600}$ | $5.54^{+0.66}_{-0.95}$ | $-1.00^{+2.00}_{-0.00}$ | $0.10^{+0.10}_{-0.10}$ | $4.15^{+1.21}_{-1.63}$ | 4 |
| KPD 1946+4340 | $27000^{+28100}_{-100}$ | $6.20^{+0.00}_{-1.61}$ | $1.00^{+0.00}_{-2.00}$ | $0.12^{+0.08}_{-0.04}$ | $9.82^{+1.54}_{-3.37}$ | 4 |
| GD 687 | $29200^{+25800}_{-7700}$ | $4.60^{+1.61}_{-0.00}$ | $1.00^{+0.00}_{-2.00}$ | $0.08^{+0.06}_{-0.07}$ | $8.93^{+1.97}_{-2.74}$ | 4 |
| PG 1232-136 | $26000^{+29100}_{-6900}$ | $4.60^{+1.61}_{-0.00}$ | $1.00^{+0.00}_{-2.00}$ | $0.07^{+0.09}_{-0.07}$ | $14.24^{+3.00}_{-5.09}$ | 4 |
| HE 0532-4503 | $40000^{+7600}_{-16200}$ | $6.20^{+0.00}_{-1.61}$ | $1.00^{+0.00}_{-2.00}$ | $0.08^{+0.03}_{-0.08}$ | $2.91^{+1.20}_{-0.42}$ | 4 |
| PG 1043+760 | $21800^{+3100}_{-2900}$ | $4.63^{+0.94}_{-0.03}$ | $-0.00^{+1.01}_{-1.00}$ | $0.00^{+0.03}_{-0.00}$ | $13.62^{+0.58}_{-0.67}$ | 4 |
| CD-30 11223 | $27000^{+28100}_{-6000}$ | $4.60^{+1.61}_{-0.00}$ | $0.71^{+0.30}_{-1.71}$ | $0.04^{+0.08}_{-0.05}$ | $21.47^{+3.45}_{-7.43}$ | 4 |
| SDSSJ165404.26+303701.8 | $54000^{+1100}_{-19300}$ | $4.80^{+1.40}_{-0.21}$ | $1.00^{+0.00}_{-1.19}$ | $0.10^{+0.02}_{-0.02}$ | $3.48^{+0.96}_{-0.07}$ | 4 |
| KIC 7668647 | $49000^{+6100}_{-26200}$ | $4.60^{+1.61}_{-0.00}$ | $1.00^{+0.00}_{-2.00}$ | $0.10^{+0.05}_{-0.08}$ | $4.04^{+2.63}_{-0.35}$ | 4 |
| EC 20260-4757 | $41000^{+14100}_{-13700}$ | $6.20^{+0.00}_{-1.61}$ | $1.00^{+0.00}_{-0.76}$ | $0.07^{+0.03}_{-0.05}$ | $8.20^{+2.40}_{-1.21}$ | 4 |
| NGC 188 2091 | – | – | – | – | – | 4 |
| EC 21556-5552 | $24400^{+6700}_{-4400}$ | $4.92^{+1.28}_{-0.33}$ | $-1.00^{+2.00}_{-0.00}$ | $0.00^{+0.06}_{-0.00}$ | $16.64^{+0.86}_{-2.58}$ | 4 |
| EC 02200-2338 | $25200^{+12500}_{-3300}$ | $6.20^{+0.00}_{-1.15}$ | $-0.68^{+1.69}_{-0.32}$ | $0.00^{+0.01}_{-0.00}$ | $27.14^{+0.64}_{-6.58}$ | 4 |
| EC 22202-1834 | $39000^{+16100}_{-15000}$ | $6.20^{+0.00}_{-1.61}$ | $0.72^{+0.29}_{-1.72}$ | $0.10^{+0.03}_{-0.07}$ | $8.81^{+2.92}_{-1.64}$ | 4 |
| EC 20182-6534 | $17600^{+9000}_{-1300}$ | $5.87^{+0.33}_{-1.28}$ | $0.88^{+0.12}_{-1.89}$ | $0.00^{+0.01}_{-0.00}$ | $18.77^{+0.55}_{-2.89}$ | 4 |
| EC 00404-4429 | $52000^{+3000}_{-25600}$ | $4.80^{+1.41}_{-0.20}$ | $1.00^{+0.00}_{-1.36}$ | $0.09^{+0.02}_{-0.06}$ | $7.69^{+3.59}_{-0.33}$ | 4 |
| PG 1558-007 | $23500^{+3200}_{-3500}$ | $5.90^{+0.30}_{-1.31}$ | $0.00^{+1.00}_{-1.01}$ | $0.14^{+0.04}_{-0.04}$ | $17.17^{+1.02}_{-1.05}$ | 5 |
| PG 1403+316 | $30900^{+5500}_{-3300}$ | $5.41^{+0.80}_{-0.81}$ | $1.00^{+0.00}_{-2.00}$ | $0.03^{+0.02}_{-0.03}$ | $10.62^{+0.67}_{-0.57}$ | 5 |
| HE 2150-0238 | 30700 | 4.60 | -1.00 | 0.11 | 0.00 | 5 |
| PG 0849+319 | $32100^{+3000}_{-4200}$ | $4.60^{+1.02}_{-0.00}$ | $-1.00^{+2.00}_{-0.00}$ | $0.05^{+0.02}_{-0.02}$ | $7.17^{+0.33}_{-0.40}$ | 5 |
| PG 2345+318 | $25400^{+3300}_{-1500}$ | $4.60^{+0.86}_{-0.00}$ | $-0.00^{+0.44}_{-1.00}$ | $0.06^{+0.02}_{-0.02}$ | $10.44^{+0.45}_{-0.50}$ | 5 |

| | | | | | | |
|---|---|---|---|---|---|---|
| PG 1432+159 | $22700^{+\ 2100}_{-\ 600}$ | $4.60^{+0.61}_{-0.00}$ | $1.00^{+0.00}_{-0.76}$ | $0.02^{+0.01}_{-0.01}$ | $11.62^{+0.21}_{-0.24}$ | 5 |
| HE 1415-0309 | $33200^{+16500}_{-\ 8500}$ | $4.60^{+1.61}_{-0.00}$ | $-1.00^{+2.00}_{-0.00}$ | $0.10^{+0.05}_{-0.06}$ | $3.03^{+0.46}_{-0.61}$ | 5 |
| SDSSJ032138.67+053840.0 | 30200 | 4.60 | -1.00 | 0.21 | 0.00 | 5 |
| SDSSJ150829.02+494050.9 | 27000 | 6.20 | 1.00 | 0.01 | 0.00 | 5 |
| SDSSJ102151.64+301011.9 | 28000 | 6.20 | 0.15 | 0.02 | 0.00 | 5 |
| SDSSJ082332.09+113641.9 | 30900 | 5.75 | -1.00 | 0.03 | 0.00 | 5 |

Table A.2.: Results for the single SED fits in the Geier sample (see section 5.3)

| Object | $T_{\rm eff}$ [K] | $\log g$ | z | E(B-V) | $d$ [kpc] | Qual. |
|---|---|---|---|---|---|---|
| HD 205805 | $25400^{+500}_{-500}$ | $5.13^{+0.25}_{-0.27}$ | $-0.35^{+0.29}_{-0.27}$ | $0.02^{+0.01}_{-0.01}$ | $0.22^{+0.09}_{-0.06}$ | 1 |
| Feige 65 | $24900^{+500}_{-300}$ | $5.86^{+0.21}_{-0.26}$ | $0.00^{+0.11}_{-0.36}$ | $0.00^{+0.01}_{-0.00}$ | $0.22^{+0.08}_{-0.05}$ | 1 |
| HD 4539 | $24200^{+900}_{-900}$ | $5.34^{+0.38}_{-0.47}$ | $-0.71^{+0.45}_{-0.29}$ | $0.02^{+0.02}_{-0.02}$ | $0.17^{+0.13}_{-0.07}$ | 2 |
| PG 1432+004 | $24100^{+1400}_{-1600}$ | $4.90^{+0.64}_{-0.30}$ | $-0.83^{+0.64}_{-0.17}$ | $0.06^{+0.02}_{-0.02}$ | $0.84^{+0.40}_{-0.45}$ | 2 |
| BD+482721 | $21500^{+700}_{-700}$ | $4.60^{+0.45}_{-0.00}$ | $-0.86^{+0.39}_{-0.15}$ | $0.03^{+0.02}_{-0.02}$ | $0.43^{+0.01}_{-0.17}$ | 2 |
| PG 0342+026 | $23800^{+700}_{-800}$ | $5.73^{+0.22}_{-0.24}$ | $0.28^{+0.12}_{-0.11}$ | $0.10^{+0.01}_{-0.01}$ | $0.13^{+0.05}_{-0.04}$ | 2 |
| GD108 | $25700^{+500}_{-500}$ | $4.77^{+0.47}_{-0.17}$ | $-0.56^{+0.36}_{-0.28}$ | $0.04^{+0.01}_{-0.01}$ | $1.56^{+0.35}_{-0.65}$ | 2 |
| SB 485 | $28000^{+700}_{-700}$ | $5.64^{+0.24}_{-0.29}$ | $-0.33^{+0.28}_{-0.27}$ | $0.03^{+0.01}_{-0.01}$ | $0.52^{+0.21}_{-0.13}$ | 2 |
| Feige 38 | $27300^{+1400}_{-1300}$ | $6.20^{+0.00}_{-0.15}$ | $0.27^{+0.21}_{-0.21}$ | $0.05^{+0.02}_{-0.02}$ | $0.25^{+0.05}_{-0.01}$ | 2 |
| [CW83] 1758+36 | $30900^{+900}_{-800}$ | $5.90^{+0.27}_{-0.31}$ | $-0.01^{+0.14}_{-0.32}$ | $0.02^{+0.01}_{-0.01}$ | $0.19^{+0.08}_{-0.05}$ | 2 |
| PHL 932 | $28500^{+1700}_{-1200}$ | $4.60^{+0.59}_{-0.00}$ | $-0.62^{+0.57}_{-0.39}$ | $0.01^{+0.02}_{-0.01}$ | $1.08^{+0.05}_{-0.53}$ | 2 |
| PG 0909+276 | $28500^{+1200}_{-1100}$ | $6.15^{+0.06}_{-0.47}$ | $0.52^{+0.19}_{-0.19}$ | $0.01^{+0.02}_{-0.02}$ | $0.20^{+0.15}_{-0.02}$ | 2 |
| [CW83] 0512-08 | $34400^{+2500}_{-1800}$ | $5.91^{+0.29}_{-1.07}$ | $0.24^{+0.27}_{-0.36}$ | $0.05^{+0.01}_{-0.01}$ | $0.19^{+0.48}_{-0.06}$ | 2 |
| HE 0151-3919 | $21500^{+900}_{-1500}$ | $4.60^{+0.22}_{-0.00}$ | $-1.00^{+1.18}_{-0.00}$ | $0.01^{+0.02}_{-0.01}$ | $2.32^{+0.06}_{-0.52}$ | 3 |
| EC 15103-1557 | $21300^{+4400}_{-1400}$ | $4.60^{+0.72}_{-0.00}$ | $1.00^{+0.00}_{-1.83}$ | $0.06^{+0.02}_{-0.02}$ | $1.21^{+0.08}_{-0.68}$ | 3 |
| EC 11349-2753 | $24100^{+4300}_{-5500}$ | $4.60^{+0.84}_{-0.00}$ | $-0.00^{+1.01}_{-1.00}$ | $0.05^{+0.03}_{-0.04}$ | $1.19^{+0.11}_{-0.76}$ | 3 |
| EC 14345-1729 | $23800^{+4800}_{-5200}$ | $4.60^{+1.20}_{-0.00}$ | $-0.00^{+1.01}_{-1.00}$ | $0.08^{+0.03}_{-0.04}$ | $1.36^{+0.14}_{-1.03}$ | 3 |
| HE 2307-0340 | $22700^{+2800}_{-900}$ | $6.20^{+0.00}_{-0.52}$ | $1.00^{+0.00}_{-2.00}$ | $0.07^{+0.02}_{-0.02}$ | $0.70^{+0.57}_{-0.02}$ | 3 |
| PG 1653+131 | $24000^{+1500}_{-800}$ | $4.60^{+0.13}_{-0.00}$ | $-0.00^{+0.25}_{-1.00}$ | $0.03^{+0.01}_{-0.01}$ | $2.67^{+0.04}_{-0.37}$ | 3 |
| HE 2237+0150 | $24500^{+3500}_{-1700}$ | $6.20^{+0.00}_{-1.61}$ | $1.00^{+0.00}_{-2.00}$ | $0.10^{+0.02}_{-0.03}$ | $0.82^{+4.41}_{-0.04}$ | 3 |
| PHL 44 | $23100^{+3600}_{-1500}$ | $6.12^{+0.08}_{-0.57}$ | $1.00^{+0.00}_{-2.00}$ | $0.03^{+0.02}_{-0.03}$ | $0.28^{+0.27}_{-0.04}$ | 3 |
| SB 815 | $25000^{+3300}_{-1400}$ | $4.60^{+0.59}_{-0.00}$ | $0.52^{+0.44}_{-1.52}$ | $0.00^{+0.01}_{-0.00}$ | $0.62^{+0.02}_{-0.30}$ | 3 |
| HE 2201-0001 | $31300^{+3500}_{-5200}$ | $4.60^{+1.61}_{-0.00}$ | $-1.00^{+2.00}_{-0.00}$ | $0.08^{+0.03}_{-0.02}$ | $8.37^{+0.54}_{-7.08}$ | 3 |
| PG 2205+023 | $22700^{+4600}_{-1900}$ | $5.63^{+0.58}_{-1.03}$ | $1.00^{+0.00}_{-2.00}$ | $0.04^{+0.02}_{-0.04}$ | $0.72^{+1.74}_{-0.37}$ | 3 |
| PG 2314+076 | $28500^{+2600}_{-1900}$ | $4.60^{+0.34}_{-0.01}$ | $-0.00^{+0.45}_{-1.00}$ | $0.10^{+0.02}_{-0.02}$ | $2.12^{+0.09}_{-0.68}$ | 3 |
| EC 12234-2607 | $26500^{+9700}_{-5900}$ | $4.60^{+1.61}_{-0.00}$ | $0.09^{+0.91}_{-1.10}$ | $0.08^{+0.05}_{-0.04}$ | $2.13^{+0.50}_{-1.74}$ | 3 |
| PG 2349+002 | $26300^{+800}_{-2500}$ | $5.86^{+0.26}_{-0.30}$ | $-1.00^{+1.78}_{-0.00}$ | $0.05^{+0.01}_{-0.01}$ | $0.38^{+0.19}_{-0.10}$ | 3 |
| PG 1549-001 | $29000^{+3200}_{-3700}$ | $4.60^{+0.97}_{-0.00}$ | $-0.00^{+1.01}_{-1.00}$ | $0.11^{+0.02}_{-0.02}$ | $4.18^{+0.20}_{-2.79}$ | 3 |
| HE 2349-3135 | $18900^{+8000}_{-1800}$ | $4.60^{+0.71}_{-0.00}$ | $1.00^{+0.00}_{-2.00}$ | $0.00^{+0.04}_{-0.00}$ | $4.92^{+0.87}_{-2.67}$ | 3 |
| HE 0007-2212 | $27000^{+5300}_{-3100}$ | $4.60^{+0.82}_{-0.00}$ | $-1.00^{+1.59}_{-0.00}$ | $0.00^{+0.03}_{-0.00}$ | $4.13^{+0.61}_{-2.52}$ | 3 |
| LB 275 | $21900^{+4200}_{-4400}$ | $4.60^{+1.61}_{-0.00}$ | $-1.00^{+2.00}_{-0.00}$ | $0.09^{+0.05}_{-0.05}$ | $2.93^{+0.32}_{-2.44}$ | 3 |
| PG 1303+097 | $25900^{+4500}_{-1700}$ | $4.60^{+0.80}_{-0.00}$ | $0.68^{+0.33}_{-1.68}$ | $0.02^{+0.02}_{-0.01}$ | $3.20^{+0.08}_{-1.91}$ | 3 |
| HE 2222-3738 | $25200^{+4000}_{-1200}$ | $6.20^{+0.00}_{-0.51}$ | $0.91^{+0.10}_{-1.91}$ | $0.00^{+0.02}_{-0.01}$ | $0.60^{+0.51}_{-0.02}$ | 3 |
| PG 1710+490 | $28800^{+1400}_{-3800}$ | $4.60^{+0.64}_{-0.00}$ | $-1.00^{+1.55}_{-0.00}$ | $0.03^{+0.02}_{-0.02}$ | $1.53^{+0.06}_{-0.81}$ | 3 |
| EC 14248-2647 | $27500^{+6000}_{-5300}$ | $4.60^{+1.04}_{-0.00}$ | $-0.12^{+1.13}_{-0.88}$ | $0.04^{+0.04}_{-0.03}$ | $1.00^{+0.14}_{-0.70}$ | 3 |
| HE 0207+0030 | $32100^{+3300}_{-2400}$ | $6.20^{+0.00}_{-1.61}$ | $1.00^{+0.00}_{-0.79}$ | $0.05^{+0.02}_{-0.02}$ | $0.91^{+5.21}_{-0.04}$ | 3 |
| KPD 2109+4401 | $27100^{+8700}_{-2300}$ | $4.60^{+1.61}_{-0.00}$ | $1.00^{+0.00}_{-2.00}$ | $0.06^{+0.03}_{-0.03}$ | $1.91^{+0.21}_{-1.62}$ | 3 |
| EC 21043-4017 | $39300^{+9700}_{-4800}$ | $4.60^{+1.03}_{-0.00}$ | $-0.27^{+0.67}_{-0.74}$ | $0.05^{+0.02}_{-0.02}$ | $2.23^{+0.24}_{-1.53}$ | 3 |
| HS 2033+0821 | $55000^{+0}_{-19383}$ | $4.76^{+1.44}_{-0.17}$ | $1.00^{+0.00}_{-2.00}$ | $0.14^{+0.02}_{-0.05}$ | $4.18^{+0.95}_{-3.52}$ | 3 |
| PHL 555 | $29000^{+1300}_{-3900}$ | $5.93^{+0.28}_{-0.84}$ | $-1.00^{+2.00}_{-0.01}$ | $0.00^{+0.02}_{-0.01}$ | $0.54^{+0.88}_{-0.16}$ | 3 |
| PG 1219+534 | $36800^{+4300}_{-4000}$ | $5.42^{+0.78}_{-0.83}$ | $-1.00^{+1.49}_{-0.00}$ | $0.00^{+0.02}_{-0.00}$ | $0.90^{+1.55}_{-0.55}$ | 3 |
| HE 1050-0630 | $33300^{+11300}_{-7000}$ | $5.79^{+0.42}_{-1.19}$ | $-1.00^{+2.00}_{-0.00}$ | $0.00^{+0.03}_{-0.00}$ | $0.87^{+3.12}_{-0.39}$ | 3 |
| EC 13047-3049 | $35000^{+20000}_{-8100}$ | $4.60^{+1.61}_{-0.00}$ | $-0.24^{+1.05}_{-0.76}$ | $0.05^{+0.04}_{-0.04}$ | $1.80^{+0.54}_{-1.46}$ | 3 |
| PHL 334 | $32000^{+2700}_{-5600}$ | $5.80^{+0.41}_{-0.66}$ | $-1.00^{+2.00}_{-0.00}$ | $0.01^{+0.02}_{-0.02}$ | $0.50^{+1.49}_{-0.20}$ | 3 |
| Feige 49 | $30300^{+6000}_{-1800}$ | $5.17^{+0.86}_{-0.58}$ | $1.00^{+0.00}_{-1.62}$ | $0.04^{+0.01}_{-0.02}$ | $0.94^{+0.59}_{-0.59}$ | 3 |
| HE 1021-0255 | $44000^{+11100}_{-6200}$ | $4.60^{+1.61}_{-0.00}$ | $-1.00^{+1.07}_{-0.00}$ | $0.08^{+0.03}_{-0.02}$ | $6.73^{+0.80}_{-5.73}$ | 3 |
| HE 0101-2707 | $55000^{+0}_{-14426}$ | $4.60^{+1.61}_{-0.00}$ | $1.00^{+0.00}_{-2.00}$ | $0.08^{+0.04}_{-0.03}$ | $7.23^{+0.24}_{-6.19}$ | 3 |
| PG 1207-032 | $38000^{+4600}_{-6300}$ | $6.20^{+0.00}_{-1.61}$ | $-0.94^{+1.95}_{-0.06}$ | $0.04^{+0.03}_{-0.02}$ | $0.38^{+2.12}_{-0.02}$ | 3 |
| PG 1505+074 | $26800^{+1300}_{-300}$ | $4.60^{+0.46}_{-0.00}$ | $1.00^{+0.00}_{-0.33}$ | $0.00^{+0.01}_{-0.00}$ | $1.34^{+0.03}_{-0.54}$ | 3 |

| | | | | | | |
|---|---|---|---|---|---|---|
| HE 1407+0033 | $45500^{+\ 9600}_{-13000}$ | $6.20^{+0.00}_{-0.39}$ | $-1.00^{+2.00}_{-0.00}$ | $0.04^{+0.03}_{-0.02}$ | $1.22^{+0.77}_{-0.18}$ | 3 |
| PG 1616+144 | $39300^{+\ 9100}_{-\ 5500}$ | $5.73^{+0.48}_{-1.13}$ | $-0.89^{+1.53}_{-0.12}$ | $0.06^{+0.03}_{-0.02}$ | $0.68^{+2.06}_{-0.32}$ | 3 |
| EC 00042-2737 | $55000^{+\ 0}_{-16334}$ | $4.80^{+1.41}_{-0.20}$ | $1.00^{+0.00}_{-1.81}$ | $0.09^{+0.02}_{-0.03}$ | $3.16^{+0.87}_{-2.62}$ | 3 |
| PHL 1548 | $35000^{+\ 2500}_{-\ 2300}$ | $5.84^{+0.34}_{-0.43}$ | $-1.00^{+1.15}_{-0.00}$ | $0.08^{+0.01}_{-0.01}$ | $0.49^{+0.34}_{-0.17}$ | 3 |
| EC 21494-7018 | $25700^{+\ 6800}_{-\ 4000}$ | $6.20^{+0.00}_{-1.61}$ | $-1.00^{+2.00}_{-0.00}$ | $0.00^{+0.03}_{-0.00}$ | $0.12^{+0.69}_{-0.01}$ | 4 |
| HE 0539-4246 | $22400^{+\ 3300}_{-\ 2900}$ | $5.38^{+0.60}_{-0.72}$ | $-1.00^{+2.00}_{-0.00}$ | $0.00^{+0.04}_{-0.00}$ | $1.23^{+1.57}_{-0.61}$ | 4 |
| EC 20106-5248 | $55000^{+\ 100}_{-28900}$ | $4.60^{+1.61}_{-0.00}$ | $0.45^{+0.55}_{-1.46}$ | $0.12^{+0.03}_{-0.05}$ | $1.95^{+0.06}_{-1.72}$ | 4 |
| HE 0321-0918 | $54000^{+\ 1000}_{-22900}$ | $5.38^{+0.83}_{-0.78}$ | $1.00^{+0.00}_{-0.89}$ | $0.18^{+0.02}_{-0.05}$ | $2.74^{+4.26}_{-1.98}$ | 4 |
| EC 03591-3232 | $25500^{+21300}_{-\ 3700}$ | $6.20^{+0.00}_{-1.52}$ | $-0.53^{+1.54}_{-0.47}$ | $0.00^{+0.02}_{-0.00}$ | $0.10^{+0.41}_{-0.01}$ | 4 |
| EC 01120-5259 | $24900^{+\ 2600}_{-\ 4200}$ | $4.60^{+1.15}_{-0.00}$ | $-1.00^{+2.00}_{-0.00}$ | $0.00^{+0.02}_{-0.00}$ | $1.75^{+0.12}_{-1.28}$ | 4 |
| EC 03263-6403 | $21600^{+\ 3600}_{-\ 2900}$ | $5.47^{+0.73}_{-0.88}$ | $-1.00^{+2.00}_{-0.00}$ | $0.00^{+0.04}_{-0.00}$ | $0.58^{+1.12}_{-0.33}$ | 4 |
| HE 2238-1455 | $52000^{+\ 3100}_{-29000}$ | $5.20^{+1.01}_{-0.60}$ | $1.00^{+0.00}_{-2.00}$ | $0.12^{+0.04}_{-0.08}$ | $4.95^{+5.57}_{-4.01}$ | 4 |
| HE 0447-3654 | $27300^{+\ 4600}_{-\ 5500}$ | $5.00^{+1.21}_{-0.40}$ | $-1.00^{+2.00}_{-0.00}$ | $0.00^{+0.03}_{-0.00}$ | $2.08^{+1.63}_{-1.57}$ | 4 |
| EC 02542-3019 | $27700^{+21300}_{-\ 4600}$ | $5.37^{+0.84}_{-0.77}$ | $-1.00^{+2.00}_{-0.00}$ | $0.00^{+0.06}_{-0.00}$ | $0.93^{+2.07}_{-0.58}$ | 4 |
| EC 05479-5818 | $25100^{+12600}_{-\ 4600}$ | $6.20^{+0.00}_{-1.61}$ | $-1.00^{+2.00}_{-0.00}$ | $0.01^{+0.07}_{-0.02}$ | $0.23^{+1.50}_{-0.02}$ | 4 |
| HE 2151-1001 | $54600^{+\ 500}_{-27700}$ | $6.20^{+0.00}_{-1.61}$ | $-1.00^{+2.00}_{-0.00}$ | $0.00^{+0.05}_{-0.00}$ | $1.79^{+10.50}_{-0.43}$ | 4 |
| EC 03408-1315 | $20400^{+\ 2800}_{-\ 2200}$ | $6.20^{+0.00}_{-1.15}$ | $-1.00^{+2.00}_{-0.00}$ | $0.00^{+0.03}_{-0.00}$ | $0.26^{+0.73}_{-0.01}$ | 4 |
| HE 0136-2758 | $23500^{+15800}_{-\ 6100}$ | $5.20^{+1.01}_{-0.60}$ | $-0.32^{+1.33}_{-0.68}$ | $0.00^{+0.07}_{-0.00}$ | $3.03^{+4.89}_{-2.13}$ | 5 |
| HS 2125+1105 | $36500^{+18500}_{-11800}$ | $4.60^{+1.61}_{-0.00}$ | $-1.00^{+2.00}_{-0.00}$ | $0.10^{+0.08}_{-0.07}$ | $9.68^{+3.26}_{-8.37}$ | 5 |
| HE 0123-3330 | $47000^{+\ 8100}_{-32000}$ | $5.02^{+1.19}_{-0.42}$ | $-1.00^{+2.00}_{-0.00}$ | $0.16^{+0.11}_{-0.16}$ | $4.21^{+4.66}_{-3.70}$ | 5 |
| HE 0513-2354 | $15000^{+40000}_{-\ 0}$ | $6.20^{+0.00}_{-1.61}$ | $-1.00^{+2.00}_{-0.00}$ | $0.00^{+0.27}_{-0.00}$ | $0.67^{+9.89}_{-0.08}$ | 6 |
| HE 0135-6150 | $15000^{+40000}_{-\ 0}$ | $4.60^{+1.61}_{-0.00}$ | $-1.00^{+2.00}_{-0.00}$ | $0.00^{+0.23}_{-0.00}$ | $4.88^{+7.17}_{-4.20}$ | 6 |
| EC 20229-3716 | $54100^{+\ 900}_{-33300}$ | $4.80^{+1.41}_{-0.20}$ | $1.00^{+0.00}_{-2.00}$ | $0.11^{+0.03}_{-0.11}$ | $0.93^{+0.34}_{-0.82}$ | 6 |
| HE 0019-5545 | $15000^{+\ 9366}_{-\ 0}$ | $4.60^{+1.61}_{-0.00}$ | $-1.00^{+2.00}_{-0.00}$ | $0.04^{+0.12}_{-0.04}$ | $3.78^{+1.16}_{-3.20}$ | 6 |
| HE 0415-2417 | 23000 | 4.74 | $-1.00$ | 0.00 | 0.00 | 6 |
| HS 1710+1614 | 55000 | 5.28 | $-1.00$ | 0.08 | 0.00 | 6 |

Table A.3.: Results for the sdB component of the stars in the Lisker sample (section 5.4)

| Object | $T_{\rm eff}$ [K] | $\log g$ | z | E(B-V) | $\theta \cdot 10^{-12}$ | Qual. |
|---|---|---|---|---|---|---|
| PHL 932 | $28500^{+1700}_{-1200}$ | $4.60^{+0.59}_{-0.00}$ | $-0.61^{+0.57}_{-0.39}$ | $0.01^{+0.02}_{-0.01}$ | $23.65^{+0.80}_{-1.01}$ | 2 |
| SB 485 | $26700^{+700}_{-800}$ | $6.04^{+0.17}_{-0.21}$ | $-0.19^{+0.24}_{-0.31}$ | $0.01^{+0.01}_{-0.01}$ | $15.39^{+0.27}_{-0.27}$ | 2 |
| GD 619 [i.e.] | $33300^{+2800}_{-2500}$ | $5.16^{+0.51}_{-0.57}$ | $-0.00^{+0.70}_{-1.00}$ | $0.00^{+0.01}_{-0.00}$ | $7.22^{+0.41}_{-0.35}$ | 2 |
| HE 0101-2707 | $49000^{+6100}_{-24300}$ | $4.60^{+1.61}_{-0.00}$ | $1.00^{+0.00}_{-2.00}$ | $0.10^{+0.05}_{-0.04}$ | $3.82^{+2.02}_{-0.34}$ | 3 |
| HE 0123-3330 | $55000^{+0}_{-39646}$ | $4.80^{+1.41}_{-0.20}$ | $1.00^{+0.00}_{-2.00}$ | $0.16^{+0.06}_{-0.17}$ | $3.30^{+4.01}_{-0.26}$ | 3 |
| HE 0151-3919 | $21700^{+900}_{-1400}$ | $4.60^{+0.17}_{-0.00}$ | $-1.00^{+1.13}_{-0.00}$ | $0.01^{+0.02}_{-0.01}$ | $11.04^{+0.26}_{-0.26}$ | 3 |
| HE 0207+0030 | $32200^{+6400}_{-3600}$ | $6.20^{+0.00}_{-1.61}$ | $1.00^{+0.00}_{-2.00}$ | $0.05^{+0.03}_{-0.03}$ | $4.44^{+0.36}_{-0.47}$ | 3 |
| HE 1021-0255 | $44300^{+10800}_{-7100}$ | $4.60^{+1.61}_{-0.00}$ | $-1.00^{+1.10}_{-0.00}$ | $0.08^{+0.03}_{-0.02}$ | $3.81^{+0.43}_{-0.42}$ | 3 |
| HE 1050-0630 | $31700^{+15700}_{-6000}$ | $5.13^{+1.08}_{-0.53}$ | $-0.86^{+1.87}_{-0.14}$ | $0.00^{+0.03}_{-0.00}$ | $7.85^{+0.97}_{-1.80}$ | 3 |
| HE 1407+0033 | $33100^{+9800}_{-3100}$ | $6.20^{+0.00}_{-0.47}$ | $1.00^{+0.00}_{-2.00}$ | $0.02^{+0.02}_{-0.02}$ | $3.79^{+0.25}_{-0.43}$ | 3 |
| HE 2201-0001 | $31300^{+3500}_{-5200}$ | $4.60^{+1.61}_{-0.00}$ | $-1.00^{+2.00}_{-0.00}$ | $0.08^{+0.03}_{-0.02}$ | $3.06^{+0.17}_{-0.21}$ | 3 |
| HE 2208+0126 | $24900^{+3600}_{-1400}$ | $6.20^{+0.00}_{-0.66}$ | $1.00^{+0.00}_{-2.00}$ | $0.05^{+0.02}_{-0.03}$ | $4.71^{+0.16}_{-0.15}$ | 3 |
| HE 2237+0150 | $24500^{+3300}_{-1600}$ | $6.20^{+0.00}_{-1.61}$ | $1.00^{+0.00}_{-2.00}$ | $0.10^{+0.02}_{-0.03}$ | $4.94^{+0.19}_{-0.18}$ | 3 |
| HE 2307-0340 | $22700^{+1300}_{-600}$ | $6.20^{+0.00}_{-0.43}$ | $1.00^{+0.00}_{-0.77}$ | $0.07^{+0.01}_{-0.01}$ | $5.83^{+0.08}_{-0.08}$ | 3 |
| HS 2033+0821 | $52000^{+3000}_{-16400}$ | $4.60^{+1.61}_{-0.00}$ | $1.00^{+0.00}_{-2.00}$ | $0.14^{+0.03}_{-0.04}$ | $5.23^{+1.42}_{-0.21}$ | 3 |
| HS 2357+2201 | $24300^{+6300}_{-2300}$ | $4.60^{+1.61}_{-0.00}$ | $0.68^{+0.33}_{-1.68}$ | $0.07^{+0.03}_{-0.03}$ | $10.01^{+0.47}_{-0.77}$ | 3 |
| GD 687 | $25200^{+2400}_{-800}$ | $4.60^{+0.25}_{-0.00}$ | $-0.00^{+0.21}_{-1.00}$ | $0.04^{+0.02}_{-0.02}$ | $10.50^{+0.24}_{-0.41}$ | 3 |
| PG 1207-032 | $38000^{+4600}_{-5000}$ | $6.20^{+0.00}_{-1.61}$ | $-0.94^{+1.95}_{-0.06}$ | $0.04^{+0.03}_{-0.02}$ | $10.67^{+0.64}_{-0.74}$ | 3 |
| PG 1549-001 | $29000^{+3300}_{-3600}$ | $4.60^{+0.97}_{-0.00}$ | $0.00^{+1.00}_{-1.01}$ | $0.11^{+0.02}_{-0.02}$ | $6.16^{+0.26}_{-0.30}$ | 3 |
| PHL 555 | $31500^{+1800}_{-5300}$ | $5.72^{+0.35}_{-0.46}$ | $-1.00^{+2.00}_{-0.00}$ | $0.01^{+0.02}_{-0.01}$ | $9.62^{+0.43}_{-0.42}$ | 3 |
| HE 0016+0044 [i.e.] | $27000^{+4000}_{-5200}$ | $4.60^{+1.61}_{-0.00}$ | $-1.00^{+2.00}_{-0.00}$ | $0.07^{+0.04}_{-0.04}$ | $7.48^{+0.50}_{-0.63}$ | 3 |
| HE 1038-2326 [i.e.] | $25700^{+6400}_{-6000}$ | $4.60^{+1.61}_{-0.00}$ | $-0.94^{+1.94}_{-0.07}$ | $0.00^{+0.13}_{-0.00}$ | $3.73^{+1.08}_{-1.08}$ | 3 |
| HE 1140-0500 [i.e.] | $34500^{+20600}_{-8900}$ | $4.60^{+1.61}_{-0.00}$ | $0.88^{+0.12}_{-1.89}$ | $0.12^{+0.10}_{-0.12}$ | $5.23^{+1.27}_{-2.56}$ | 3 |
| HE 1221-2618 [i.e.] | $28900^{+4000}_{-6200}$ | $4.60^{+1.61}_{-0.00}$ | $-1.00^{+2.00}_{-0.00}$ | $0.16^{+0.06}_{-0.07}$ | $7.56^{+0.74}_{-0.86}$ | 3 |
| HE 1254-1540 [i.e.] | $25800^{+7200}_{-6800}$ | $4.60^{+1.61}_{-0.00}$ | $-1.00^{+2.00}_{-0.00}$ | $0.00^{+0.08}_{-0.00}$ | $4.84^{+0.93}_{-1.00}$ | 3 |
| HE 1352-1827 [i.e.] | $38900^{+16200}_{-21500}$ | $4.60^{+1.61}_{-0.00}$ | $-1.00^{+2.00}_{-0.00}$ | $0.00^{+0.23}_{-0.00}$ | $2.28^{+2.40}_{-0.76}$ | 3 |
| HE 1422-1851 [i.e.] | $27300^{+4800}_{-5200}$ | $4.60^{+1.47}_{-0.00}$ | $-1.00^{+2.00}_{-0.00}$ | $0.00^{+0.14}_{-0.00}$ | $2.68^{+0.93}_{-0.53}$ | 3 |
| HE 1450-0957 [i.e.] | $34000^{+15200}_{-8400}$ | $4.60^{+1.61}_{-0.00}$ | $-0.79^{+1.80}_{-0.21}$ | $0.09^{+0.03}_{-0.02}$ | $5.07^{+0.70}_{-1.17}$ | 3 |
| HE 2322-0617 [i.e.] | $28100^{+6500}_{-6100}$ | $4.60^{+1.61}_{-0.00}$ | $-1.00^{+2.00}_{-0.00}$ | $0.00^{+0.13}_{-0.00}$ | $4.03^{+0.84}_{-0.90}$ | 3 |
| HS 1536+0944 [i.e.] | $55000^{+0}_{-13433}$ | $4.60^{+1.61}_{-0.00}$ | $1.00^{+0.01}_{-2.00}$ | $0.20^{+0.04}_{-0.07}$ | $3.04^{+27.57}_{-0.35}$ | 3 |
| HS 2216+1833 [i.e.] | $53200^{+1800}_{-38300}$ | $5.00^{+1.21}_{-0.40}$ | $1.00^{+0.00}_{-2.00}$ | $0.41^{+0.14}_{-0.33}$ | $10.84^{+12.09}_{-7.27}$ | 3 |
| KUV 01542-0710 [i.e.] | $32100^{+3400}_{-5800}$ | $4.60^{+1.61}_{-0.00}$ | $-1.00^{+2.00}_{-0.00}$ | $0.06^{+0.05}_{-0.06}$ | $3.59^{+0.20}_{-0.36}$ | 3 |
| PG 0258+184 [i.e.] | $30700^{+7500}_{-7600}$ | $4.60^{+1.61}_{-0.00}$ | $-1.00^{+2.00}_{-0.00}$ | $0.17^{+0.13}_{-0.18}$ | $5.33^{+0.77}_{-1.67}$ | 3 |
| HE 1459-0234 [i.e.] | $33600^{+4500}_{-6300}$ | $4.60^{+1.61}_{-0.00}$ | $-1.00^{+2.00}_{-0.00}$ | $0.07^{+0.17}_{-0.08}$ | $4.23^{+2.41}_{-1.17}$ | 3 |
| HS 1530+0542 [i.e.] | $32000^{+23100}_{-6800}$ | $6.20^{+0.00}_{-1.61}$ | $1.00^{+0.00}_{-2.00}$ | $0.16^{+0.07}_{-0.13}$ | $6.61^{+3.35}_{-3.49}$ | 3 |
| GD 617 [i.e.] | $41700^{+13300}_{-13300}$ | $6.20^{+0.00}_{-1.55}$ | $-1.00^{+2.00}_{-0.00}$ | $0.00^{+0.01}_{-0.01}$ | $2.72^{+2.85}_{-0.09}$ | 3 |
| HE 0007-2212 | $26500^{+28600}_{-5100}$ | $4.60^{+1.06}_{-0.00}$ | $-1.00^{+2.00}_{-0.00}$ | $0.00^{+0.07}_{-0.00}$ | $6.34^{+0.50}_{-2.36}$ | 4 |
| HE 0306-0309 | $17800^{+8300}_{-2800}$ | $4.60^{+1.59}_{-0.00}$ | $-1.00^{+2.00}_{-0.00}$ | $0.00^{+0.09}_{-0.00}$ | $4.59^{+0.47}_{-0.90}$ | 4 |
| HE 0321-0918 | $51900^{+3100}_{-21800}$ | $5.00^{+1.20}_{-0.41}$ | $1.00^{+0.00}_{-1.13}$ | $0.17^{+0.02}_{-0.06}$ | $3.89^{+1.38}_{-0.22}$ | 4 |
| HE 0539-4246 | $22400^{+3300}_{-2900}$ | $5.38^{+0.60}_{-0.72}$ | $-1.00^{+2.00}_{-0.00}$ | $0.00^{+0.04}_{-0.00}$ | $8.47^{+0.24}_{-0.60}$ | 4 |
| HE 0929-0424 | $27500^{+27500}_{-12600}$ | $5.54^{+0.66}_{-0.95}$ | $-1.00^{+2.00}_{-0.00}$ | $0.10^{+0.10}_{-0.10}$ | $4.15^{+1.21}_{-1.63}$ | 4 |
| HE 2151-1001 | $54300^{+700}_{-35200}$ | $4.80^{+1.41}_{-0.20}$ | $1.00^{+0.00}_{-2.00}$ | $0.10^{+0.08}_{-0.11}$ | $2.77^{+2.12}_{-0.45}$ | 4 |
| HE 2222-3738 | $26300^{+19600}_{-3900}$ | $6.16^{+0.05}_{-1.56}$ | $0.00^{+1.00}_{-1.00}$ | $0.00^{+0.08}_{-0.00}$ | $6.87^{+0.43}_{-2.16}$ | 4 |
| HE 2238-1455 | $52100^{+2900}_{-29100}$ | $5.20^{+1.01}_{-0.60}$ | $1.00^{+0.00}_{-2.00}$ | $0.12^{+0.04}_{-0.08}$ | $2.61^{+1.69}_{-0.13}$ | 4 |
| HE 2349-3135 | $18700^{+8600}_{-2000}$ | $4.60^{+0.84}_{-0.00}$ | $1.00^{+0.00}_{-2.00}$ | $0.00^{+0.04}_{-0.00}$ | $5.26^{+0.54}_{-0.87}$ | 4 |
| HS 2043+0615 | – | – | – | – | – | 4 |
| CBS 275 | $15000^{+3473}_{-0}$ | $4.60^{+1.07}_{-0.00}$ | $-1.00^{+1.76}_{-0.00}$ | $0.00^{+0.05}_{-0.00}$ | $10.40^{+0.17}_{-0.96}$ | 4 |
| HE 0230-4323 [i.e.] | $37800^{+15900}_{-15300}$ | $6.20^{+0.00}_{-1.61}$ | $1.00^{+0.00}_{-2.00}$ | $0.00^{+0.02}_{-0.00}$ | $7.48^{+5.16}_{-1.39}$ | 4 |

| | | | | | | |
|---|---|---|---|---|---|---|
| HE 1200-0931[i.e.] | 26400 | 4.76 | -0.34 | 0.31 | 0.00 | 4 |
| HE 1309-1102[i.e.] | 15000 | 6.01 | -0.78 | 0.06 | 0.00 | 4 |
| HE 1419-1205[i.e.] | 29100 | 6.20 | 1.00 | 0.10 | 0.00 | 4 |
| HE 1441-0558[i.e.] | $21600^{+33400}_{-\ 6700}$ | $4.60^{+1.61}_{-0.00}$ | $-1.00^{+2.00}_{-0.00}$ | $0.00^{+0.14}_{-0.00}$ | $9.26^{+2.23}_{-4.32}$ | 4 |
| HE 1519-0708[i.e.] | 51000 | 4.60 | 1.00 | 0.04 | 0.00 | 4 |
| HE 2156-3927[i.e.] | $30800^{+24200}_{-12100}$ | $6.20^{+0.00}_{-1.61}$ | $1.00^{+0.00}_{-2.00}$ | $0.00^{+0.10}_{-0.00}$ | $6.28^{+3.77}_{-1.68}$ | 4 |
| HE 2322-4559[i.e.] | $31000^{+24100}_{-14600}$ | $4.60^{+1.61}_{-0.00}$ | $1.00^{+0.00}_{-2.00}$ | $0.00^{+0.03}_{-0.00}$ | $4.13^{+2.64}_{-1.44}$ | 4 |
| PG 2122+157[i.e.] | $15000^{+40000}_{-\ 0}$ | $4.80^{+1.40}_{-0.21}$ | $-1.00^{+2.00}_{-0.00}$ | $0.09^{+0.22}_{-0.10}$ | $13.20^{+5.60}_{-10.51}$ | 4 |
| TON S155[i.e.] | $55000^{+\ 0}_{-40000}$ | $5.13^{+1.08}_{-0.53}$ | $1.00^{+0.00}_{-2.00}$ | $0.14^{+0.25}_{-0.14}$ | $1.74^{+8.42}_{-0.99}$ | 4 |
| GD 1237[i.e.] | $55000^{+\ 100}_{-40000}$ | $4.60^{+1.61}_{-0.00}$ | $1.00^{+0.00}_{-2.00}$ | $0.42^{+0.09}_{-0.43}$ | $4.48^{+5.93}_{-2.97}$ | 4 |
| HE 1033-2353 | $35600^{+19400}_{-15200}$ | $6.20^{+0.00}_{-1.61}$ | $1.00^{+0.00}_{-2.00}$ | $0.07^{+0.06}_{-0.08}$ | $2.86^{+1.41}_{-0.75}$ | 5 |
| HS 2125+1105 | $36500^{+18500}_{-11800}$ | $4.60^{+1.61}_{-0.00}$ | $-1.00^{+2.00}_{-0.00}$ | $0.10^{+0.08}_{-0.07}$ | $2.65^{+0.50}_{-0.67}$ | 5 |
| HE 0019-5545 | $15000^{+\ 9366}_{-\ 0}$ | $4.60^{+1.61}_{-0.00}$ | $-1.00^{+2.00}_{-0.00}$ | $0.04^{+0.12}_{-0.04}$ | $6.79^{+0.52}_{-1.60}$ | 6 |
| HE 0135-6150 | $15000^{+40000}_{-\ 0}$ | $4.60^{+1.61}_{-0.00}$ | $-1.00^{+2.00}_{-0.00}$ | $0.00^{+0.23}_{-0.00}$ | $5.25^{+0.86}_{-3.14}$ | 6 |
| HE 0136-2758 | – | – | – | – | – | 6 |
| HE 0415-2417 | 23000 | 4.64 | -1.00 | 0.00 | 0.00 | 6 |
| HE 0513-2354 | – | – | – | – | – | 6 |
| HS 1710+1614 | $55000^{+\ 0}_{-37350}$ | $4.60^{+1.61}_{-0.00}$ | $1.00^{+0.00}_{-2.00}$ | $0.08^{+0.06}_{-0.08}$ | $2.15^{+2.39}_{-0.11}$ | 6 |

[i.e.] infrared excess was detected

Table A.4.: Single SED results of the TGAS sample (see section 5.5)

| Object | $T_{\rm eff}$ | $\log g$ | z | E(B-V) | d [kpc] | Quality |
|---|---|---|---|---|---|---|
| HD 49798 | $45000^{+\ 5100}_{-\ 3600}$ | $5.18^{+0.83}_{-0.59}$ | $-0.53^{+0.82}_{-0.48}$ | $0.05^{+0.02}_{-0.02}$ | $0.13^{+0.14}_{-0.08}$ | 1 |
| BD+75 325 | $50000^{+\ 0}_{-\ 3563}$ | $5.91^{+0.29}_{-0.46}$ | $0.71^{+0.30}_{-0.41}$ | $0.02^{+0.01}_{-0.01}$ | $0.11^{+0.08}_{-0.04}$ | 1 |
| PG 1233+427 | $25400^{+\ 600}_{-\ 400}$ | $5.43^{+0.00}_{-0.11}$ | $0.34^{+0.23}_{-0.23}$ | $0.00^{+0.01}_{-0.00}$ | $0.37^{+0.06}_{-0.01}$ | 1 |
| PG 1234+253 | $34600^{+\ 3000}_{-\ 2300}$ | $6.20^{+0.00}_{-0.16}$ | $-1.00^{+0.63}_{-0.00}$ | $0.04^{+0.02}_{-0.02}$ | $0.10^{+0.03}_{-0.01}$ | 1 |
| Feige 67 | $46100^{+\ 3900}_{-\ 2500}$ | $5.66^{+0.55}_{-0.83}$ | $-0.06^{+0.45}_{-0.63}$ | $0.00^{+0.01}_{-0.00}$ | $0.42^{+0.71}_{-0.20}$ | 1 |
| HZ 44 | $35100^{+\ 4300}_{-\ 2100}$ | $6.20^{+0.00}_{-0.29}$ | $1.00^{+0.00}_{-0.14}$ | $0.01^{+0.02}_{-0.01}$ | $0.18^{+0.08}_{-0.01}$ | 1 |
| BD+42 3250 | $27300^{+\ 1200}_{-\ 1600}$ | $5.14^{+0.05}_{-0.16}$ | $-1.00^{+1.48}_{-0.00}$ | $0.03^{+0.02}_{-0.02}$ | $0.27^{+0.07}_{-0.02}$ | 1 |
| HD 205805 | $25000^{+\ 600}_{-\ 600}$ | $5.27^{+0.21}_{-0.22}$ | $0.18^{+0.20}_{-0.21}$ | $0.01^{+0.01}_{-0.01}$ | $0.19^{+0.06}_{-0.04}$ | 1 |
| FB 179 | $50000^{+\ 0}_{-\ 5607}$ | $4.60^{+1.46}_{-0.00}$ | $1.00^{+0.00}_{-0.79}$ | $0.05^{+0.02}_{-0.01}$ | $0.55^{+0.01}_{-0.46}$ | 1 |
| JL 194 | $24600^{+\ 500}_{-\ 300}$ | $5.27^{+0.14}_{-0.26}$ | $0.35^{+0.20}_{-0.18}$ | $0.00^{+0.01}_{-0.00}$ | $0.52^{+0.19}_{-0.08}$ | 2 |
| PG 0044+097 | $23300^{+\ 900}_{-\ 500}$ | $5.28^{+0.20}_{-0.00}$ | $-0.53^{+0.71}_{-0.48}$ | $0.00^{+0.02}_{-0.00}$ | $0.18^{+0.01}_{-0.04}$ | 2 |
| PG 0057+155 | $28600^{+\ 1800}_{-\ 1200}$ | $5.64^{+0.20}_{-0.00}$ | $0.13^{+0.37}_{-0.62}$ | $0.01^{+0.02}_{-0.01}$ | $0.33^{+0.02}_{-0.07}$ | 2 |
| PG 0101+039 | $25900^{+\ 400}_{-\ 400}$ | $5.59^{+0.05}_{-0.16}$ | $0.38^{+0.14}_{-0.14}$ | $0.01^{+0.01}_{-0.01}$ | $0.32^{+0.07}_{-0.02}$ | 2 |
| MCT 0106-3259 | $24500^{+\ 600}_{-\ 400}$ | $5.28^{+0.23}_{-0.18}$ | $0.18^{+0.24}_{-0.29}$ | $0.00^{+0.01}_{-0.00}$ | $0.48^{+0.12}_{-0.12}$ | 2 |
| FB 15 | $27100^{+\ 700}_{-\ 700}$ | $5.61^{+0.00}_{-0.08}$ | $0.13^{+0.20}_{-0.31}$ | $0.01^{+0.01}_{-0.01}$ | $0.53^{+0.05}_{-0.01}$ | 2 |
| FB 19 | $33800^{+\ 1400}_{-\ 800}$ | $6.00^{+0.00}_{-0.20}$ | $0.19^{+0.31}_{-0.45}$ | $0.00^{+0.01}_{-0.00}$ | $0.22^{+0.07}_{-0.01}$ | 2 |
| PG 0342+026 | $23800^{+\ 500}_{-\ 500}$ | $5.57^{+0.15}_{-0.10}$ | $0.84^{+0.16}_{-0.19}$ | $0.10^{+0.01}_{-0.01}$ | $0.16^{+0.03}_{-0.03}$ | 2 |
| LB 3459 | $38200^{+\ 4900}_{-\ 3100}$ | $5.56^{+0.00}_{-0.20}$ | $-0.61^{+0.68}_{-0.40}$ | $0.01^{+0.02}_{-0.02}$ | $0.30^{+0.11}_{-0.02}$ | 2 |
| CPD-64 481 | $26500^{+\ 700}_{-\ 400}$ | $5.50^{+0.16}_{-0.00}$ | $-0.36^{+0.38}_{-0.38}$ | $0.00^{+0.01}_{-0.01}$ | $0.25^{+0.01}_{-0.05}$ | 2 |
| UVO 0711+22 | $42900^{+\ 1800}_{-\ 4100}$ | $4.68^{+1.11}_{-0.08}$ | $1.00^{+0.00}_{-0.40}$ | $0.02^{+0.01}_{-0.01}$ | $1.14^{+0.14}_{-0.84}$ | 2 |
| CD-40 3927 | $44000^{+\ 2900}_{-\ 5900}$ | $5.40^{+0.81}_{-0.80}$ | $0.86^{+0.14}_{-0.94}$ | $0.01^{+0.01}_{-0.02}$ | $0.67^{+1.08}_{-0.42}$ | 2 |
| UVO 0825+15 | $45700^{+\ 4300}_{-\ 5200}$ | $6.02^{+0.00}_{-0.20}$ | $1.00^{+0.00}_{-0.39}$ | $0.04^{+0.01}_{-0.02}$ | $0.26^{+0.09}_{-0.02}$ | 2 |
| CD-34 5246 | $41900^{+\ 8200}_{-\ 5400}$ | $6.20^{+0.00}_{-1.25}$ | $-0.62^{+1.08}_{-0.38}$ | $0.05^{+0.02}_{-0.02}$ | $0.27^{+0.94}_{-0.03}$ | 2 |
| PG 0909+275 | $27800^{+\ 1400}_{-\ 500}$ | $5.99^{+0.20}_{-0.00}$ | $0.92^{+0.09}_{-0.30}$ | $0.00^{+0.02}_{-0.00}$ | $0.24^{+0.01}_{-0.05}$ | 2 |
| LSS 1274 | $50000^{+\ 0}_{-\ 7660}$ | $5.70^{+0.00}_{-0.31}$ | $0.81^{+0.19}_{-0.82}$ | $0.13^{+0.01}_{-0.02}$ | $0.58^{+0.26}_{-0.06}$ | 2 |
| FBS 0913+819 | $50000^{+\ 0}_{-\ 790}$ | $6.20^{+0.00}_{-0.48}$ | $0.26^{+0.27}_{-0.26}$ | $0.00^{+0.01}_{-0.00}$ | $0.25^{+0.18}_{-0.01}$ | 2 |
| BD+37 1977 | $47000^{+\ 3100}_{-\ 6600}$ | $6.20^{+0.00}_{-0.97}$ | $0.55^{+0.46}_{-0.68}$ | $0.04^{+0.02}_{-0.02}$ | $0.10^{+0.21}_{-0.01}$ | 2 |

| | | | | | | |
|---|---|---|---|---|---|---|
| PG 1032+406 | $30500^{+700}_{-500}$ | $5.85^{+0.03}_{-0.18}$ | $0.49^{+0.28}_{-0.30}$ | $0.00^{+0.01}_{-0.00}$ | $0.21^{+0.06}_{-0.01}$ | 2 |
| PG 1241-084 | $26800^{+1500}_{-1400}$ | $5.59^{+0.15}_{-0.06}$ | $0.35^{+0.53}_{-0.67}$ | $0.04^{+0.02}_{-0.02}$ | $0.15^{+0.02}_{-0.03}$ | 2 |
| LSE 44 | $40200^{+5700}_{-3800}$ | $5.00^{+0.59}_{-0.40}$ | $-0.88^{+0.54}_{-0.13}$ | $0.05^{+0.01}_{-0.01}$ | $1.01^{+0.71}_{-0.52}$ | 2 |
| PG 1352-022 | $48500^{+1500}_{-4700}$ | $6.20^{+0.00}_{-0.44}$ | $0.17^{+0.44}_{-0.60}$ | $0.04^{+0.01}_{-0.01}$ | $0.25^{+0.17}_{-0.02}$ | 2 |
| PG 1432+004 | $25900^{+2100}_{-2000}$ | $5.32^{+0.06}_{-0.15}$ | $0.64^{+0.36}_{-0.47}$ | $0.07^{+0.02}_{-0.03}$ | $0.55^{+0.13}_{-0.07}$ | 2 |
| PG 1433+239 | $26100^{+800}_{-800}$ | $5.42^{+0.12}_{-0.00}$ | $0.59^{+0.19}_{-0.19}$ | $0.01^{+0.01}_{-0.01}$ | $0.49^{+0.01}_{-0.07}$ | 2 |
| PG 1452+198 | $25100^{+1300}_{-500}$ | $5.92^{+0.29}_{-0.57}$ | $-0.95^{+1.00}_{-0.06}$ | $0.00^{+0.02}_{-0.00}$ | $0.25^{+0.24}_{-0.08}$ | 2 |
| PG 1505+074 | $39700^{+8500}_{-7400}$ | $5.52^{+0.00}_{-0.20}$ | $-0.93^{+0.79}_{-0.08}$ | $0.03^{+0.02}_{-0.03}$ | $0.56^{+0.21}_{-0.08}$ | 2 |
| PG 1519+640 | $27900^{+3000}_{-1500}$ | $5.60^{+0.18}_{-0.03}$ | $-0.36^{+0.72}_{-0.65}$ | $0.01^{+0.03}_{-0.01}$ | $0.39^{+0.05}_{-0.09}$ | 2 |
| PG 1722+286 | $29400^{+1500}_{-800}$ | $6.04^{+0.00}_{-0.20}$ | $1.00^{+0.00}_{-0.13}$ | $0.00^{+0.02}_{-0.00}$ | $0.39^{+0.12}_{-0.01}$ | 2 |
| UVO 1735+22 | $30800^{+4000}_{-1100}$ | $5.44^{+0.20}_{-0.00}$ | $-0.65^{+0.67}_{-0.35}$ | $0.00^{+0.03}_{-0.01}$ | $0.40^{+0.04}_{-0.10}$ | 2 |
| BD+39 3226 | $50000^{+0}_{-6513}$ | $6.00^{+0.00}_{-1.00}$ | $-1.00^{+1.24}_{-0.00}$ | $0.05^{+0.02}_{-0.02}$ | $0.13^{+0.23}_{-0.01}$ | 2 |
| PG 1758+364 | $30200^{+1100}_{-1000}$ | $5.91^{+0.00}_{-0.25}$ | $0.34^{+0.23}_{-0.24}$ | $0.01^{+0.01}_{-0.01}$ | $0.18^{+0.07}_{-0.01}$ | 2 |
| BD+48 2721 | $21000^{+700}_{-700}$ | $5.26^{+0.25}_{-0.00}$ | $0.15^{+0.29}_{-0.48}$ | $0.02^{+0.02}_{-0.02}$ | $0.20^{+0.01}_{-0.05}$ | 2 |
| CD-23 14565 | $27200^{+700}_{-700}$ | $5.40^{+0.00}_{-0.17}$ | $-0.97^{+0.41}_{-0.03}$ | $0.05^{+0.01}_{-0.01}$ | $0.14^{+0.04}_{-0.01}$ | 2 |
| LSII+18 9 | $50000^{+0}_{-8553}$ | $4.60^{+1.61}_{-0.00}$ | $0.56^{+0.45}_{-0.92}$ | $0.03^{+0.02}_{-0.02}$ | $1.67^{+0.04}_{-1.43}$ | 2 |
| HD 188112 | $21700^{+900}_{-900}$ | $5.63^{+0.14}_{-0.07}$ | $-1.00^{+0.55}_{-0.00}$ | $0.01^{+0.02}_{-0.02}$ | $0.11^{+0.02}_{-0.02}$ | 2 |
| EC 19563-7205 | $23700^{+900}_{-1200}$ | $4.97^{+0.33}_{-0.00}$ | $0.41^{+0.36}_{-0.31}$ | $0.09^{+0.02}_{-0.02}$ | $0.81^{+0.02}_{-0.27}$ | 2 |
| MCT 2341-3443 | $27100^{+400}_{-400}$ | $5.29^{+0.20}_{-0.00}$ | $0.27^{+0.19}_{-0.18}$ | $0.00^{+0.01}_{-0.00}$ | $0.28^{+0.01}_{-0.07}$ | 2 |
| EC 21313-7301 | $24800^{+1000}_{-900}$ | $5.32^{+0.00}_{-0.18}$ | $-0.48^{+0.56}_{-0.52}$ | $0.04^{+0.02}_{-0.02}$ | $0.45^{+0.11}_{-0.02}$ | 2 |
| Feige 110 | $40900^{+2900}_{-2400}$ | $5.80^{+0.25}_{-0.00}$ | $0.23^{+0.24}_{-0.22}$ | $0.01^{+0.01}_{-0.01}$ | $0.33^{+0.02}_{-0.09}$ | 2 |
| MCT 2350-3026 | $36300^{+2400}_{-1200}$ | $5.40^{+0.32}_{-0.38}$ | $1.00^{+0.00}_{-0.12}$ | $0.00^{+0.01}_{-0.01}$ | $0.56^{+0.33}_{-0.18}$ | 2 |
| PG 0011+283 | $23700^{+900}_{-1100}$ | $4.60^{+0.42}_{-0.00}$ | $-1.00^{+1.22}_{-0.00}$ | $0.00^{+0.02}_{-0.01}$ | $1.18^{+0.03}_{-0.45}$ | 3 |
| JL 241 | $38900^{+5700}_{-4000}$ | $6.20^{+0.00}_{-0.30}$ | $-0.49^{+0.95}_{-0.51}$ | $0.00^{+0.01}_{-0.00}$ | $0.22^{+0.11}_{-0.02}$ | 3 |
| GALEX J02096-1810 | $26100^{+1300}_{-600}$ | $5.80^{+0.41}_{-1.10}$ | $1.00^{+0.00}_{-0.92}$ | $0.00^{+0.01}_{-0.00}$ | $0.43^{+1.11}_{-0.17}$ | 3 |
| PHL 1434 | $20000^{+422}_{-0}$ | $5.00^{+0.32}_{-0.40}$ | $-1.00^{+0.88}_{-0.00}$ | $0.05^{+0.02}_{-0.01}$ | $0.57^{+0.34}_{-0.18}$ | 3 |
| TONS 403 | $34000^{+2400}_{-1700}$ | $6.20^{+0.00}_{-0.13}$ | $1.00^{+0.00}_{-0.39}$ | $0.01^{+0.01}_{-0.01}$ | $0.31^{+0.06}_{-0.01}$ | 3 |
| UVO 0512-08 | $37900^{+3300}_{-2500}$ | $5.89^{+0.00}_{-0.25}$ | $-1.00^{+0.59}_{-0.00}$ | $0.04^{+0.01}_{-0.01}$ | $0.20^{+0.08}_{-0.01}$ | 3 |
| PG 0823+499 | $20000^{+1123}_{-0}$ | $5.00^{+0.43}_{-0.40}$ | $0.44^{+0.57}_{-1.44}$ | $0.07^{+0.02}_{-0.02}$ | $0.45^{+0.27}_{-0.18}$ | 3 |
| PG 0919+272 | $34900^{+4100}_{-2300}$ | $6.00^{+0.13}_{-0.18}$ | $-0.60^{+0.77}_{-0.40}$ | $0.01^{+0.01}_{-0.01}$ | $0.34^{+0.11}_{-0.06}$ | 3 |
| US 719 | $31600^{+6300}_{-3900}$ | $6.20^{+0.00}_{-1.61}$ | $0.29^{+0.71}_{-1.30}$ | $0.08^{+0.04}_{-0.03}$ | $0.21^{+1.27}_{-0.02}$ | 3 |
| KUV 09565+3632 | $32500^{+2600}_{-2300}$ | $4.83^{+0.20}_{-0.00}$ | $1.00^{+0.00}_{-0.64}$ | $0.06^{+0.02}_{-0.02}$ | $1.31^{+0.07}_{-0.32}$ | 3 |
| EC 10106-2117 | $37700^{+9300}_{-8200}$ | $4.60^{+0.86}_{-0.00}$ | $-1.00^{+1.33}_{-0.00}$ | $0.07^{+0.02}_{-0.03}$ | $1.84^{+0.24}_{-1.15}$ | 3 |
| Feige 162 | $33600^{+4300}_{-3200}$ | $5.64^{+0.46}_{-0.55}$ | $1.00^{+0.00}_{-0.79}$ | $0.04^{+0.02}_{-0.02}$ | $0.56^{+0.51}_{-0.24}$ | 3 |
| EC 14248-2647 | $29000^{+10200}_{-5700}$ | $5.60^{+0.20}_{-0.00}$ | $0.00^{+1.00}_{-1.01}$ | $0.04^{+0.04}_{-0.04}$ | $0.32^{+0.03}_{-0.10}$ | 3 |
| EC 15103-1557 | $24400^{+4800}_{-3400}$ | $5.62^{+0.00}_{-0.33}$ | $1.00^{+0.00}_{-2.00}$ | $0.07^{+0.03}_{-0.01}$ | $0.39^{+0.23}_{-0.03}$ | 3 |
| PG 1610+529 | $27700^{+3500}_{-4500}$ | $5.01^{+0.78}_{-0.42}$ | $-0.74^{+1.75}_{-0.26}$ | $0.01^{+0.03}_{-0.02}$ | $0.90^{+0.64}_{-0.52}$ | 3 |
| KUV 16256+4034 | $50000^{+0}_{-22563}$ | $5.34^{+0.20}_{-0.00}$ | $-0.68^{+1.69}_{-0.32}$ | $0.07^{+0.02}_{-0.05}$ | $0.77^{+0.02}_{-0.34}$ | 3 |
| PB 7352 | $22700^{+1800}_{-500}$ | $5.25^{+0.07}_{-0.00}$ | $1.00^{+0.00}_{-1.65}$ | $0.02^{+0.01}_{-0.01}$ | $0.48^{+0.01}_{-0.04}$ | 3 |
| PG 1051+501 | $33800^{+7100}_{-4200}$ | $5.06^{+0.00}_{-0.20}$ | $1.00^{+0.00}_{-2.00}$ | $0.03^{+0.03}_{-0.03}$ | $1.39^{+0.56}_{-0.08}$ | 3 |
| PHL 178 | $49500^{+500}_{-12600}$ | $6.20^{+0.00}_{-0.66}$ | $-0.00^{+1.01}_{-1.00}$ | $0.05^{+0.02}_{-0.02}$ | $0.39^{+0.45}_{-0.06}$ | 3 |
| FBS 0102+362 | $31700^{+18400}_{-6000}$ | $4.62^{+1.59}_{-0.02}$ | $1.00^{+0.00}_{-2.00}$ | $0.04^{+0.04}_{-0.05}$ | $1.39^{+0.45}_{-1.20}$ | 4 |
| FBS 0224+330 | $50000^{+0}_{-23766}$ | $6.20^{+0.00}_{-1.61}$ | $-0.59^{+1.60}_{-0.41}$ | $0.07^{+0.02}_{-0.06}$ | $0.40^{+2.18}_{-0.13}$ | 4 |
| PB 9286 | $24600^{+23600}_{-2900}$ | $5.78^{+0.00}_{-0.23}$ | $1.00^{+0.00}_{-2.00}$ | $0.02^{+0.07}_{-0.03}$ | $0.39^{+0.34}_{-0.03}$ | 4 |
| GALEX J05487-5817 | $25000^{+22600}_{-3400}$ | $6.05^{+0.00}_{-0.25}$ | $0.44^{+0.57}_{-1.44}$ | $0.02^{+0.08}_{-0.02}$ | $0.28^{+0.24}_{-0.02}$ | 4 |
| GALEX J06062-2021 | $22900^{+3900}_{-3000}$ | $4.80^{+0.20}_{-0.00}$ | $-1.00^{+2.00}_{-0.00}$ | $0.02^{+0.04}_{-0.03}$ | $0.68^{+0.07}_{-0.18}$ | 4 |
| FBS 0654+366 | $25300^{+24800}_{-3500}$ | $5.26^{+0.95}_{-0.66}$ | $1.00^{+0.00}_{-2.00}$ | $0.08^{+0.07}_{-0.05}$ | $0.42^{+0.92}_{-0.29}$ | 4 |
| FBS 0658+350 | $20000^{+5748}_{-0}$ | $4.60^{+1.11}_{-0.00}$ | $1.00^{+0.00}_{-2.00}$ | $0.18^{+0.05}_{-0.03}$ | $0.78^{+0.10}_{-0.56}$ | 4 |
| GALEX J09348-2512 | $50000^{+0}_{-18193}$ | $4.88^{+0.59}_{-0.00}$ | $1.00^{+0.00}_{-1.28}$ | $0.08^{+0.02}_{-0.04}$ | $1.79^{+0.02}_{-1.09}$ | 4 |
| GALEX J11143-2421 | $33000^{+17100}_{-8600}$ | $5.19^{+0.20}_{-0.00}$ | $0.80^{+0.20}_{-1.81}$ | $0.15^{+0.04}_{-0.06}$ | $0.73^{+0.21}_{-0.25}$ | 4 |
| PG 1207-032 | $29900^{+20200}_{-3500}$ | $5.88^{+0.04}_{-0.17}$ | $-1.00^{+2.00}_{-0.00}$ | $0.00^{+0.01}_{-0.00}$ | $0.46^{+0.31}_{-0.05}$ | 4 |
| FBS 1400+389 | $20400^{+2100}_{-500}$ | $4.81^{+0.00}_{-0.20}$ | $1.00^{+0.00}_{-1.14}$ | $0.03^{+0.02}_{-0.02}$ | $0.67^{+0.20}_{-0.03}$ | 4 |
| GALEX J16322+8513 | $35000^{+15100}_{-14200}$ | $5.32^{+0.31}_{-0.00}$ | $-1.00^{+2.00}_{-0.00}$ | $0.09^{+0.03}_{-0.08}$ | $0.58^{+0.13}_{-0.21}$ | 4 |

| | | | | | | |
|---|---|---|---|---|---|---|
| PG 1710+490 | $30800^{+14100}_{-\ 5000}$ | $5.56^{+0.20}_{-0.00}$ | $-0.92^{+1.43}_{-0.09}$ | $0.03^{+0.04}_{-0.03}$ | $0.53^{+0.15}_{-0.13}$ | 4 |
| GALEX J17247+1132 | $24300^{+16200}_{-\ 4400}$ | $6.20^{+0.00}_{-1.18}$ | $-1.00^{+2.00}_{-0.00}$ | $0.04^{+0.09}_{-0.05}$ | $0.18^{+0.67}_{-0.01}$ | 4 |
| FBS 1850+443 | $27000^{+\ 9800}_{-\ 6100}$ | $6.20^{+0.00}_{-1.24}$ | $1.00^{+0.00}_{-2.00}$ | $0.10^{+0.05}_{-0.07}$ | $0.16^{+0.53}_{-0.01}$ | 4 |
| GALEX J20144-5239 | $50000^{+\ 0}_{-22645}$ | $5.13^{+0.25}_{-0.00}$ | $0.17^{+0.83}_{-1.18}$ | $0.11^{+0.02}_{-0.06}$ | $0.99^{+0.02}_{-0.46}$ | 4 |
| GALEX J20235+0136 | $27900^{+22100}_{-\ 3700}$ | $5.50^{+0.20}_{-0.00}$ | $1.00^{+0.00}_{-2.00}$ | $0.10^{+0.06}_{-0.04}$ | $0.52^{+0.21}_{-0.14}$ | 4 |
| GALEX J21035+3035 | $21400^{+11300}_{-\ 1200}$ | $6.20^{+0.00}_{-1.61}$ | $0.93^{+0.07}_{-1.94}$ | $0.00^{+0.07}_{-0.00}$ | $0.21^{+1.49}_{-0.01}$ | 4 |
| BPS CS22937-33 | $33800^{+16300}_{-\ 7900}$ | $5.51^{+0.25}_{-0.00}$ | $1.00^{+0.00}_{-2.00}$ | $0.05^{+0.04}_{-0.05}$ | $0.70^{+0.19}_{-0.26}$ | 4 |
| GALEX J22058-3141 | $37000^{+13000}_{-\ 9300}$ | $5.82^{+0.00}_{-0.28}$ | $-1.00^{+1.51}_{-0.00}$ | $0.16^{+0.03}_{-0.04}$ | $0.30^{+0.19}_{-0.06}$ | 4 |
| Bal 90900004 | $30300^{+\ 7700}_{-\ 3500}$ | $5.39^{+0.25}_{-0.00}$ | $-1.00^{+2.00}_{-0.00}$ | $0.00^{+0.03}_{-0.00}$ | $0.64^{+0.11}_{-0.18}$ | 4 |
| FBS 2253+335 | $26000^{+24100}_{-\ 3200}$ | $5.80^{+0.41}_{-1.20}$ | $1.00^{+0.00}_{-2.00}$ | $0.09^{+0.06}_{-0.03}$ | $0.32^{+1.55}_{-0.14}$ | 4 |
| Bal 90100001 | $28600^{+15600}_{-\ 2900}$ | $6.20^{+0.00}_{-1.61}$ | $1.00^{+0.00}_{-1.02}$ | $0.08^{+0.05}_{-0.03}$ | $0.16^{+1.03}_{-0.02}$ | 4 |
| FBS 2347+385 | $20000^{+\ 2388}_{-\ 0}$ | $5.28^{+0.20}_{-0.00}$ | $-1.00^{+1.34}_{-0.00}$ | $0.07^{+0.02}_{-0.02}$ | $0.28^{+0.02}_{-0.06}$ | 4 |
| FB 29 | $20000^{+\ 3134}_{-\ 0}$ | $6.20^{+0.00}_{-1.21}$ | $-1.00^{+1.89}_{-0.00}$ | $0.11^{+0.04}_{-0.02}$ | $0.15^{+0.44}_{-0.01}$ | 4 |
| FBS 0711+429 | $20000^{+\ 1391}_{-\ 0}$ | $4.60^{+0.88}_{-0.00}$ | $-1.00^{+1.07}_{-0.00}$ | $0.20^{+0.02}_{-0.01}$ | $0.63^{+0.03}_{-0.40}$ | 4 |
| BD+49 2226 | $20000^{+\ 1604}_{-\ 0}$ | $4.86^{+1.00}_{-0.00}$ | $-1.00^{+1.11}_{-0.00}$ | $0.19^{+0.03}_{-0.01}$ | $0.19^{+0.01}_{-0.14}$ | 4 |
| FBS 1654+352 | $20000^{+\ 2452}_{-\ 0}$ | $5.44^{+0.76}_{-0.85}$ | $-1.00^{+1.46}_{-0.00}$ | $0.00^{+0.03}_{-0.01}$ | $0.42^{+0.76}_{-0.25}$ | 4 |
| GALEX J21571+3308 | $36000^{+14100}_{-\ 6500}$ | $4.60^{+1.60}_{-0.01}$ | $0.98^{+0.03}_{-1.54}$ | $0.12^{+0.03}_{-0.04}$ | $2.20^{+0.50}_{-1.90}$ | 4 |
| FBS 2158+373 | $20000^{+\ 1561}_{-\ 0}$ | $4.60^{+0.59}_{-0.00}$ | $-1.00^{+1.15}_{-0.00}$ | $0.20^{+0.02}_{-0.01}$ | $0.66^{+0.03}_{-0.33}$ | 4 |
| FBS 2204+364 | $21000^{+\ 7400}_{-\ 1100}$ | $4.80^{+1.41}_{-0.20}$ | $1.00^{+0.00}_{-2.00}$ | $0.26^{+0.05}_{-0.04}$ | $0.43^{+0.20}_{-0.36}$ | 4 |
| FBS 2204+386 | $20000^{+\ 1995}_{-\ 0}$ | $4.83^{+1.37}_{-0.24}$ | $-1.00^{+1.24}_{-0.00}$ | $0.30^{+0.03}_{-0.02}$ | $0.45^{+0.17}_{-0.36}$ | 4 |
| FBS 2301+415 | $20000^{+\ 5119}_{-\ 0}$ | $4.60^{+1.05}_{-0.00}$ | $-0.21^{+1.22}_{-0.79}$ | $0.13^{+0.05}_{-0.01}$ | $0.69^{+0.09}_{-0.49}$ | 4 |
| Bal 90100002 | $20000^{+\ 4551}_{-\ 0}$ | $5.29^{+0.91}_{-0.09}$ | $-1.00^{+1.95}_{-0.00}$ | $0.13^{+0.05}_{-0.01}$ | $0.35^{+0.08}_{-0.23}$ | 4 |
| Bal 90100004 | $20000^{+\ 2481}_{-\ 0}$ | $4.86^{+0.99}_{-0.00}$ | $-0.55^{+1.33}_{-0.46}$ | $0.19^{+0.03}_{-0.01}$ | $0.49^{+0.04}_{-0.34}$ | 4 |
| GALEX J23204+2829 | $20000^{+\ 2720}_{-\ 0}$ | $4.60^{+1.47}_{-0.00}$ | $-1.00^{+1.49}_{-0.00}$ | $0.50^{+0.04}_{-0.02}$ | $0.35^{+0.03}_{-0.29}$ | 4 |

Table A.5.: Composite SED fits in the TGAS sample

| Object | $T_{\rm eff,sd}$ [K] | $\log g_{\rm sd}$ | z | $T_{\rm eff,MS}$ | $\log g_{\rm MS}$ | $\frac{A_c}{A_{sd}}$ | E(B-V) | $d$ [kpc] | Qual. |
|---|---|---|---|---|---|---|---|---|---|
| BD-11 162 | $49100^{+1000}_{-4300}$ | $5.82^{+0.39}_{-1.00}$ | $0.84^{+0.17}_{-0.64}$ | $6100^{+100}_{-200}$ | $5.20^{+0.00}_{-0.56}$ | $55^{+5}_{-8}$ | $0.02^{+0.02}_{-0.02}$ | $0.34^{+0.08}_{-0.14}$ | 1 |
| LSV+22 38 | $50000^{+0}_{-22871}$ | $4.60^{+0.77}_{-0.00}$ | $-1.00^{+2.00}_{-0.00}$ | $5900^{+1000}_{-3200}$ | $5.20^{+0.00}_{-3.20}$ | $14^{+27}_{-7}$ | $1.17^{+0.17}_{-0.18}$ | $0.18^{+1.13}_{-0.13}$ | 1 |
| PG 1253+284 | $32000^{+11100}_{-4400}$ | $6.20^{+0.00}_{-0.45}$ | $1.00^{+0.00}_{-2.00}$ | $6500^{+200}_{-200}$ | $3.04^{+1.14}_{-1.04}$ | $41^{+52}_{-21}$ | $0.09^{+0.07}_{-0.07}$ | $0.34^{+0.26}_{-0.09}$ | 1 |
| PG 1631-039 | $31400^{+1100}_{-900}$ | $5.74^{+0.12}_{-0.00}$ | $1.00^{+0.00}_{-0.34}$ | $2800^{+400}_{-500}$ | $4.00^{+1.21}_{-2.00}$ | $14^{+10}_{-4}$ | $0.00^{+0.01}_{-0.00}$ | $0.08^{+0.01}_{-0.02}$ | 1 |
| HD 185510 | $20000^{+830}_{-0}$ | $6.20^{+0.00}_{-1.61}$ | $-1.00^{+1.92}_{-0.00}$ | $5200^{+200}_{-200}$ | $5.20^{+0.00}_{-0.30}$ | $1000^{+0}_{-115}$ | $0.36^{+0.03}_{-0.03}$ | $0.06^{+0.35}_{-0.01}$ | 1 |
| CD-38 222 | $24900^{+500}_{-400}$ | $5.34^{+0.07}_{-0.14}$ | $-0.19^{+0.33}_{-0.58}$ | $4100^{+200}_{-300}$ | $5.20^{+0.00}_{-0.70}$ | $5 \pm 1$ | $0.00^{+0.01}_{-0.00}$ | $0.20^{+0.04}_{-0.02}$ | 2 |
| MCT 0146-2651 | $31300^{+1500}_{-1100}$ | $6.06^{+0.15}_{-0.42}$ | $0.49^{+0.40}_{-0.33}$ | $5700^{+200}_{-200}$ | $4.74^{+0.46}_{-2.45}$ | $32^{+7}_{-4}$ | $0.00^{+0.02}_{-0.00}$ | $0.31^{+0.20}_{-0.06}$ | 2 |
| PG 0232+095 | $28000^{+2000}_{-1900}$ | $6.20^{+0.01}_{-0.58}$ | $1.00^{+0.00}_{-0.20}$ | $5200^{+100}_{-100}$ | $4.50^{+0.44}_{-0.79}$ | $211^{+66}_{-47}$ | $0.07^{+0.04}_{-0.04}$ | $0.37^{+0.41}_{-0.05}$ | 2 |
| CPD-71 172 | $50000^{+0}_{-11745}$ | $6.20^{+0.00}_{-0.84}$ | $-1.00^{+1.01}_{-0.00}$ | $6800^{+100}_{-200}$ | $4.72^{+0.40}_{-0.42}$ | $165^{+8}_{-59}$ | $0.00^{+0.02}_{-0.00}$ | $0.27^{+0.44}_{-0.06}$ | 2 |
| HDE 283048 | $44800^{+5300}_{-10600}$ | $5.40^{+0.80}_{-0.81}$ | $1.00^{+0.00}_{-0.96}$ | $6500^{+200}_{-300}$ | $5.20^{+0.00}_{-0.50}$ | $244^{+173}_{-92}$ | $0.10^{+0.05}_{-0.06}$ | $0.52^{+0.15}_{-0.36}$ | 2 |
| LB 3390 | $27700^{+3600}_{-2700}$ | $4.60^{+0.25}_{-0.00}$ | $1.00^{+0.00}_{-0.16}$ | $3400^{+1500}_{-1100}$ | $5.20^{+0.00}_{-3.20}$ | $4^{+8}_{-1}$ | $0.13^{+0.04}_{-0.04}$ | $0.67^{+0.05}_{-0.17}$ | 2 |
| BD+34 1543 | $36300^{+5700}_{-4600}$ | $5.36^{+0.36}_{-0.00}$ | $1.00^{+0.00}_{-0.37}$ | $6300^{+200}_{-200}$ | $5.20^{+0.00}_{-0.85}$ | $119^{+40}_{-34}$ | $0.00^{+0.01}_{-0.00}$ | $0.42^{+0.04}_{-0.19}$ | 2 |
| BD+48 1777 | $50000^{+0}_{-7252}$ | $6.20^{+0.00}_{-1.61}$ | $1.00^{+0.00}_{-0.61}$ | $2400^{+1600}_{-100}$ | $3.50^{+1.70}_{-1.51}$ | $9^{+4}_{-7}$ | $0.02^{+0.01}_{-0.02}$ | $0.14^{+0.49}_{-0.02}$ | 2 |
| PG 0934+553 | $34800^{+15200}_{-5500}$ | $5.42^{+0.20}_{-0.00}$ | $-1.00^{+2.00}_{-0.00}$ | $5600^{+1100}_{-800}$ | $2.00^{+3.20}_{-0.00}$ | $14^{+16}_{-6}$ | $0.00^{+0.02}_{-0.00}$ | $0.57^{+0.27}_{-0.21}$ | 2 |
| Feige 34 | $50000^{+0}_{-1767}$ | $5.69^{+0.52}_{-0.71}$ | $0.32^{+0.64}_{-1.05}$ | $3600^{+300}_{-300}$ | $3.25^{+1.13}_{-1.08}$ | $20^{+5}_{-3}$ | $0.00^{+0.01}_{-0.00}$ | $0.32^{+0.40}_{-0.15}$ | 2 |
| PG 1101+249 | $27300^{+1300}_{-700}$ | $5.80^{+0.20}_{-0.00}$ | $0.38^{+0.37}_{-0.34}$ | $3600^{+700}_{-600}$ | $3.40^{+1.81}_{-1.40}$ | $5^{+3}_{-2}$ | $0.00^{+0.02}_{-0.00}$ | $0.37^{+0.02}_{-0.09}$ | 2 |
| PG 1104+243 | $48700^{+1300}_{-13700}$ | $5.94^{+0.00}_{-0.20}$ | $1.00^{+0.00}_{-1.70}$ | $6300^{+100}_{-200}$ | $2.00^{+0.51}_{-0.00}$ | $153^{+14}_{-71}$ | $0.00^{+0.02}_{-0.00}$ | $0.43^{+0.14}_{-0.12}$ | 2 |
| BD+10 2357 | $29600^{+9500}_{-3400}$ | $6.20^{+0.00}_{-0.55}$ | $-1.00^{+1.00}_{-0.00}$ | $7400^{+300}_{-300}$ | $4.20^{+0.26}_{-0.40}$ | $37^{+16}_{-13}$ | $0.00^{+0.02}_{-0.00}$ | $0.07^{+0.09}_{-0.02}$ | 2 |
| GD 319 | $31400^{+2300}_{-1900}$ | $6.20^{+0.00}_{-0.53}$ | $1.00^{+0.00}_{-0.34}$ | $5000^{+200}_{-200}$ | $5.20^{+0.00}_{-1.27}$ | $80^{+16}_{-12}$ | $0.00^{+0.02}_{-0.00}$ | $0.27^{+0.26}_{-0.03}$ | 2 |
| PG 1338+611 | $30000^{+5100}_{-3700}$ | $5.57^{+0.56}_{-0.81}$ | $0.32^{+0.69}_{-1.32}$ | $6100^{+300}_{-300}$ | $2.00^{+3.20}_{-0.00}$ | $21^{+11}_{-10}$ | $0.00^{+0.04}_{-0.00}$ | $0.38^{+0.68}_{-0.20}$ | 2 |
| PG 1629+081 | $37800^{+11200}_{-5900}$ | $5.48^{+0.00}_{-0.20}$ | $0.28^{+0.72}_{-1.29}$ | $3900^{+300}_{-600}$ | $5.20^{+0.00}_{-0.89}$ | $24^{+12}_{-7}$ | $0.10^{+0.03}_{-0.04}$ | $0.62^{+0.29}_{-0.05}$ | 2 |
| BD+29 3070 | $50000^{+0}_{-13049}$ | $5.72^{+0.00}_{-0.36}$ | $0.75^{+0.26}_{-1.75}$ | $6900^{+200}_{-200}$ | $4.64^{+0.47}_{-0.43}$ | $277^{+43}_{-139}$ | $0.01^{+0.05}_{-0.02}$ | $0.51^{+0.33}_{-0.15}$ | 2 |
| LSE 21 | $50000^{+0}_{-2522}$ | $5.93^{+0.27}_{-0.66}$ | $-1.00^{+0.26}_{-0.00}$ | $3500^{+700}_{-700}$ | $5.20^{+0.00}_{-1.95}$ | $12^{+8}_{-4}$ | $0.08^{+0.02}_{-0.02}$ | $0.27^{+0.21}_{-0.08}$ | 2 |
| LSII+22 21 | $50000^{+0}_{-1624}$ | $6.20^{+0.00}_{-0.65}$ | $-1.00^{+1.48}_{-0.00}$ | $2300^{+434}_{-0}$ | $5.20^{+0.00}_{-3.20}$ | $13^{+7}_{-9}$ | $0.00^{+0.01}_{-0.00}$ | $0.33^{+0.36}_{-0.01}$ | 2 |
| Bal 90600002 | $34200^{+6300}_{-3500}$ | $5.52^{+0.40}_{-0.61}$ | $0.21^{+0.50}_{-0.73}$ | $2400^{+100}_{-100}$ | $5.04^{+0.17}_{-0.67}$ | $13^{+6}_{-4}$ | $0.04^{+0.03}_{-0.03}$ | $0.50^{+0.66}_{-0.21}$ | 2 |
| BD-3 5357 | $22100^{+2300}_{-900}$ | $6.20^{+0.00}_{-0.67}$ | $-1.00^{+0.62}_{-0.00}$ | $4300^{+100}_{-100}$ | $4.55^{+0.47}_{-0.53}$ | $1000^{+0}_{-101}$ | $0.00^{+0.05}_{-0.00}$ | $0.11^{+0.13}_{-0.01}$ | 2 |
| BD-7 5977 | $45200^{+4600}_{-3200}$ | $6.20^{+0.01}_{-0.51}$ | $0.66^{+0.35}_{-0.47}$ | $4900^{+100}_{-100}$ | $4.00^{+0.51}_{-0.27}$ | $1000^{+0}_{-110}$ | $0.03^{+0.03}_{-0.02}$ | $0.27^{+0.22}_{-0.02}$ | 2 |
| PB 8783 | $26300^{+11300}_{-3000}$ | $6.20^{+0.00}_{-0.41}$ | $1.00^{+0.00}_{-2.00}$ | $7000^{+200}_{-400}$ | $5.20^{+0.00}_{-0.80}$ | $26^{+55}_{-19}$ | $0.05^{+0.12}_{-0.06}$ | $0.26^{+0.12}_{-0.11}$ | 3 |
| LB 1741 | $50000^{+0}_{-7642}$ | $5.80^{+0.40}_{-0.64}$ | $-0.00^{+1.01}_{-1.00}$ | $4300^{+200}_{-200}$ | $5.20^{+0.00}_{-0.72}$ | $15^{+3}_{-4}$ | $0.00^{+0.02}_{-0.00}$ | $0.53^{+0.56}_{-0.22}$ | 3 |
| GALEX J08111+2734 | $20000^{+14988}_{-0}$ | $5.30^{+0.90}_{-0.71}$ | $-1.00^{+2.00}_{-0.00}$ | $6800^{+400}_{-200}$ | $2.50^{+1.05}_{-0.50}$ | $14^{+253}_{-4}$ | $0.10^{+0.05}_{-0.11}$ | $0.56^{+4.52}_{-0.39}$ | 3 |
| GALEX J10179+5516 | $33200^{+16800}_{-13300}$ | $5.53^{+0.00}_{-0.93}$ | $1.00^{+0.00}_{-2.00}$ | $7100^{+400}_{-200}$ | $4.00^{+0.45}_{-0.49}$ | $135^{+148}_{-125}$ | $0.00^{+0.10}_{-0.00}$ | $0.91^{+2.93}_{-0.64}$ | 3 |
| PG 1051+501 | $37000^{+13100}_{-8700}$ | $5.06^{+0.01}_{-0.20}$ | $1.00^{+0.00}_{-2.00}$ | $2300^{+297}_{-0}$ | $2.00^{+1.21}_{-0.00}$ | $70^{+60}_{-34}$ | $0.00^{+0.06}_{-0.00}$ | $1.57^{+0.90}_{-0.32}$ | 3 |
| EC 11031-1348 | $31000^{+19100}_{-11000}$ | $6.20^{+0.00}_{-1.13}$ | $1.00^{+0.00}_{-2.00}$ | $7300^{+400}_{-500}$ | $4.70^{+0.50}_{-0.76}$ | $72^{+328}_{-68}$ | $0.15^{+0.19}_{-0.11}$ | $0.25^{+1.52}_{-0.18}$ | 3 |

Table A.5.: Composite SED fits in the TGAS sample

| Object | $T_{\rm eff,sd}$ [K] | $\log g_{\rm sd}$ | z | $T_{\rm eff,MS}$ | $\log g_{\rm MS}$ | $\frac{A_c}{A_{sd}}$ | E(B-V) | $d$ [kpc] | Qual. |
|---|---|---|---|---|---|---|---|---|---|
| FBS 1111+339 | $39200^{+10100}_{-7900}$ | $4.65^{+0.75}_{-0.05}$ | $-0.39^{+1.39}_{-0.62}$ | $4900^{+100}_{-100}$ | $4.50^{+0.50}_{-2.50}$ | $284^{+128}_{-81}$ | $0.00^{+0.04}_{-0.00}$ | $2.52^{+0.71}_{-1.26}$ | 3 |
| EC 11429-2701 | $20500^{+3900}_{-500}$ | $4.60^{+1.39}_{-0.00}$ | $1.00^{+0.00}_{-2.00}$ | $4600^{+700}_{-600}$ | $5.20^{+0.00}_{-3.20}$ | $3 \pm 1$ | $0.41^{+0.04}_{-0.06}$ | $0.35^{+0.03}_{-0.29}$ | 3 |
| EC 00179-6503 | $20000^{+21912}_{-0}$ | $6.20^{+0.00}_{-1.61}$ | $-1.00^{+2.00}_{-0.00}$ | $5500^{+1500}_{-600}$ | $5.20^{+0.00}_{-1.93}$ | $1000^{+0}_{-818}$ | $0.29^{+0.28}_{-0.15}$ | $0.21^{+0.85}_{-0.07}$ | 4 |
| GALEX J03493+2713 | $20000^{+11457}_{-0}$ | $5.32^{+0.41}_{-0.72}$ | $1.00^{+0.00}_{-2.00}$ | $4600^{+1200}_{-800}$ | $2.00^{+3.20}_{-0.00}$ | $2 \pm 1$ | $0.58^{+0.07}_{-0.04}$ | $0.13^{+0.10}_{-0.06}$ | 4 |
| GALEX J04557-2034 | $20000^{+30000}_{-0}$ | $6.20^{+0.01}_{-1.60}$ | $-1.00^{+2.00}_{-0.00}$ | $7300^{+1800}_{-1300}$ | $2.50^{+1.41}_{-0.50}$ | $8^{+992}_{-5}$ | $0.15^{+0.12}_{-0.15}$ | $0.15^{+5.99}_{-0.05}$ | 4 |
| GALEX J05073-2802 | $50000^{+0}_{-30000}$ | $5.51^{+0.20}_{-0.00}$ | $1.00^{+0.00}_{-2.00}$ | $5000^{+1200}_{-1000}$ | $5.20^{+0.00}_{-3.20}$ | $21^{+55}_{-11}$ | $0.37^{+0.10}_{-0.38}$ | $0.31^{+0.16}_{-0.16}$ | 4 |
| GALEX J07082+7802 | $30000^{+20100}_{-10000}$ | $6.20^{+0.00}_{-1.61}$ | $1.00^{+0.00}_{-2.00}$ | $6900^{+1000}_{-3000}$ | $4.05^{+1.16}_{-2.05}$ | $8^{+993}_{-6}$ | $0.36^{+0.14}_{-0.35}$ | $0.13^{+8.14}_{-0.06}$ | 4 |
| GALEX J10078-2924 | $43000^{+7100}_{-21800}$ | $4.86^{+1.34}_{-0.00}$ | $1.00^{+0.00}_{-2.00}$ | $5200^{+500}_{-800}$ | $5.20^{+0.00}_{-3.20}$ | $18^{+6}_{-12}$ | $0.00^{+0.08}_{-0.00}$ | $1.72^{+0.21}_{-1.28}$ | 4 |
| GALEX J11077-3731 | $37000^{+13100}_{-17000}$ | $5.40^{+0.81}_{-0.80}$ | $1.00^{+0.00}_{-2.00}$ | $7700^{+2600}_{-2300}$ | $5.20^{+0.00}_{-3.20}$ | $11^{+989}_{-10}$ | $0.31^{+0.14}_{-0.31}$ | $0.58^{+11.75}_{-0.47}$ | 4 |
| GALEX J13058-3657 | $38000^{+12100}_{-18000}$ | $4.60^{+1.61}_{-0.00}$ | $1.00^{+0.00}_{-2.00}$ | $7200^{+400}_{-1100}$ | $4.90^{+0.30}_{-2.53}$ | $42^{+624}_{-39}$ | $0.25^{+0.24}_{-0.22}$ | $1.63^{+0.77}_{-1.19}$ | 4 |
| HIP 67513 | $49200^{+900}_{-29200}$ | $5.50^{+0.01}_{-0.90}$ | $1.00^{+0.00}_{-2.00}$ | $9000^{+2300}_{-2200}$ | $4.50^{+0.71}_{-2.50}$ | $59^{+942}_{-58}$ | $0.00^{+0.11}_{-0.00}$ | $1.03^{+11.44}_{-0.79}$ | 4 |
| PG 1347+086 | – | – | – | – | – | – | – | – | 4 |
| GALEX J13564-4934 | $50000^{+0}_{-30000}$ | $5.58^{+0.32}_{-0.01}$ | $1.00^{+0.00}_{-2.00}$ | $5100^{+500}_{-600}$ | $2.00^{+3.20}_{-0.00}$ | $49^{+23}_{-25}$ | $0.07^{+0.12}_{-0.08}$ | $0.60^{+0.13}_{-0.37}$ | 4 |
| GALEX J17195+1512 | $38500^{+11600}_{-18500}$ | $4.60^{+1.61}_{-0.00}$ | $1.00^{+0.00}_{-1.48}$ | $6600^{+800}_{-700}$ | $5.00^{+0.21}_{-2.24}$ | $11^{+372}_{-5}$ | $0.40^{+0.06}_{-0.35}$ | $0.99^{+3.90}_{-0.31}$ | 4 |
| GALEX J17368+2806 | $49000^{+1100}_{-29000}$ | $4.60^{+1.49}_{-0.00}$ | $1.00^{+0.00}_{-2.00}$ | $4900^{+1000}_{-800}$ | $5.20^{+0.00}_{-3.20}$ | $10^{+3}_{-9}$ | $0.51^{+0.05}_{-0.08}$ | $0.65^{+0.08}_{-0.60}$ | 4 |
| Kepler 2M1938+4603 | $50000^{+100}_{-25800}$ | $5.51 \pm 0.02$ | $1.00^{+0.00}_{-2.00}$ | $2400^{+200}_{-100}$ | $5.03^{+0.17}_{-1.29}$ | $18^{+8}_{-17}$ | $0.04^{+0.04}_{-0.05}$ | $0.59^{+0.01}_{-0.22}$ | 4 |
| GALEX J20098+0310 | $43000^{+7100}_{-22000}$ | $5.36^{+0.20}_{-0.00}$ | $1.00^{+0.00}_{-2.00}$ | $4600^{+400}_{-400}$ | $4.61^{+0.60}_{-2.61}$ | $29^{+13}_{-19}$ | $0.03^{+0.08}_{-0.03}$ | $0.87^{+0.13}_{-0.47}$ | 4 |
| EC 20117-4014 | $50000^{+0}_{-30000}$ | $4.61^{+1.59}_{-0.02}$ | $1.00^{+0.00}_{-2.00}$ | $6300^{+1200}_{-1200}$ | $2.50^{+2.71}_{-0.50}$ | $16^{+55}_{-9}$ | $0.36^{+0.07}_{-0.22}$ | $1.31^{+1.27}_{-1.18}$ | 4 |
| GALEX J20209-2250 | $30900^{+19200}_{-10900}$ | $5.61^{+0.03}_{-0.36}$ | $1.00^{+0.00}_{-2.00}$ | $6100^{+400}_{-500}$ | $3.50^{+1.71}_{-1.50}$ | $48^{+148}_{-37}$ | $0.08^{+0.20}_{-0.09}$ | $0.42^{+0.82}_{-0.20}$ | 4 |
| GALEX J21306+2140 | $50000^{+0}_{-30000}$ | $5.00^{+1.21}_{-0.40}$ | $1.00^{+0.00}_{-2.00}$ | $6900^{+400}_{-500}$ | $3.39^{+1.81}_{-1.40}$ | $86^{+298}_{-80}$ | $0.12^{+0.06}_{-0.12}$ | $1.64^{+0.17}_{-1.48}$ | 4 |
| PG 2151+100 | $31100^{+7100}_{-5400}$ | $5.71^{+0.00}_{-0.25}$ | $1.00^{+0.00}_{-2.00}$ | $4100^{+300}_{-400}$ | $4.85^{+0.35}_{-1.24}$ | $14^{+4}_{-6}$ | $0.08^{+0.03}_{-0.04}$ | $0.42^{+0.18}_{-0.06}$ | 4 |

# Bibliography


Ahmad, A., & Jeffery, C. S. 2004, A&A, 413, 323

Asplund, M., Grevesse, N., Sauval, A. J., & Scott, P. 2009, ARA&A, 47, 481

Aznar Cuadrado, R., & Jeffery, C. S. 2001, A&A, 368, 994

Barlow, B. N., Kilkenny, D., Drechsel, H., et al. 2013, Monthly Notices of the Royal Astronomical Society, 430, 22

Basu, B. 2003, An Introduction to Astrophysics (Prentice-Hall Of India Pvt. Limited)

Bauer, F., & Husfeld, D. 1995, A&A, 300, 481

Bessell, M. S. 2000, PASP, 112, 961

—. 2005, ARA&A, 43, 293

Bessell, M. S., Castelli, F., & Plez, B. 1998, A&A, 333, 231

Bingham, R. G., & Cousins, A. W. J. 1974, Monthly Notes of the Astronomical Society of South Africa, 33, 15

Blanchette, J.-P., Chayer, P., Wesemael, F., et al. 2008, ApJ, 678, 1329

Bogges, A. 1978, in BAAS, Vol. 10, Bulletin of the American Astronomical Society, 442

Budding, E., & Demircan, O. 2007, Introduction to Astronomical Photometry, Cambridge Observing Handbooks for Research Astronomers (Cambridge University Press)

Camarota, L., & Holberg, J. B. 2014, MNRAS, 438, 3111

Carroll, B., & Ostlie, D. 2007, An Introduction to Modern Astrophysics (Pearson Addison-Wesley)

Chromey, F. 2010, To Measure the Sky: An Introduction to Observational Astronomy (Cambridge University Press)

Copperwheat, C. M., Morales-Rueda, L., Marsh, T. R., Maxted, P. F. L., & Heber, U. 2011, MNRAS, 415, 1381

Crawford, D. L. 1958, ApJ, 128, 185

Cutri, R. M., & et al. 2013, VizieR Online Data Catalog, 2328

Cutri, R. M., Skrutskie, M. F., van Dyk, S., et al. 2003, VizieR Online Data Catalog, 2246

Dorman, B., Rood, R. T., & O'Connell, R. W. 1993, ApJ, 419, 596

Draine, B. T. 2003, ARA&A, 41, 241

Draine, B. T. 2004, in The Cold Universe, Saas-Fee Advanced Course 32, Springer-Verlag, 308 pages, 129 figures, Lecture Notes 2002 of the Swiss Society for Astronomy and Astrophysics (SSAA), Springer, 2004. Edited by A.W. Blain, F. Combes, B.T. Draine, D. Pfenniger and Y. Revaz, ISBN 354040838x, p. 213, ed. A. W. Blain, F. Combes, B. T. Draine, D. Pfenniger, & Y. Revaz, 213

ESA, ed. 1997, ESA Special Publication, Vol. 1200, The HIPPARCOS and TYCHO catalogues. Astrometric and photometric star catalogues derived from the ESA HIPPARCOS Space Astrometry Mission

Fan, X., Burstein, D., Chen, J.-S., et al. 1996, AJ, 112, 628

Fitzpatrick, E. L. 1999, PASP, 111, 63

For, B.-Q., Green, E. M., Fontaine, G., et al. 2010, ApJ, 708, 253

Fukugita, M. 1998, Highlights of Astronomy, 11, 449

Fukugita, M., Ichikawa, T., Gunn, J. E., et al. 1996, AJ, 111, 1748

Fukugita, M., Yasuda, N., Doi, M., Gunn, J. E., & York, D. G. 2011, AJ, 141, 47

Geier, S. 2013, A&A, 549, A110

Geier, S., & Heber, U. 2012, A&A, 543, A149

Geier, S., Heber, U., Heuser, C., et al. 2013, A&A, 551, L4

Girven, J., Steeghs, D., Heber, U., et al. 2012, MNRAS, 425, 1013

Golay, M. 1966, in IAU Symposium, Vol. 24, Spectral Classification and Multicolour Photometry, ed. K. Loden, L. O. Loden, & U. Sinnerstad, 262

Gray, D. 2008, The observation and analysis of stellar photospheres (Cambridge University Press)

Heber, U. 2009, ARA&A, 47, 211

—. 2016, PASP, 128, 082001

Heber, U., Drechsel, H., Østensen, R., et al. 2004, A&A, 420, 251

Henden, A. A., Templeton, M., Terrell, D., et al. 2016, VizieR Online Data Catalog, 2336

Herwig, F. 2005, ARA&A, 43, 435

Hewett, P. C., Warren, S. J., Leggett, S. K., & Hodgkin, S. T. 2006, MNRAS, 367, 454

Høg, E., Fabricius, C., Makarov, V. V., et al. 2000, A&A, 355, L27

Hu, H., Tout, C. A., Glebbeek, E., & Dupret, M.-A. 2011, MNRAS, 418, 195

Husser, T.-O., Wende-von Berg, S., Dreizler, S., et al. 2013, A&A, 553, A6

Irrgang, A. 2014, PhD thesis

Jeffery, C. S., & Pollacco, D. L. 1998, MNRAS, 298, 179

Johnson, H. L., & Morgan, W. W. 1953, ApJ, 117, 313

Karttunen, H., Kröger, P., Oja, H., Poutanen, M., & Donner, K. 2007, Fundamental Astronomy (Springer Berlin Heidelberg)

Kupfer, T., Geier, S., Heber, U., et al. 2015, A&A, 576, A44

Kurucz, R. L. 1996, in Astronomical Society of the Pacific Conference Series, Vol. 108, M.A.S.S., Model Atmospheres and Spectrum Synthesis, ed. S. J. Adelman, F. Kupka, & W. W. Weiss, 160

Lawrence, A., Warren, S. J., Almaini, O., et al. 2007, MNRAS, 379, 1599

Lisker, T., Heber, U., Napiwotzki, R., et al. 2005, A&A, 430, 223

Luo, Y.-P., Németh, P., Liu, C., Deng, L.-C., & Han, Z.-W. 2016, The Astrophysical Journal, 818, 202

Martin, C., & GALEX Team. 2005, in IAU Symposium, Vol. 216, Maps of the Cosmos, ed. M. Colless, L. Staveley-Smith, & R. A. Stathakis, 221

Maxted, P. F. L., Heber, U., Marsh, T. R., & North, R. C. 2001, MNRAS, 326, 1391

Mermilliod, J.-C., Mermilliod, M., & Hauck, B. 1997, A&AS, 124, doi:10.1051/aas:1997197

Michalik, D., Lindegren, L., & Hobbs, D. 2015, A&A, 574, A115

Milone, E., & Sterken, C. 2011, Astronomical Photometry: Past, Present, and Future, Astrophysics and Space Science Library (Springer New York)

Napiwotzki, R., Karl, C. A., Lisker, T., et al. 2004, Ap&SS, 291, 321

Napiwotzki, R., Christlieb, N., Drechsel, H., et al. 2001, Astronomische Nachrichten, 322, 411

Naslim, N., Jeffery, C. S., Hibbert, A., & Behara, N. T. 2013, MNRAS, 434, 1920

Norris, J. M., Wright, J. T., Wade, R. A., Mahadevan, S., & Gettel, S. 2011, ApJ, 743, 88

Østensen, R. H. 2006, Baltic Astronomy, 15, 85

O'Toole, S. J., & Heber, U. 2006, A&A, 452, 579

Pauli, E.-M., Napiwotzki, R., Heber, U., Altmann, M., & Odenkirchen, M. 2006, A&A, 447, 173

Paunzen, E. 2015, A&A, 580, A23

Robinson, K. 2007, Spectroscopy: The Key to the Stars: Reading the Lines in Stellar Spectra, The Patrick Moore Practical Astronomy Series (Springer New York)

Saffer, R. A., Bergeron, P., Koester, D., & Liebert, J. 1994, ApJ, 432, 351

Schaffenroth, V., Geier, S., Drechsel, H., et al. 2013, A&A, 553, A18

Schlafly, E. F., & Finkbeiner, D. P. 2011, ApJ, 737, 103

Schlegel, D. J., Finkbeiner, D. P., & Davis, M. 1998, ApJ, 500, 525

Scholz, R.-D., Heber, U., Heuser, C., et al. 2015, A&A, 574, A96

Skrutskie, M. F., Cutri, R. M., Stiening, R., et al. 2006, AJ, 131, 1163

Sterken, C., & Manfroid, J. 1992, Astronomical Photometry: A Guide, Astrophysics and Space Science Library (Springer Netherlands)

Stroeer, A., Heber, U., Lisker, T., et al. 2007, A&A, 462, 269

Strömgren, B. 1956, Vistas in Astronomy, 2, 1336

Thejll, P., Ulla, A., & MacDonald, J. 1995, A&A, 303, 773

Ulla, A., & Thejll, P. 1998, A&AS, 132, 1

Vink, J. S., & Cassisi, S. 2002, A&A, 392, 553

Vos, J., Østensen, R. H., Németh, P., et al. 2013, A&A, 559, A54

Vos, J., Østensen, R. H., Degroote, P., et al. 2012, A&A, 548, A6

Wang, S., Gao, J., Jiang, B. W., Li, A., & Chen, Y. 2013, ApJ, 773, 30

Warner, B. 2016, A Practical Guide to Lightcurve Photometry and Analysis, The Patrick Moore Practical Astronomy Series (Springer International Publishing)

Wright, E. L., Eisenhardt, P. R. M., Mainzer, A. K., et al. 2010, AJ, 140, 1868

Zheng, Z., Shang, Z., Su, H., et al. 1999, AJ, 117, 2757

Erklärung

Hiermit erkläre ich, dass ich diese Masterarbeit selbständig angefertigt und keine anderen als die angegebenen Hilfsmittel verwendet habe.

Erlangen, den 28. September 2016

(Johannes Schaffenroth)